Dipl.-Ing Philipp Schachinger, BSc.

# Analysis of Low Frequency Neutral Point Currents and their Impact on Power Grids

**DOCTORAL THESIS**

to achieve the university degree of

Doktor der technischen Wissenschaften

submitted to

**Graz University of Technology**

**Supervisor**

Ao.Univ.-Prof. Dipl.-Ing. Dr.techn. Herwig Renner

Institute of Electrical Power Systems

**External Reviewer**

Univ.-Prof. Dipl.-Ing. Dr.techn. Thomas Kienberger

Chair of Energy Network Technology

Montantuniversität Leoben

Graz, April 2024

# Acknowledgement

Pursuing a PhD, conducting research and writing a thesis is a challenging task with ups and downs. There are situations where it seems impossible to finish at all. Only with the support of colleagues, friends and family, it was possible to finish this thesis and I want to express my thanks.

First, I want to thank my supervisor Prof. Herwig Renner for the opportunity to write this thesis. Thank you for giving me space to develop my own ideas but also keeping me on track when it was necessary. I also want the thank Prof. Thomas Kienberger for reviewing this thesis.

This work is part of a project between TU Graz, Siemens Energy Austria GmbH and Austrian Power Grid AG. I want to thank all project partners for their cooperation and all helpful discussions.

This thesis would not have been possible without the support of colleagues. Therefore, I want to thank all colleagues from IEAN, not only for the scientific and technical discussions, but also for the fun, laugh, encouragement, after work activities and your friendship.

Ein großer Dank geht an meine Familie, die mich immer unterstützt und mir diesen Weg ermöglicht hat. Vor allem geht ein Danke an meine Frau Veronika, die mir auch in den schwierigsten Zeiten mit Geduld und Mut zur Seite stand.

# Abstract

A safe and reliable supply of electrical energy is essential for our modern society. Therefore, the detection, prediction and analysis of possible risks for the power grid is a major task for grid operators and research groups. Low frequency currents lead to disturbances in the power grid and can endanger the safe and reliable operation of our energy system. These currents have frequencies far below the bulk frequencies of 50, 60 or 16.7 Hz and therefore show a DC behavior. This includes half-cycle saturation of transformers and all related effects on the grid. As this led to major disturbances in power grids in the past, the effect of low frequency currents must be analyzed and, if necessary, actions need to be taken.

This thesis analyses the impact of low frequency currents on power grids. For this purpose, an already existing transformer neutral point measurement system in the Austrian power grid was further improved and extended. With this measurement system, the highest-ever recorded geomagnetically induced currents in Austria were recorded. Additionally to improving and updating the existing hardware, alternative measurement systems were analyzed and tested.

The data of the in Europe unique measurement system, containing nine neutral point measurements, is used to identify the different sources of low frequency currents. Besides the already known major source, which is the interaction of the solar wind with the Earth's magnetic field leading to geomagnetically induced currents, further sources were identified and confirmed. This includes DC powered public transportation systems, switching operations in power systems and large power electronic devices such as digital power flow controllers.

The highest low frequency currents occur during solar storms, which can not only be measured but also calculated. Based on previous work, calculations of these geomagnetically induced currents were performed, influences of parameters were analyzed and results were compared with real measurements. Additionally, a software tool with a graphical user interface, enabling the usage without any further knowledge about the mathematical background or program structure, was created.

The effect of saturated transformers on the grid was investigated in terms of reactive power demand and harmonic current distortion. A modular approach of the developed tool and commercial power grid calculation software enables a cross-platform analysis of reactive power influence. The effect of a major solar storm and the arising problems due to the resulting additional reactive power demand are evaluated for two scenarios in the Austrian transmission grid. To enable a time-reasonable estimation of the influence of distorted transformer magnetizing currents, which does not rely on electromagnetic transient simulations, principal considerations about modelling approaches were made.

To reduce the impact of geomagnetically induced currents on the grid, a mitigation algorithm was developed. It is based on connecting additional available neutral points, to distribute the effects onto several transformers. Various constraints can be included in this optimization algorithm, e.g., a maximum neutral point current for each transformer or a maximum number of neutral point connection changes. This can reduce the risk of grid disturbances without any additional assets.

# Kurzfassung

Niederfrequente Ströme führen zu Störungen im Stromnetz und können den sicheren und zuverlässigen Betrieb unseres Energiesystems gefährden. Diese Ströme haben eine Frequenz weit unterhalb der Netzfrequenz von 50, 60 oder 16,7 Hz und zeigen daher ein Gleichstromverhalten und führt dadurch zur Halbzyklussättigung von Transformatoren und damit verbundenen Auswirkungen auf das Netz. Da dies in der Vergangenheit zu großen Störungen in Stromnetzen geführt hat, müssen die Auswirkungen niederfrequenter Ströme analysiert und gegebenenfalls Maßnahmen ergriffen werden.

In dieser Arbeit werden die Auswirkungen von niederfrequenten Strömen auf Stromnetze untersucht. Zu diesem Zweck wurde ein bereits bestehendes Sternpunktmesssystem verbessert und erweitert. Zusätzlich zur Verbesserung und Modernisierung der bestehenden Hardware wurde ein neuer Messsystemtyp entwickelt und installiert, der den Netzbetrieb nicht beeinflusst. Mit dem Messsystem wurden die höchsten jemals in Österreich gemessenen geomagnetisch induzierten Ströme aufgezeichnet.

Die Daten des in Europa einzigartigen Messsystems, das aus neun Sternpunktmessungen besteht, werden zur Identifizierung der verschiedenen Quellen von niederfrequenten Strömen verwendet. Neben der bereits bekannten Hauptquelle, der Wirkung des Sonnenwindes auf das Erdmagnetfeld was zu geomagnetisch induzierten Strömen führt, wurden weitere Quellen nachgewiesen und identifiziert. Dazu gehören öffentliche Verkehrssysteme, Schaltvorgänge in Stromnetzen und große leistungselektronische Geräte.

Die Berechnung der geomagnetisch induzierten Ströme wurde als Softwaretool mit einer grafischen Benutzeroberfläche erstellt, sodass die Anwendung ohne weitere Kenntnisse über den mathematischen Hintergrund oder Programmstruktur möglich ist. Neben der Berechnung der Ströme in allen Transformatoren und Leitungen kann mit dieser Software auch der zusätzliche Blindleistungsbedarf von Transformatoren abgeschätzt werden.

Die Auswirkung von gesättigten Transformatoren auf das Netz wurde in Bezug auf den Blindleistungsbedarf und die harmonische Verzerrung analysiert. Ein modularer Ansatz des entwickelten Tools in Kombination mit kommerzieller Netzberechnungssoftware ermöglicht eine plattformübergreifende Analyse des Blindleistungseinflusses. Die Auswirkung eines großen Sonnensturms und die daraus resultierenden Probleme aufgrund des zusätzlichen Blindleistungsbedarfs werden für zwei Szenarien im österreichischen Übertragungsnetz analysiert. Um eine zeitlich sinnvolle Abschätzung des Einflusses verzerrter Transformator-Magnetisierungsströme zu ermöglichen, wurden grundsätzliche Überlegungen zu Modellierungsansätzen angestellt.

Um den Einfluss von niederfrequenten Strömen auf das Netz zu reduzieren, wurde ein Reduktionsalgorithmus entwickelt. Er basiert auf Erden zusätzlich verfügbarer Sternpunkte, um die Auswirkungen auf mehrere Transformatoren zu verteilen. Maximale Transformatorströme oder Beschränkungen aufgrund von des Netzbetriebs können als Randbedingungen hinzugefügt werden. Dadurch kann das Risiko von Netzstörungen ohne zusätzliche Anlagen verringert werden.

# CONTENTS

# List of Abbreviations

| | |
|---|---|
| **AC** | alternating flux |
| **acf** | Auto correlation function |
| **APG** | Austrian Power Grid |
| **API** | Application programming interface |
| **BDV** | Budkov Observatory, Czech Republic |
| **CME** | coronal mass ejection |
| **DAQ** | data acquisition |
| **DC** | direct current |
| **DCC** | direct current compensation |
| **DGA** | Dissolved gas analysis |
| **DMM** | differential magnetometer method |
| **DsT** | disturbance storm time |
| **EST** | Eastern standard time |
| **FFT** | Fast Fourier transformation |
| **FORESEEN** | Fiber optical current measurement Project |
| **FUR** | Fürstenfeldbruck Observatory, Germany |
| **GeoSphere Austria** | Meteorological and geological service Austria |
| **GIC** | geomagnetically induced current |
| **GMD** | geomagnetic disturbance |
| **GND** | Ground |
| **GPS** | Global Positioning System |
| **GSM** | Global System for Mobile Communications |
| **HV** | high voltage |
| **HVAC** | High voltage alternating current |
| **HVDC** | High voltage direct current |
| **IAGA** | International Association of Geomagnetism and Aeronomy |
| **ISES** | International Solar Energy Society |
| **ISS** | international space station |
| **Kp** | Global geomagnetic activity index |
| **lat** | latitude |
| **LFC** | low frequency current |
| **long** | longitude |
| **LP** | Lethinen-Pirjola |
| **LV** | low voltage |
| **M39** | Earth layer model M39 |
| **MP 1-4** | measurement point 1-4 |
| **NASA** | National Space Agency |
| **NCK** | Nagycenk Observatory, Hungary |
| **NOAA** | US National Oceanic and Atmospheric Admission |
| **NP01-09** | Neutral point measurement system 01-09 |
| **obj.Func** | Objective Function |
| **P** | Performance Parameter |
| **p.u.** | per unit |
| **PMU** | phasor measurement unit |

| | |
|---|---|
| **R** | Pearson’s correlation coefficient |
| **RMS** | root mean squared |
| **RMSE** | root mean squared error |
| **SCADA** | Supervisory Control and Data Acquisition |
| **SR 1-5** | shunt reactor 1-5 |
| **SSC** | sudden storm commencement |
| **Sub** | substation |
| **SVC** | Static var compensator |
| **Tennet** | German Transmission grid operator |
| **UTC** | Coordinated Universal Time |
| **WIC** | Conrad Observatory, Austria |

# List of Symbols

| | |
|---|---|
| $a_j$, $b_j$ | fitting parameters |
| $A_{xV}$ | allocation matrix for HV and LV |
| $\alpha_n$ | reflection coefficient of layer n |
| $A_\nu$, $B_\nu$ | Fourier coefficients |
| $B$ | magnetic field |
| $BMC_{xV}$ | Boolean minimum connection matrix |
| $BNM$ | branch-node matrix |
| $BNM_{lin}$ | line branch-node matrix |
| $BNM_{sub}$ | substation branch-node matrix |
| $BNM_{tra}$ | transformer branch-node matrix |
| $B_x$ | magnetic field in northern direction |
| $B_y$ | magnetic field in eastern direction |
| $B_z$ | magnetic field in earth direction |
| $c$ | voltage factor |
| $C_T$ | reduced transformer system network matrix |
| $D$ | electric field strength |
| $d_n$ | earth layer thickness |
| $E$ | electric field |
| $E_{inv}$ | inverse calculated electric field |
| $E_{inv,x}$ | inverse calculated electric field in x direction |
| $E_{inv,y}$ | inverse calculated electric field in y direction |
| $e_x$, $e_y$, $e_z$ | unit vector in x-, y-, and z- direction |
| $E_x$, $E_y$, $E_z$ | electric field in x-, y-, z-direction |
| $f$ | frequency |
| $\varphi_{ij}$ | Latitudinal angle between points i and j |
| $H$ | magnetic field strength |
| $H1 - H8$ | Harmonics with order 1-8 |
| $I$ | current |
| $I^e$ | earthing currents, LP-Method |
| $I_{DC,ABC}$ | calculated direct current in phase A,B,C |
| $I_{GIC}$ | effective DC transformer current |
| $I_{HV}$ | Current HV winding |
| $I_{k1}''$ | line-to-earth fault current |
| $I_{lin}$ | Currents in lines |
| $I_{LV}$ | Current LV winding |
| $I_{NP,DCC}$ | calculated neutral point current from DCC measurements |
| $i_m$ | Magnetization current |
| $I_{sub}$ | currents in substation grounding systems |
| $I_T$ | Transformer current |
| $I_{T,max}$ | maximum allowed transformer neutral point current |
| $I_{T,meas}$ | measured transformer currents |
| $I_{Th}$ | threshold current |
| $I_{Tn}$ | transformer current at transformer n |
| $I_{Tra}$ | currents in transformers |

| | |
|---|---|
| $J$ | electric current density |
| $J^e$ | line currents, LP-Method |
| $K$ | Q-slope factor |
| $L$ | inductance |
| $L_x$ | distance in north-direction |
| $L_y$ | distance in east-direction |
| $MC_{xV}$ | minimum connection matrix for HV and LV |
| $\mu$ | magnetic permeability |
| $\mu_0$ | magnetic permeability in free space |
| $\mu_R$ | relative magnetic permeability |
| $n$ | winding ratio / number of turns |
| $N_B$ | number of branches |
| $n_C$ | Number of turns, common winding |
| $n_{DCC}$ | Number of DCC turns |
| $n_{HV}$ | Number of turns, HV winding |
| $N_{lin}$ | number of lines |
| $n_{LV}$ | Number of turns, LV winding |
| $N_N$ | number of nodes |
| $N_{net}$ | number of grid nodes without grounding nodes |
| $N_S$ | number of substations |
| $n_S$ | Number of turns series winding |
| $N_{sub}$ | number of substations |
| $N_T$ | number of transformer neutral points |
| $np$ | neutral point vector / optimization variable |
| $np_{0i}$ | original neutral point connection i |
| $NP_A$ | neutral point substation A |
| $NP_B$ | neutral point substation B |
| $npc_{max}$ | maximum allowed neutral point changes |
| $np_i$ | neutral point i |
| $\nu$ | verdet constant |
| $\omega$ | angular frequency |
| $p$ | complex skin depth |
| $\Phi$ | magnetic flux |
| $\Phi_{AC}$ | alternating flux |
| $\Phi_{DC}$ | Direct flux |
| $\Phi_{sat}$ | Saturation flux |
| $\phi$ | phase angle |
| $Q$ | reactive power |
| $Q_{loss}$ | reactive power loss due to GIC |
| $Qslope_{low}$, $Qslope_{high}$ | slope for reactive power calculations |
| $R$ | resistance |
| $R_b$ | branch resistance |
| $R_c$ | common winding resistance auto transformer |
| $R_g$ | grounding resistance |
| $R_{g,T}$ | resistance of tower grounding |
| $R_l$ | line resistance |
| $R_s$ | series winding resistance auto transformer |

| | |
|---|---|
| $R_{sw}$ | resistance of shield wire |
| $R_{w,HV}$ | HV winding resistance transformer |
| $R_{w,LV}$ | LV winding resistance transformer |
| $r_{xx}$ | autocorrelation value of a signal x(t) |
| $\rho_E$ | specific earth resistivity |
| $\rho$ | charge density or earth resistivity |
| $SC_{xV}$ | substation connection matrix for voltage level HV and LV |
| $\sigma$ | conductivity |
| $\sigma_m$ | conductivity in bottom layer |
| $\sigma_n$ | conductivity in layer n |
| $T$ | cycle time |
| $t$ | time |
| $\tau$ | time constant |
| $\theta$ | polarization angle of light |
| $\theta$ | Phase angle |
| $\vartheta$ | rotation angle |
| $TN_{HV,LV}$ | Neutral point of Transformer N, HV or LV side |
| $Un$ | nominal voltage |
| $v$ | Harmonic order |
| $v(t)$ | voltage time series |
| $\hat{V}$ | voltage peak value |
| $V_{HV}$ | High voltage |
| $V_{LV}$ | Low voltage |
| $V_N$ | nodal voltage |
| $V_{pu}$ | Transformer voltage in p.u. |
| $V_{s,i}$ | driving voltage between substation i and reference node |
| $V_{Tn}$ | driving voltage source in tower footing |
| $V_s$ | driving voltage source |
| $w_p(t)$ | Window function |
| $x(t)$ | signal |
| $X_h$ | Main inductance |
| $X_{sat}$ | Air-core inductance |
| $X_\sigma$ | Leakage inductance |
| $Y^n$ | admittance matrix, LP-Method |
| $Y_C$ | coupling matrix |
| $Y_G$ | grounding matrix |
| $Y_N$ | network admittance matrix |
| $Z$ | complex earth impedance |
| $Z^e$ | earthing impedance matrix, LP-Method |
| $Z_{(0)}$ | zero sequence impedance |
| $Z_{(1)}$ | positive sequence impedance |
| $Z_{(2)}$ | negative sequence impedance |
| $Z_{inv,xy}$ | surface impedance in xy-direction |
| $Z_{inv,yx}$ | surface impedance in yx-direction |
| $Z_m$ | earth impedance at bottom layer |
| $Z_n$ | earth impedance in layer n |
| $Z_{n0}$ | intrinsic impedance of layer n |

# 1 Introduction

## 1.1 Scope of Research

In 2014, unusual audible transformer noise was recognized in a newly installed transformer in the Austrian Power Grid. First measurements in the transformer neutral point with a power spectrum analyzer and a current clamp revealed DC currents [1]. This was the start of a cooperation between the Austrian Power Grid operator APG, the Austrian meteorological service GeoSphere Austria and the Institute of Electrical Power System (IEAN) from Graz University of Technology. The project revealed that the DC currents in the transformer neutral points origin from the interaction between solar winds and the earth's magnetic field, leading to geomagnetically induced currents (GICs) [2, 3]. Continuous measurement systems were installed in several substations in Austria and calculations of GICs were done by GeoSphere Austria and IEAN and validated with the new measured data [4].

A follow-up project started in 2019 with an additional partner. Siemens Energy Austria, a transformer manufacturer, joined and contributed detailed knowledge about power transformers. The objective of this second project was to gain further knowledge on low frequency neutral point currents, improve the calculations, model the behavior of transformers under DC bias and develop countermeasure techniques suited for the Austrian power grid. As part of this project, this thesis focuses on the influence of low frequency currents on power grids.

The goal of this thesis is to gain further knowledge regarding the effects of low frequency currents (LFCs) on power grids. The term "LFC" includes all currents with frequencies between 0.01 mHz and 1 Hz and are therefore far lower than the operation frequency of the power grid. Among identified sources, geomagnetically induced currents are the source, with the highest impact on power grids. In order to evaluate the risk of LFCs on the power grid, the measurement data needs to be categorized by sources and impacts.

In the first step, the existing GIC calculations from [5] were extended with a graphical user interface. This enables easier usage of the calculation tool and a wider range of users. These calculations use magnetic field measurements, earth models and power grid data to calculate GICs in lines, transformers and substation grounding systems.

The already in Austria existing neutral point measurement system was improved. This includes the update of hardware, software, automated data analysis and the extensions from five measurement systems to nine systems in operation.

The next step was to evaluate the performance of the GIC calculation with a sensitivity analysis. This shows the impact of unknown or uncertain parameters e.g. the influence of substation grounding resistances. Afterward, GIC simulations are compared to measurements to see the influence of different parameters on the simulation accuracy.

The influence of LFCs on power grids is analyzed in terms of additional reactive power demand and harmonic emissions.

To mitigate the effects of GICs on power grids, a new mitigation method, based on changing the location(substation) and number of neutral point connections, is presented and evaluated.

## 1.2 Research Questions

The following research questions are addressed in this thesis:

- How can the accuracy of GIC calculations in the Austrian power grid be improved?

    - Analysis of the influence of unknown grid parameters
    - Installation of new measurement devices
- What other sources lead to low frequency currents?
- What are the consequences of LFCs?
    - Calculation of reactive power demand
    - Worst-case analysis of reactive power demand
    - How can transformer current harmonics for system studies be calculated
- What countermeasures are suitable for the Austrian Power Grid to reduce the influence of LFCs?

## 1.3 Outline of this Thesis

This doctoral thesis is structured as follows:

*Section 2 Theory and State of the Art of LFC Analysis*

This section gives a brief introduction to the fundamentals of space weather at the beginning, followed by an analysis of the effects of historic geomagnetic disturbances and their impact on human infrastructure. Different methods to calculate GICs are discussed. An overview of state-of-the-art mitigation methods is presented. The section is concluded with the description of selected LFC measurement techniques and their operations sites around the world.

*Section 3 Measurement of LFCs in the Austrian Power Grid*

The focus of intention in this segment is to describe the neutral point measurement systems installed in the Austrian power grid. The different locations, patterns and general measurement results are presented. Measurements of days with high and low geomagnetic activity are discussed. Additionally, an optical current measurement system, which is still under development, is given.

*Section 4 Identified Sources of Low Frequency Currents*

This portion of the thesis lists the identified low frequency sources and describes the methods used to detect them. The methods are based on the measurements described in section 3 and show recurring patterns, day-time and location dependency in the measurement data. With these methods, switching in power systems and public transportation as LFC sources were identified. Additional temporary measurements during tests of digital power flow controllers led to conclusions about large power electronic devices.

*Section 5 Calculation of GIC in the Austrian Transmission System*

This chapter deals with the calculation of GICs. The principal calculation with the nodal-admittance method is shown and results are compared with measurements. The impact of uncertain and unknown parameters is presented via sensitivity analysis and discussed. This includes grid sizes, shield wires and changes in the grid topology. Methods to reduce the influence of uncertainty are discussed and the influence on simulation accuracy is highlighted.

*Section 6 Effects of LFCs on Power Grids*

The effects of saturated transformers and their backlash on power grids are discussed in this section. The additional reactive power demand and harmonic emission are calculated and worst-case scenarios are presented. This is

done with a modified, simple and modular approach. An example of the influence of additional reactive power demand on the Austrian power grid is described. The principal relation between harmonic currents, direct flux and distorted voltage is calculated and discussed.

*Section 7 Method for Minimizing the Impact of GICs*

A novel mitigation technique, based on not connected neutral points is presented throughout this part. For this purpose, an optimization algorithm distributes the GICs on several transformers to reduce the overall GIC load in the grid. The effectiveness of this algorithm is shown on a test grid.

*Section 8 Conclusion*

This section concludes the results of this thesis and suggests research areas for further investigation.

# 2 Theory and State of the Art

At the beginning of this chapter, a brief introduction to space weather, related classifications and historical events caused by solar storms is given. Furthermore, the effects of low frequency currents on power systems are discussed and the calculation of geomagnetically induced currents is shown. As there are ways to reduce the impact of LFCs on power grids, the known methods are presented before the different LFC measurement techniques are concluded at the end.

## 2.1 Space weather

The closest star in our galaxy, the sun, produces energy through the fusion of hydrogen to helium. The energy is then transported by radiation from the core through the radiation zone to the convection zone, which takes approximately 170000 years. From the convection zone, energy is transported via material convection to the solar atmosphere, which consists of several different layers. One of these layers is the photosphere, which is the layer where most of the light is emitted [6]. In this layer, so-called sunspots occur, which are cooler regions but the magnetic fields in this area are much higher [6]. The photosphere is followed by the chromosphere and the outmost layer, the corona. The corona emits a continuous stream of charged particles into space, the solar wind, which constantly interacts with the Earth's magnetic field. Under calm solar wind conditions, this interaction leads only to small changes in the magnetic field of 20-40 nT over a day in Austria [7] or Sweden [8]. During a geomagnetic storm, large amounts of charged particles are ejected from the corona as a coronal mass ejection (CME), leading to large changes in the Earth's magnetic field [9], e.g. up to 35 nT/min in Austria in 2017 [7], more than 500 nT/min during the 2003 solar storm in Sweden and even 2500 nT/min during an event in 1982 [10]. As soon as the CME arrives at Earth, the magnetic field is rapidly compressed and the field strength rises. This is called the sudden storm commencement SSC [11] and marks the first phase of a geomagnetic storm. In the following hours, a continuous decline of the magnetic field happens, which is the main phase of the storm and the largest geomagnetic variations occur [9]. The impact of the solar storm mainly depends on the field direction of the interplanetary magnetic field [12]. During the recovery phase, which marks the end of the storm, the field strength returns to the normal value.

The sun follows an 11-year cycle, in which the magnetic poles switch orientation [9]. During the solar maximum, the number of sunspots increases and more CMEs are likely to emerge from the sun [7]. At the time of writing (autumn 2023), the sun is approaching the maximum of solar cycle 25. When a CME is earth-directed, the impact leads to the above-described geomagnetic disturbance (GMD). There are different ways to classify a GMD and its related influence on the magnetic field. The most prominent way is the global Kp index, which is a 3 h time interval-based indicator to characterize a geomagnetic storm [13–16]. TABLE 1 lists the Kp values and the classifications of the geomagnetic activity [5].

*TABLE 1: Kp values and classification of geomagnetic activity*

| | **WEAK** | | | | | | | | | **MODERATE** | | | | | | | | | **STRONG** | | | | | | | | |
|---|---|---|---|---|---|---|---|---|---|---|---|---|---|---|---|---|---|---|---|---|---|---|---|---|---|---|---|
| **KP** | 0 | | | 1 | | | 2 | | | 3 | | | 4 | | | 5 | | | 6 | | | 7 | | | 8 | | | 9 | |
| | o | + | - | o | + | - | o | + | - | o | + | - | o | + | - | o | + | - | o | + | - | o | + | - | o | + | - | o |

The Kp values are calculated with measurements from 13 observatories worldwide considered, which means Kp is a global index and local GMD impacts can deviate from this. Some research groups are working on local Kp indices

but have not yet concluded their work.

There are other indices, e.g., Dst – disturbance storm time, however, storm predictions mostly only use Kp or parameters derived from Kp [17]. The US National Oceanic and Atmospheric Administration NOAA classifies geomagnetic storms in scales from G1 for minor to G5 for extreme, but this scale again is based on Kp [18].

Space weather prediction is growing in importance, as the impact of solar storms on infrastructure, satellites, GPS, etc. directly influences daily lives. The two main questions arising from the observation of a CME are '*When will it hit Earth?'* and '*What will hit earth*?' For the timing question, [19] summarizes several methods that predict the impact time and concludes a wide variation of ±20 h of the forecasted and real impact time on Earth. The CME scoreboard [17] displays several methods, the predicted arrival time and the predicted Kp. For the impact predictions, knowledge about the CME magnetic field structure is crucial, especially the direction of the $B_z$ component is important. Although there is a lot of recent research on $B_z$ predictions [20, 21], the complexity of the solar wind is not yet understood. Another impact prediction approach is used in [22]: Solar wind data, measured via a satellite at Lagrange point L1 (which is a stationary point between the Sun and Earth), and GIC measurements are used to train a machine learning algorithm with events from the past. The trained model afterward can predict GICs and forecast the impact on power grids.

During the interaction of the solar wind with the Earth's magnetic field, various effects occur. The aurora borealis is one of the effects which is the result of the energization of particles in the atmosphere. The occurrence of the aurora in unusual regions was one of the first indicators of the impact of solar storms on human infrastructure and will be discussed in the next section.

## 2.2 Historical Analysis of Geomagnetic Disturbances

Solar cycles have been explicitly investigated and enumerated since the 18th century. In the following, several GMD-related events are described. The impacts reach from disturbed telecommunication systems in the 19th century up to regional blackouts in the late 1980s.

### 2.2.1 England 1847

Solar cycle 9 had a rising edge in 1847. Spontaneous deflections of telegraph needles were observed in the mid-1800s in England. On the 19th of March 1847, strong disturbances occurred on telegraph lines in central England [23]. During the interferences, an aurora was visible in England and unusual disturbances of magnetic needles occurred in England and abroad [23]. Further investigations showed the influence on isolated and grounded telegraph lines and the discovery that only lines connected to ground on both sides were affected.

### 2.2.2 Carrington Event 1859

On September 1st 1859, a short but impressive disturbance on the sun was observed around 11:20 GMT by [24]. The newspaper Daily Chronicle & Sentinel [25] reported about the conversation between two operators of the American telegraph lines in Boston and Portland. The batteries, that were used to operate the line, were disconnected in both stations, however, the operators were still able to communicate. This was the first documented conversation enabled by auroral currents. However, damages to telegraph stations were reported as well. The aurora borealis was seen in unusual southern regions e.g., in Cuba [26].

Similar phenomena and problems were also reported in Europe, North America and Australia during the active phase of the sun in August and September 1859 [27]. The Carrington Event belongs to Solar Cycle 10.

### 2.2.3 Transatlantic communication lines 1958

A magnetic storm in February 1958 (solar cycle 19) led to troubles on the first transatlantic telephone line between Scotland and Newfoundland. The communication on the 1956 newly installed line was disrupted for about one hour [28]. But not only intercontinental lines were affected, also telegraph lines in Sweden were disturbed by voltage swings and even fires in cables [28]. Additionally, the magnetic disturbances led to a Blackout in Toronto, Canada, during which the auroral lights were seen in the dark of the night. [29]

### 2.2.4 Hydro Quebec 1989

The Hydro-Quebec Blackout is probably the solar event with the highest impact on Earth in recent human history. It started on the 6$^{th}$ of March 1989 during solar cycle 22 with the appearance of a highly active sunspot region on the sun and its movement towards the side facing the Earth until the 18$^{th}$ of March. During these days, several flares, including more than 11 X-class flares, occurred and led to disturbances on earth and earth-near space [30]. Auroras were visible in unusual latitudes, e.g. London, Texas, Cancun and Grand Cayman Islands [31].

Not all solar flares are accompanied by CMEs, however, because of the related disturbances on Earth, the flares on the 10$^{th}$ and 12$^{th}$ of March are considered to be the source of the geomagnetic storms on Earth on the 13$^{th}$ of March [30].

The disturbances in Hydro-Quebec's power system started on the night of 12$^{th}$ to 13$^{th}$ March (EST, Eastern Standard Time) with instabilities, which were corrected by the system operators. A sudden magnetic variation at 2:44 EST (7:44 UTC) led to trippings of static compensators because of overvoltages and overcurrents [32]. The loss of the compensators in combination with the increased reactive power demand of saturated transformers led to severe voltage problems [33]. Shortly after five 735-kV lines between the major generation side in the north and the demand spots in the south tripped, frequency and voltage in the whole Hydro-Quebec system dropped, leading to automated load shedding procedures. The taken actions were not able to compensate the difference between load and generation, leading to a complete collapse of the Hydro-Quebec grid [33]. Among others, Montreal and Quebec City were cut from power supply, leaving around 9 million people without power. The majority of customers were resupplied after 9 hours [31].

The blackout of Hydro-Quebec was certainly the most serious impact of the solar storm, however, there were also disturbances in other power grids: Several lines in Sweden tripped at the same time and capacitor banks and lines tripped all over the US, fortunately leading only to small and short power interruptions [31].

### 2.2.5 New Zealand November 2001

The north and south Islands of New Zealand are connected via a HVDC link. As DC stray currents enter HVAC transformers, a neutral point monitoring system was established early. Because of its position in medium latitude, the GIC risk was considered low, however, on the 6$^{th}$ of November 2001 (solar cycle 23), a solar storm led to disturbances in New Zealand's power grid. Several SVCs and Buchholz relays tripped and a transformer was destroyed, fortunately, a blackout could be prevented. The amplitudes of measured neutral point currents were in the range of 20-30 Ampere, unfortunately, the faulty transformer was not monitored [34].

### 2.2.6 Halloween Storm 2003 in Sweden

The so-called Halloween Storm from 29-31 October 2003 (solar cycle 23) was a solar storm that impacted mostly southern Sweden, leading to a local blackout in the city of Malmö. [35] quantifies this storm as a 1 in 10 years event,

therefore not unlikely to happen in each solar cycle, however, no storm with this impact occurred since 2003.

Between October 26 and November 5, five CMEs arrived at Earth caused by a highly active region on the sun. Two of these CMEs produced Kp values of 9 [10]. The first major CME hit Earth at 6:15 UT on October 29, leading to major disturbances in the Earth's magnetic field. However, no major problems occurred in the Swedish power grid and only a line tripping and higher temperatures were reported [36]. The second CME arrived at 20:04 UT on October 30 with a maximum magnetic field deviation $\Delta B_x$ of 400 nT/min, resulting in induced electric fields of 2 V/km. [10]. This second CME caused several problems, including the disconnection of several transformers and 130 kV lines. The tripping of a 130 kV line in the city of Malmö caused a power outage for 50.000 customers for 20 to 50 minutes. Saturated transformers led to high harmonic distortions in the grid, which led in combination with an abnormal switching state and a high number of cables to the tripping of an overcurrent relay. The relay had a high sensitivity to 150 Hz programmed, leading to the trip during this storm [36].

The Halloween Storm had also an impact on the international space station ISS, where astronauts were advised to seek shelter inside and also 13 nuclear power reactors in the US took precautionary actions to prevent impacts [37].

### 2.2.7 South Africa after 2003

Around 2003, there were 18 transformers in South Africa regularly checked for their condition, some of them with on-line DGA (dissolved gas analysis). After the Halloween storm in October 2003, the levels of dissolved gasses rose rapidly. Several transformers had to be taken out of service because of high DGA levels and paper insulation failures. [38]

### 2.2.8 Austria 2014

During the commissioning of a new transformer in the Austrian power grid in 2014, unexpected high noise levels occurred. Investigations on the cause of this noise led to measured DC currents in the transformer neutral point. The analysis of the measured currents and the comparison with the geomagnetic activity index showed a correlation [1]. This was the beginning of GIC investigations in Austria.

### 2.2.9 Future Storms

There is ongoing progress in the prediction of future solar storms. Based on the last solar cycles, solar prediction models, e.g. [39, 40], deliver forecasts on the number of sunspots in the upcoming solar cycle 25. The website [41] shows the current predictions from NOAA, NASA and ISES. However, as shown in [42] the predictions on the upcoming solar maximum differ in a wide range.

## 2.3 Effects of LFC on Transformers

Low frequency currents enter the power grid through grounded transformer neutral points. As depicted in Figure 1, LFCs can flow through transmission lines, split and distribute at the next substation and enter or leave the power grid.

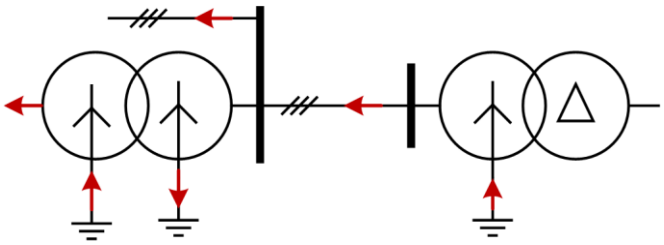

*Figure 1: Paths for low frequency currents*

The frequency spectrum of these currents contains components typically between 0.01 mHz and 1 Hz [43] and far below the grid operating frequencies of 16.7, 50 or 60 Hz. A detailed description of the frequency spectra can be found in section 4 of this thesis. The analyzed LFCs can therefore be treated as DC for further analysis of the influence on transformers. The DC, flowing through the transformer windings, leads to a superimposed direct flux in the transformer. During normal operation, the operating point of the transformer is below the knee-point of the saturation curve in the linear area and an alternating flux (AC flux) leads to an AC magnetizing current (see Figure 2 left picture). If there is a direct flux, caused by neutral point currents, the flux is shifted and the transformer operates partly in the saturation area of the saturation curve (see Figure 2 right picture). Due to the saturation, the magnetizing current is highly distorted.

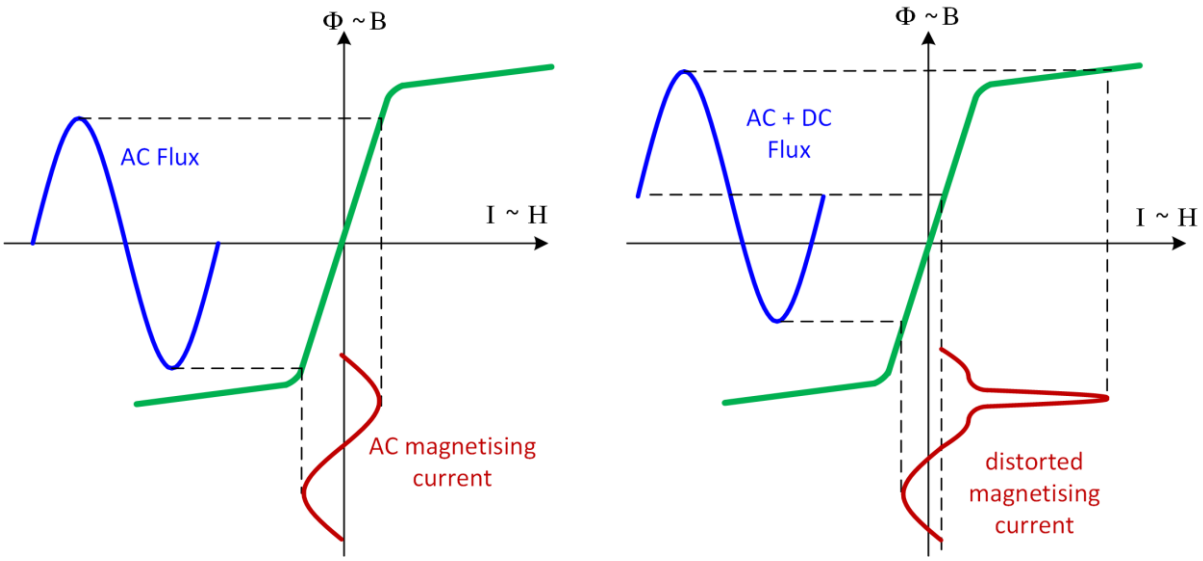


*Figure 2: Half-cycle saturation due to superimposed direct flux*

This is called half-cycle saturation, semi saturation or part saturation. The influence of the distorted magnetizing current can be analyzed best with a Fourier analysis.

Every periodic signal (function) *f(t)* can be described as a Fourier series, which is the sum of trigonometric functions with a fundamental frequency of $\omega_1 = 2\pi f_1$ and its harmonic order frequencies:

$$f(t) = \frac{A_0}{2} + \sum_{\nu=1}^{\infty} A_\nu \cos(\nu \cdot \omega_1 t) + B_\nu \sin(\nu \cdot \omega_1 t) \tag{1}$$

The frequency components can be divided into different categories:

- **Fundamental frequency** $f_1$ is the rated frequency in power grids with 16.7, 50 or 60 Hz.
- **Harmonics** are spectral components with frequencies being integer multiples of the fundamental frequency

- **Interharmonics** are spectral components with frequencies between integer harmonics
- **Subharmonics** have frequencies below the fundamental frequency

In the same way as the fundamental frequency can be transformed into symmetrical components in three-phase systems, harmonics can also be categorized into zero, positive and negative sequences.

- Harmonics with order $\nu = 3k, k=1,2,3...$ ($\nu$ = 3,6,9…) are a **zero sequence**
- Harmonics with order $\nu = 3k+1, k=1,2,3...$ ($\nu$ = 4,7,9…) are a **positive sequence**
- Harmonics with order $\nu = 3k-1, k=1,2,3...$ ($\nu$ = 5,8,11…) are a **negative sequence.**

$$f(t) = -f(t+\frac{T}{2}) \tag{2}$$

If equation (2), where T is the cycle length of the fundamental, is satisfied, which means that the positive and negative half-waves are equal beside the sign, then only odd harmonics are present in the power grid. However, in the case of half-cycle saturation this is not valid anymore due to the DC offset.

The saturation behavior of the transformer is highly dependent on the transformer magnetizing curve and hence on the transformer type. The four main/commonly used transformer construction types are shown in Figure 3. Due to the different flux paths in each transformer type, the hysteresis curve and saturation are different for each type. Hence calculation of harmonic emissions is different for each type.

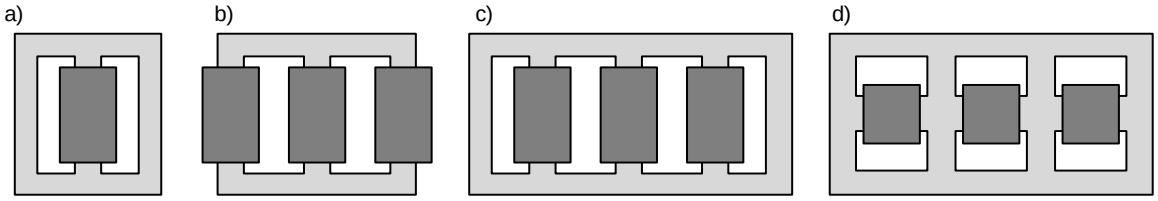


*Figure 3: Transformer types: a) 1-phase, b) 3-phase 3-limb, c) 3-phase 5-limb, d) 3-phase shell form*

Depending on the core type, mathematical calculations of the saturation effect in [44] linearize the hysteresis curve with piecewise linear representations. The simplified results show, that single-phase and 3-phase shell form transformers are most susceptible to DC saturation, which is mainly caused by the magnetic flux path.

Because of the different transformer types, it is difficult to give a general formulation for harmonics calculation which could be used without detailed information about the transformer hysteresis. Additionally, there are very different types of result representation in literature. Nevertheless, the principal approach is always the electro-magnetic modeling to simulate the excitation current of the transformer [45, 46]. As will be shown later in section 6.2, data from real transformers in the Austrian transmission grid is used. The model behind this simulation uses detailed information about the transformer construction to create a model of flux branches with magnetic resistances where the link between electrical winding and magnetic flux is included [46]. After the determination of the magnetic resistances, which are mostly design-dependent, the influence of DC on the exciting current can be calculated. From the change in the exciting current, harmonics in dependence on the saturation, and hence in dependence on the DC bias, can be derived. Again, depending on the transformer type, the lower harmonics often tend to increase linearly with increasing DC (or can be well approximated linearly). Single phase types (Figure 3 a)) show the highest increase rates [44]. Higher harmonics show more complex behaviors.

As the magnetizing current of the transformer, which is in phase with the flux, increases, also the reactive power demand of the transformer rises. This additional reactive power demand influences the voltage in the grid. If there is not enough reactive power reserve available, e.g. the generators operate already at the reactive power limits, the

voltage in the grid decreases, which leads to further disturbances. Voltage stability problems or voltage collapses are possible worst cases, as happened in Canada in 1989 [32].

Transformers create different types of sound and noise: load sound, no-load sound and auxiliary noise, e.g. from cooling fans. The load sound is caused by the Lorentz forces, which is caused by the load current, acting on the windings and leading to vibrations therein [47]. The vibrations propagate through the inner parts of the transformer and to the surrounding air, i.e. pressure changes in the air, and so to noise. The main frequencies of load current noise are therefore the fundamental and odd harmonics. The core movement is caused by magnetostriction. The Weiss' domains in a ferromagnetic material rotate or change their boundaries when an external magnetic field is applied. This movement leads to mechanical stress and hence to noise [48]. The construction of the transformer has a major influence on the strain, and hence on the noise levels. Detailed models of transformers can analyze this behavior, identify the main noise generators and improve the transformer design afterward [49]. As this happens twice per period, the frequency of the no-load sound is double fundamental.

When the magnetizing current is distorted because a DC offset is present, this means also the frequency components of the transformer noise change, which is hear- and measurable. Even harmonics are always present in the transformer sound whereas odd harmonics show a special operating condition. The frequency analysis of transformer sounds can therefore indicate DC bias in transformers [43].

The influence of LFCs on transformer heating and internal hot spots can be found in Literature, e.g. [38, 46, 50, 51], but is not further discussed in this thesis.

## 2.4 GIC Calculation

The calculation of GICs is typically split into two parts: The first part is the calculation of an electric field, which results from the changes in the Earth's geomagnetic field. There are well-known methods, e.g. the plane wave method [52] or new approaches based on machine learning algorithms [22]. This will be discussed in sections 2.4.1 and 2.4.2. The second part of GIC estimation is the electrical engineering calculation, which uses the determined or predicted geoelectric fields to calculate currents in transformers, lines and substation grounding systems. This part also includes the determination of the resulting effects on transformers and transducers. Again, there are several methods to calculate these currents and effects, which will be discussed in section 2.4.3. To reduce the impact of GICs on power grids, mitigation technologies with different approaches were developed. An overview of already existing methods is given in section 2.5.

### 2.4.1 Magnetic Field Measurements

The basis for all GIC calculations is the knowledge about the earth's magnetic field change. The most common and well-known method is the magnetic field measurement at ground level through observatories. INTERMAGNET is a global network of ground-based observatories and was founded in 1991 to establish standards for measuring, recording and transmitting magnetic observatory data [53]. INTERMAGNET [54] is also a portal and web service, which provides (in 2019) ground-magnetic field measurements from 129 observatories all over the world. One of these observatories is the Conrad Observatory (IAGA Code WIC) in Austria located south-west of Vienna [55]. The directional variations of the Earth's magnetic field are measured in 1-second-samples and provided in xyz-direction. The coordinate system is defined as follows [52]:

- x… northward direction
- y… eastward direction
- z… vertically into the Earth

More information about the used sensors, location, geological structure, baseline values, etc. can be found in [55].

## 2.4.2 Electric Field Calculation

### 2.4.2.1 General Formulation

This section gives a brief introduction to the calculation of induced electric fields with the most important equations. A detailed description of the mathematical formulation can be found in literature, e.g., [52, 56–58]. The basis for the calculation of the influence of geomagnetic variance on power grids are Maxwell's equations, shown in the differential form in equation (3) - (6).

$$\boldsymbol{\nabla} \times \mathbf{H} = \mathbf{J} + \frac{\partial \mathbf{D}}{\partial t} \tag{3}$$

$$\boldsymbol{\nabla} \times \mathbf{E} = -\frac{\partial \mathbf{B}}{\partial t} \tag{4}$$

$$\boldsymbol{\nabla} \cdot \mathbf{B} = 0 \tag{5}$$

$$\boldsymbol{\nabla} \cdot \mathbf{D} = \rho \tag{6}$$

$$\mathbf{D} = \varepsilon \mathbf{E} \tag{7}$$

$$\mathbf{B} = \mu_r \mu_0 \mathbf{H} \tag{8}$$

$$\mathbf{J} = \sigma \mathbf{E} \tag{9}$$

For practical usage, the equations need a reformulation and assumptions must be made:

- The time variation can be assumed as $e^{j\omega t}$ [56]
- The displacement current can be neglected due to the low frequencies and high conductivities [5, 56]
- The relative magnetic permeability is nearly $\mu_r \approx 1$, as the conductive ground is assumed to be non-magnetic
- The conductivity is uniform, therefore $\boldsymbol{\nabla} \cdot \boldsymbol{E} = 0$ [56]

With these assumptions and the material equations (7) - (9), (3) and (4) can be formulated as:

$$\boldsymbol{\nabla} \times \mathbf{B} = \mu_0 \sigma \mathbf{E} \tag{10}$$

$$\boldsymbol{\nabla} \times \mathbf{E} = -j\omega \mathbf{B} \tag{11}$$

The substitution of (11) in (10) and vice versa leads to:

$$\boldsymbol{\nabla}^2 \mathbf{E} = j\omega\mu_0\sigma \mathbf{E} \tag{12}$$

$$\boldsymbol{\nabla}^2 \mathbf{B} = j\omega\mu_0\sigma \mathbf{B} \tag{13}$$

If the variations in the horizontal plane are very small compared to the variations in depth, (12) has a solution in the form of (14), with p as the complex skin depth [56] and superscript 0 indicating the surface field. Similar considerations from [56] also lead to (15).

$$\mathbf{E} = \mathbf{E}^0 \, e^{-\frac{z}{p}} \tag{14}$$

$$\mathbf{B} = \mathbf{B}^0 \, e^{-\frac{z}{p}} \tag{15}$$

The assumption of minimal changes in the horizontal electric field also leads to:

$$\nabla \times \mathbf{E} = \det\begin{pmatrix} \mathbf{e_x} & \mathbf{e_y} & \mathbf{e_z} \\ \frac{\partial}{\partial x} & \frac{\partial}{\partial y} & \frac{\partial}{\partial z} \\ E_x & E_y & E_z \end{pmatrix} = \det\begin{pmatrix} \mathbf{e_x} & \mathbf{e_y} & \mathbf{e_z} \\ 0 & 0 & \frac{\partial}{\partial z} \\ E_x & E_y & E_z \end{pmatrix} = -\frac{\partial E_y}{\partial z}\boldsymbol{e_x} + \frac{\partial E_x}{\partial z}\boldsymbol{e_y} \tag{16}$$

For further investigations, the calculation is split into two cases with an electric field in x-axis respectively y-axis direction only:

Case 1:
$$\mathbf{E^0} = \begin{pmatrix} \mathbf{E_x^0} \\ 0 \\ 0 \end{pmatrix} \tag{17}$$

Case 2:
$$\mathbf{E^0} = \begin{pmatrix} 0 \\ \mathbf{E_y^0} \\ 0 \end{pmatrix} \tag{18}$$

The substitution of (14) in (11) with the assumptions in the two cases and $Z = j\omega p \mu_0$ leads to:

Case 1:
$$\frac{\partial\left(E_x^0\, e^{-\frac{z}{p}}\right)}{\partial z}\mathbf{e_y} = -j\omega\mathbf{B_y} \tag{19}$$

$$E_x^0 = \frac{Z}{\mu_0}B_y^0 \tag{20}$$

Case 2:
$$-\frac{\partial\left(E_y^0\, e^{-\frac{z}{p}}\right)}{\partial z}\mathbf{e_x} = -j\omega\mathbf{B_x} \tag{21}$$

$$E_y^0 = -\frac{Z}{\mu_0}B_x^0 \tag{22}$$

This shows the rotation, meaning that magnetic field changes in x direction lead to electric fields in y direction.

The relationship between the complex skin depth p, the penetration depth $\delta$ and the earth's conductivity is given with equations (23) and (24).

$$p = \frac{\delta}{\sqrt{2}}e^{-j\frac{\pi}{4}} \tag{23}$$

$$\delta = \sqrt{\frac{2}{\omega\mu_0\sigma}} \tag{24}$$

This formulations from equation (10) to (24) can also be written as equation (25) to (27) [58], where $Z(\omega)$ describes the frequency depended total earth impedance, which will be further discussed in the following section.

$$\mathbf{E}(\omega) = \mathbf{Z}(\omega) \cdot \mathbf{H}(\omega) \tag{25}$$

$$\mathrm{E_x}(\omega) = \frac{\mathrm{Z}(\omega)}{\mu_0} \cdot \mathrm{B_y}(\omega) \tag{26}$$

$$\mathrm{E_y}(\omega) = -\frac{\mathrm{Z}(\omega)}{\mu_0} \cdot \mathrm{B_x}(\omega) \tag{27}$$

### 2.4.2.2 Earth Modeling

The modeling of earth and the total earth impedance is one of the key factors for GIC calculations. There are different methods to calculate the earth impedance and the resulting electric field, depending on the available data source, desired degree of complexity and especially on the geographic location of the area. Based on [59, 60] there are four main categories of earth modeling, where [60] gives one of the most comprehensive overviews of this topic.

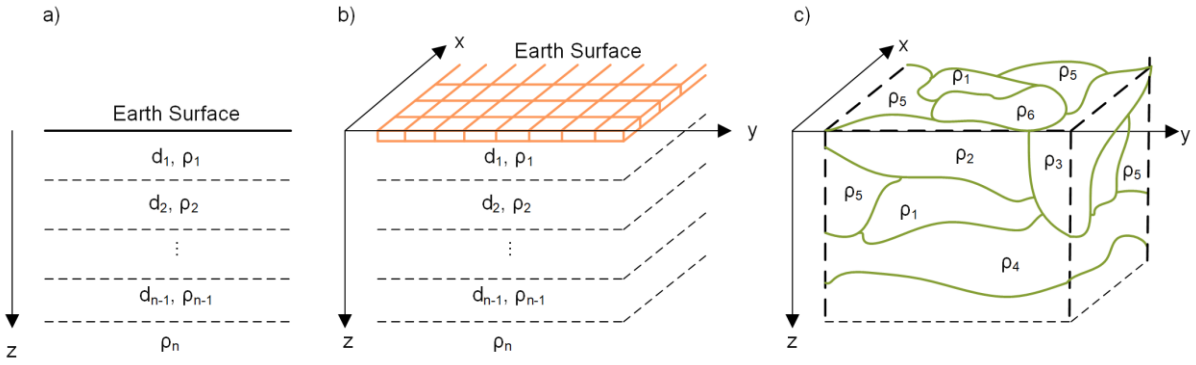


*Figure 4: Earth models: a) 1-D-model, b) 1-D thin sheet, c) 3-D model*

**1-D model and 1-D compilation:** The simplest approach to model the conductive earth is by assuming the earth as a homogeneous half-space with the resistivity ρ (or conductivity σ). There are no lateral changes in the earth's structure and no reflected waves occur. By adding different layers in depth with different thicknesses $d_x$ and resistivities $\rho_x$, as depicted in Figure 4 a), variations in z-direction can be modelled. For this method, a large database of earth structures is available, e.g. for Europe the EUROHM-Data [61] (that will be used in this work) or the US [62]. The lowest layer n describes an infinite deep layer. The following calculation of the earth impedance is based on [5, 59, 63]:

The calculation of the total earth impedance with a layered 1-D model, with m different layers starts with the bottom layer m:

$$Z_m(\omega) = \sqrt{j\omega\mu_0\rho_m} \tag{28}$$

All layers above the lowest layer are then calculated using Snell's law, considering travelling and reflected waves.

$$Z_{n(\omega)} = \left(\frac{1+\alpha_n(\omega)}{1-\alpha_n(\omega)}\right) Z_{0n}(\omega), n = m, m-1, \dots, 1 \tag{29}$$

with:

$$\alpha_n(\omega) = R_{i+1}(\omega) \cdot e^{-2\gamma_n d_n} \tag{30}$$

$$R_{n+1}(\omega) = \left(\frac{Z_{n+1}(\omega) - Z_{0n}(\omega)}{Z_{n+1}(\omega) + Z_{0n}(\omega)}\right) \tag{31}$$

$$\gamma_n(\omega) = \sqrt{\frac{j\omega\mu}{\rho_n}} \tag{32}$$

$$Z_{0n}(\omega) = \sqrt{j\omega\mu\rho_n} \tag{33}$$

With these formulations, the equivalent earth impedance can be calculated and used with equations (26)-(27) to calculate the resulting electric field on the Earth's surface. It is dependent on the angular frequency ω and the different conductivities in depth.

**1-D and thin-sheet approach**: This method includes a 2-dimensional structure on top of a 1-D earth model, as depicted in Figure 4 b). It was introduced by [64] and further improved, adapted and expanded by [65, 66] and others and used by [2] for calculations in Austria. Because of the lateral changes in conductivity on the top layer, it is often used for complex surface structures e.g. coastlines. Therefore this approach is often used to model geographical islands, e.g. United Kingdom [67, 68], and New Zealand [69]. There are numerous studies available, showing the benefits of this method, e.g. [67, 69, 70]. However, this method needs more and detailed data about the Earth's structure.

**3D modeling**: The most thorough method to model induced electric fields is a fully 3-D model of the earth. As depicted in Figure 4 c), this modeling approach takes horizontal and vertical conductivity changes into account. New magneto telluric measurement survey made this approach, especially in recent years more common. There are fully 3-D models available for e.g. UK [71], USA [72], Sweden [73], Japan [74] or Australia [75], and global approaches [76].

### 2.4.3 Calculation of Geomagnetically Induced Currents in Power System Assets

With the electric field known, either from different modeling approaches from section 2.4.2 or directly assumed as a given quantity representing a worst-case scenario, currents in lines, transformers and substation grounding systems can be calculated. There are different calculation methods known, which will be described in the next section. With these currents, especially transformer currents, the impact on the transmission grid can be estimated.

#### 2.4.3.1 Induced EMF and Driving Voltage Sources

As described above, changes in the magnetic field lead to an induced electric field. Applying this to a conductive closed loop, the electromotive force emf drives a current. As pointed out in literature [5, 77], this is sometimes misunderstood as an induction in the loop between earth and conductive wire or as a field gradient on the earth's surface potential.

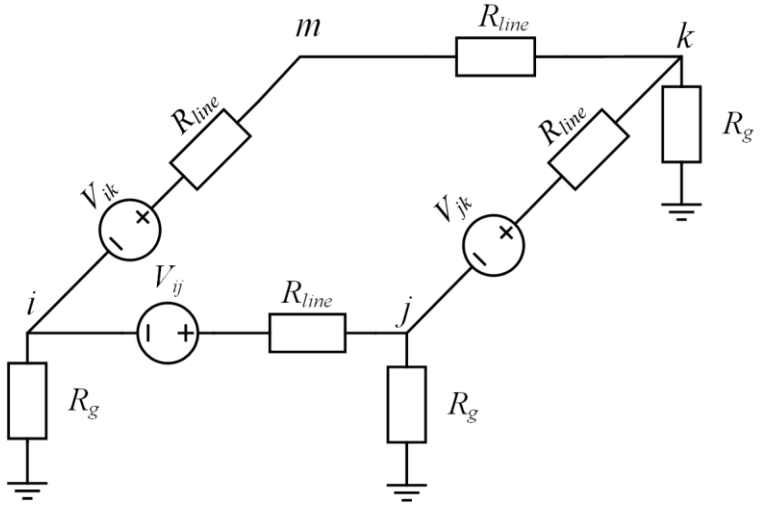


*Figure 5: Schematic of induced EMF implementation*

As shown in [77], and Figure 5, the correct implementation of the emf in grid calculation is the modeling as a voltage source in series with the conductive path(e.g. the transmission line). The equivalent voltage between two grounded points in the system is calculated as the integral of the electric surface potential between these points with equation (34).

$$V_s = \int_j^i \mathbf{E} \cdot d\boldsymbol{s} \tag{34}$$

By using the plane wave method with 1-D earth layers, the electric field is homogeneous and constant in the calculated area and (34) can be reformulated to (35) where $E_x$ and $E_y$ are the electric field in north- and eastward direction and $L_x$ and $L_y$ are the distances between the two points i and j in the respective direction.

$$V_s = \int_j^i \mathbf{E} \cdot d\boldsymbol{s} = E_x \cdot L_x + E_y \cdot L_y \tag{35}$$

#### 2.4.3.2 Current Calculation

There are mainly three methods to calculate GICs in power grids: The Lehtinen-Pirjola method, the nodal-admittance method and the calculation via parameter fitting. As these three methods are the most commonly used, they are described in this section. Additionally, there are more recent developments or variations of the three mentioned methods [78].

**Lehtinen-Pirjola**: This method, often referred to as LP-method, was introduced by Lehtinen and Pirjola [79] in 1985 and was the first approach to calculate geomagnetically induced currents. The emf is described by a voltage source in series with the conducting grid assets. The derivation of (36) can be found in [7, 79]. The earthing currents in each node $I^e$ are calculated with detailed knowledge about the network with the network admittance matrix $Y^n$, the earthing impedance matrix $Z^e$ and the information about currents in the assets $J^e$.

$$\mathbf{I}^e = (\mathbf{1} + \mathbf{Y}^n \mathbf{Z}^e)^{-1} \mathbf{J}^e \tag{36}$$

The currents in $J^e$ are calculated via the voltage between two nodes and the connecting resistance. The LP-Method is widely used for GIC calculations e.g. [4, 80–83] to list only a few.

**Parameter fitting:** In this method, used in [84–86], the GIC in a specific transformer j is the linear combination of the electric field in x- and y direction multiplied with the fitting parameters $a_j$ and $b_j$ in equation (37). The electric field is again calculated with the plane wave method. The fitting parameters or substation coefficients are specific for each substation and can be determined with real measurements in power grids.

$$GIC_j = a_j \cdot E_x + b_j \cdot E_y \tag{37}$$

This method has several disadvantages: Only GICs at substations with neutral point measurements can be calculated and as soon as there is any change in the grid topology, the fitting parameters must be calculated again. Additionally, because of limited earth layer modeling, uncertainties caused by the electric field calculation influence the parameter fitting.

**Nodal admittance method**: The nodal admittance method is well known in power systems engineering and also well known in GIC calculations [5, 86, 87]. The following description of this calculation method is based on and mainly taken from [5]:

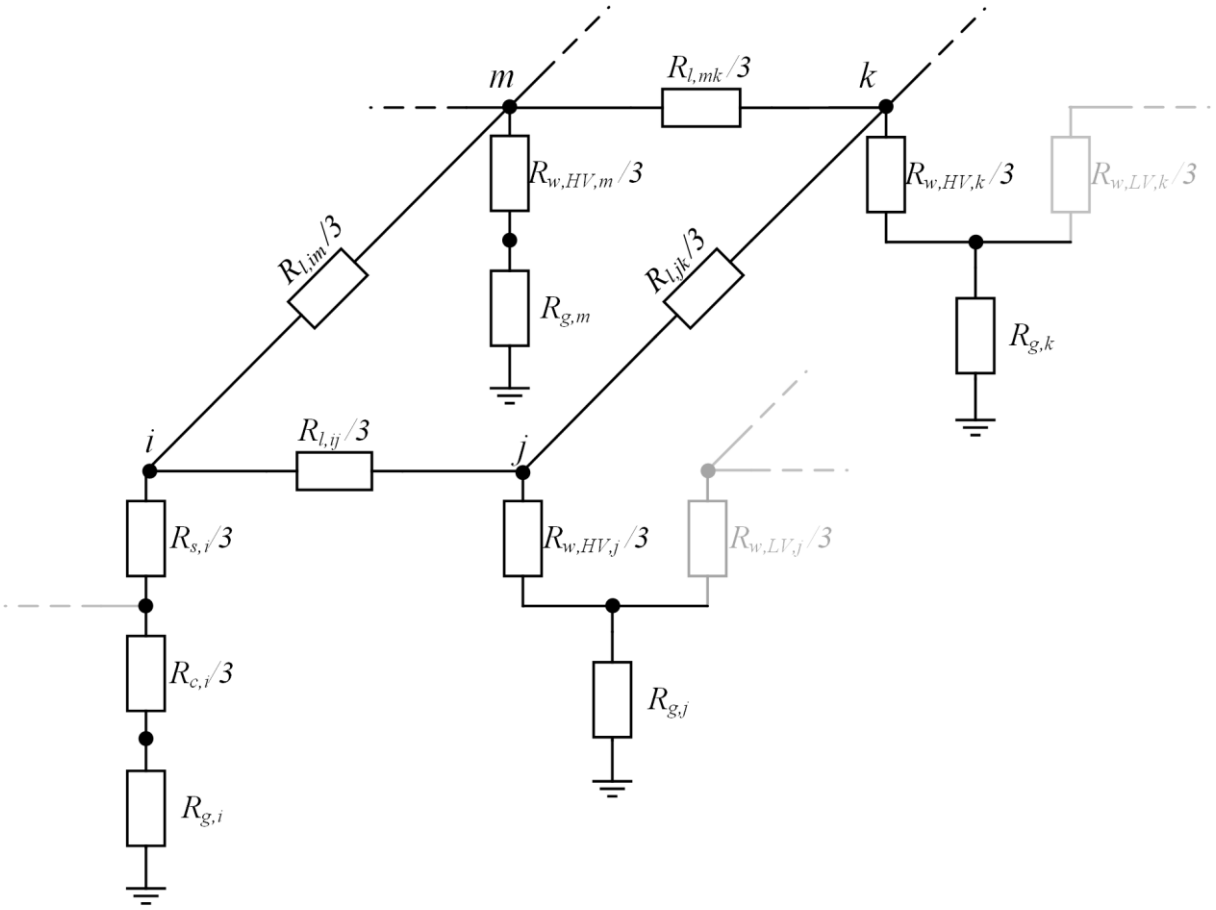


*Figure 6: Grid-schematic for GIC calculations with nodal-admittance method*

The schematic grid in Figure 6 includes all necessary assets for modeling a power system for GIC calculations. All 3-phase devices are replaced by a single impedance, representing a parallel connection of the phase conductors. Because of the low frequency, the power grid can be described as a purely ohmic network, neglecting series inductances. The high voltage level is depicted in black, and the lower voltage level in grey. Beginning on the left in substation i, an autotransformer with the series winding $R_s$ and common winding $R_c$ is shown. The neutral point of the autotransformer is connected to the grounding resistance $R_g$ which represents the resistance of the substation to remote earth (which is not the resistance between substations or to a reference node). Substation i is connected with transmission lines to the substations j and k by the line resistances $R_{l,ij}$ and $R_{l,im}$. In substation j, a transformer with the high voltage winding resistance $R_{w,HV}$ and the low voltage winding $R_{w,LV}$ is connected. The path for LFCs in this transformer type is through the HV-winding to the neutral bus and through the LV-winding into the next voltage level. If the neutral point is grounded, which is normally the case, the neutral bus is again connected through the substation grounding resistance to remote earth. In the transformer in substation m, only the HV winding is affected by GICs, as the LV winding is not connected to the neutral e.g. because of a delta vector group. This is typically the case for generator step-up transformers GSU.

The even distribution of LFCs in the three phases of electric power systems has been under discussion for some time. Due to missing 3-phase DC measurement on high voltage potential, the even distribution has never been proofed, but as the system is more or less symmetrical designed, the assumption may be valid. The optical three-phase measurement device described in 2.6.1.2 may lead to new results, however, the installation of the developed prototype is not finished yet. In this thesis, it is assumed, that LFCs are evenly split on the phases in the three-phase system. Therefore the resistances of transformers and lines are in parallel and can be simply divided by 3.

The following mathematical description of the nodal admittance method for GIC calculation is based on [5]:

**Admittance Matrix Y**

As well-known from electrical power engineering, the admittance matrix Y is constructed according to (38). As the frequency of GICs is very low, Y is only ohmic. For GIC calculations, the grid is split into three matrices, the network admittance matrix $Y_N$, the grounding matrix $Y_G$ and the coupling matrix $Y_C$. The network matrix $Y_N$ includes all nodes where lines and transformers are connected and has the size $N_{net} \times N_{net}$. The grounding matrix $Y_G$ with the size $N_{sub} \times N_{sub}$ includes the substation grounding systems and the coupling matrix $Y_C$ connects the neutral busses with the grounding points of the substations and has the size $N_{net} \times N_{sub}$. The overall admittance matrix is the combination of these three matrices and is constructed as shown with (39).

$$Y_{ij} = \begin{cases} -\frac{1}{R_{ij}}, & i \neq j \\ \sum_{k=1,k\neq i}^{N} \frac{1}{R_{ik}}, & i = j \end{cases} \tag{38}$$

$$\boldsymbol{Y} = \begin{bmatrix} \boldsymbol{Y}_N & \boldsymbol{Y}_c \\ \boldsymbol{Y}_C^T & \boldsymbol{Y}_G \end{bmatrix} \tag{39}$$

The resulting size of Y is $N_N \times N_N$.

**Branch-node Incidence Matrix**

$$BNM = \begin{cases} \frac{1}{R_b}, & sending\ node \\ -\frac{1}{R_b}, & receiving\ node \\ 0, & branch\ not\ connected\ to\ node \end{cases} \tag{40}$$

The directed incidence matrix includes the topology information, at which node a branch starts (entry is 1) and where it ends (entry is -1). It has the size $N_B \times N_N$, where $N_B$ is the number of branches and $N_N$ is the number of nodes. Multiplied with the diagonal branch admittance matrix, we receive the directed, weighted branch-node matrix BNM in equation (40). The structure in (41) is the result of categorizing this into the three categories of Lines, Transformers, and Substations (see Figure 6 for element description). $\mathbf{BNM}_{Lin}$ contains all lines between the different substations, $\mathbf{BNM}_{Tra}$ contains all transformers and $\mathbf{BNM}_{Sub}$ includes all substation grounding resistances.

$$\boldsymbol{BNM} = \begin{bmatrix} \boldsymbol{BNM}_{Lin} \\ \boldsymbol{BNM}_{Tra} \\ \boldsymbol{BNM}_{Sub} \end{bmatrix} \tag{41}$$

The size of the three matrices are $N_{Lin} \times N_N$ for $\mathbf{BNM}_{Lin}$, $N_{Tra} \times N_N$ for $\mathbf{BNM}_{Tra}$, and $N_{Sub} \times N_N$ for $\mathbf{BNM}_{Sub}$, where $N_{Lin}$ is the number of lines, $N_{Tra}$ is the number of Transformers (split into HV and LV side), $N_{Sub}$ is the number of Substations and $N_N$ the number of overall nodes.

**Geographical Distances**

For the calculation of the induced voltage between two substations, the geographical distance between the substations is needed. Taking the non-spherical shape of the earth into account, as it has a smaller radius on the poles than on the equator, the distance calculation from geographical latitude and longitude is not trivial. Based on [88, 89] with the GPS earth model WGS84 the equations (42) - (44) are used for the distance calculation.

$$\phi_{ij} = \frac{lat_i + lat_j}{2} \tag{42}$$

$$L_{x,ij} = (111.133 - 0.56\cos(2 \cdot \phi_{ij}) \cdot (lat_j - lat_i) \tag{43}$$

$$L_{y,ij} = \left(111.5065 - 0.1872\cos\left(2 \cdot \phi_{ij}\right)\right) \cdot \cos\left(\phi_{ij}\right) \cdot \left(lon_j - lon_i\right) \tag{44}$$

In (42), $\Phi_{ij}$ is defined as the mean value of the latitudes of substations i and j. The northward direction x (latitudinal) is described with (43) and the eastward direction y (longitudinal) with (44).

**Network Currents**

After the distances are known and the electric field is calculated, the driving voltage source $V_{s,i}$ between the substations and a reference substation can be calculated with (45). Substation one is chosen as the reference point.

$$\boldsymbol{V}_{s,i} = [\boldsymbol{L}_{x,i} \quad \boldsymbol{L}_{y,i}] \cdot \begin{bmatrix} \boldsymbol{E}_x \\ \boldsymbol{E}_y \end{bmatrix} \tag{45}$$

The electric field values are uniform for the whole grid and have the size $1 \times t$, where t is the investigated time series. The voltage sources are combined into the vector $V_s$ with the size $N_{sub} \times t$.

Using nodal analysis, the resulting currents can be in general described with

$$\begin{bmatrix} 0 \\ \boldsymbol{I}_{Sub} \end{bmatrix} = \begin{bmatrix} \boldsymbol{Y}_N & \boldsymbol{Y}_c \\ \boldsymbol{Y}_C^T & \boldsymbol{Y}_G \end{bmatrix} \cdot \begin{bmatrix} \boldsymbol{V}_N \\ \boldsymbol{V}_S \end{bmatrix} \tag{46}$$

The admittance matrices as well as the driving voltage sources $V_s$ (which is the voltage between a substation *i* and the reference point) are known but all other remaining nodal voltages $V_N$ and the resulting grounding currents are unknown. The remaining nodal voltages $V_N$ can be calculated by reformulating the upper part of equation (46) $0 = Y_N \cdot V_N + Y_C \cdot V_S$ to

$$\boldsymbol{V}_N = -\boldsymbol{Y}_N^{-1} \cdot \boldsymbol{Y}_C \cdot \boldsymbol{V}_S \tag{47}$$

where the resulting vector $V_N$ has the size $N_{net} \times t$.

With all known network voltages and driving voltage sources, the currents in lines, transformers and substation grounding systems can be calculated with

$$\begin{bmatrix} \boldsymbol{I}_{Lin} \\ \boldsymbol{I}_{Tra} \\ \boldsymbol{I}_{Sub} \end{bmatrix} = \begin{bmatrix} \boldsymbol{BNM}_{Lin} \\ \boldsymbol{BNM}_{Tra} \\ \boldsymbol{BNM}_{Sub} \end{bmatrix} \cdot \begin{bmatrix} \boldsymbol{V}_N \\ \boldsymbol{V}_S \end{bmatrix} \tag{48}$$

By replacing $V_N$ with equation (47) and $V_S$ with (45), we receive (49) which shows a direct calculation of the currents in the grid calculated from the electric field in north and eastward directions.

$$\begin{bmatrix} \boldsymbol{I}_{Lin} \\ \boldsymbol{I}_{Tra} \\ \boldsymbol{I}_{Sub} \end{bmatrix} = \underbrace{\begin{bmatrix} \boldsymbol{BNM}_{Lin} \\ \boldsymbol{BNM}_{Tra} \\ \boldsymbol{BNM}_{Sub} \end{bmatrix} \cdot \begin{bmatrix} -\boldsymbol{Y}_N^{-1} \cdot \boldsymbol{Y}_C \\ 1 \end{bmatrix} \cdot [\boldsymbol{L}_x \quad \boldsymbol{L}_y]}_{[C]} \cdot \begin{bmatrix} \boldsymbol{E}_x \\ \boldsymbol{E}_y \end{bmatrix} \tag{49}$$

The matrix dimensions of equation (49) are the following: $\begin{bmatrix} \boldsymbol{I}_{Lin} \\ \boldsymbol{I}_{Tra} \\ \boldsymbol{I}_{Sub} \end{bmatrix}$ has the size $N_B \times t$ where $N_B$ is the number of branches, $\begin{bmatrix} \boldsymbol{BNM}_{Lin} \\ \boldsymbol{BNM}_{Tra} \\ \boldsymbol{BNM}_{Sub} \end{bmatrix}$ has the size $N_B \times N_N$, $\begin{bmatrix} -\boldsymbol{Y}_N^{-1} \cdot \boldsymbol{Y}_C \\ 1 \end{bmatrix}$ has the size $N_N \times N_{sub}$, $[\boldsymbol{L}_x \quad \boldsymbol{L}_y]$ has the size $N_{sub} \times 2$ and $\begin{bmatrix} \boldsymbol{E}_x \\ \boldsymbol{E}_y \end{bmatrix}$ has the size $2 \times t$. Parts of this equation are also notated as system matrix C, which is used later.

The main difference between the LP-Method and the calculation through nodal-admittance analysis is the placement of the driving voltage source and the accompanying definition of a reference point. As pointed out by [90], as long as the electric field is considered uniform, the two methods are completely equal. As soon as the electric is considered more realistic or is not constant over the area under investigation, the integration of the electric

field is path-dependent. This means the calculation of the driving voltage source to a reference point in equation (35) is not correct, as no electric field change can be considered. In this case, the LP-Method can still be used, as long as during the electric field calculation the non-uniformity is considered.

#### 2.4.3.3 Reactive Power Calculation

Transformers under DC-bias operate in the saturation area of the magnetizing curve. This leads to distortions in voltage and current waveforms, as described earlier. Due to the distortion, the no-load reactive power losses of the transformer increase. As the additional reactive power loss of transformers $Q_{loss}$ leads to a decreased fundamental voltage, only the fundamental of the reactive power loss is considered in most calculation approaches, especially if system-wide calculations are done [44, 45, 91, 92]. These approaches use the linear reactive power calculation in (50). Some approaches consider the fundamental voltage as constant with 1 p.u. and therefore neglect $V_{pu}$ in this equation. In any case, the factor K must have the correct unit, usually Mvar/A. The current $I_{GIC}$ is the effective DC in the transformer in A, causing the saturation.

$$Q_{loss} = V_{pu} \cdot K \cdot I_{GIC} \tag{50}$$

The calculation of $I_{GIC}$ is dependent on the transformer type, e.g. if it is a two-winding transformer or an autotransformer. Factor $K$ describes the slope of the reactive power, depending on DC in the transformer. This value depends on the transformer type and is usually determined with simulations [44]. During system-wide studies, the factor K is not always known for all transformers, therefore standard values are proposed in literature. As the tertiary winding of transformers is mostly connected in delta, no GIC is flowing through this winding and no reactive power demand occurs. The two used types in this thesis are shown in Figure 6. The left schematic depicts a two-winding transformer with a high voltage connection HV and a low voltage side LV. The respective resistances and number of turns are $R_{HV}$, $n_{HV}$ and $R_{LV}$, $n_{LV}$. The neutral point is connected to ground via the substation earthing resistance $R_G$. On the right side in Figure 6, the schematic of an autotransformer is shown. The high voltage terminal is connected via the series winding ($R_S$ and $n_S$) to the low voltage terminal LV. The common winding with the resistance $R_C$ and number of turns $n_c$ connects the low voltage side with the neutral point.

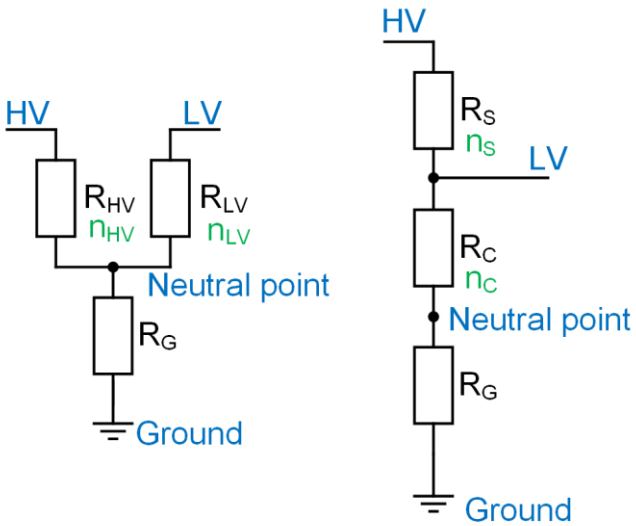


*Figure 7: Transformer schematics for linear reactive power demand calculation*

The calculation of the effective current is based on [91] and shown in equations (51) - (54). With these calculations, the currents in the low and high (series and common) windings are combined and transformed to one side.

Two winding transformers [91]:

$$n = \frac{n_{HV}}{n_{LV}} = \frac{V_{HV}}{V_{LV}} \tag{51}$$

$$I_{GIC} = \left| \frac{n\, I_{HV} + I_{LV}}{n} \right| \tag{52}$$

Autotransformer [91]:

$$n = \frac{n_S + n_C}{n_C} = \frac{V_{HV}}{V_{LV}} \tag{53}$$

$$I_{GIC} = \left| \frac{(n-1)I_S + I_C}{n} \right| \tag{54}$$

A detailed analysis of this calculation and proposed changes is given in section 6.2.

The resulting currents $I_{GIC}$ and $Q_{loss}$ respectively can now be used in system studies to analyze the influence of the additional reactive power demand on voltage and system stability. Especially in cases, where already high reactive power demand is present in the grid, these additional losses can lead to severe problems in the grid. In the author's opinion, it is important to calculate the combined impact of all additional reactive power demands of transformers in the grid, as the sum of $Q_{loss}$ may lead to disturbances although the single values of each transformer are low. Additionally, voltage problems may not arise from problems in one national grid, but in grids nearby, which means a total system analysis is important.

## 2.5 Countermeasures against LFC

LFC mitigation, elimination or reduction strategies can target different assets in power grids. There are six main strategy classes:

- Elimination of neutral connections
- Corrective line switching
- Series compensation along transmission lines
- DC diverters
- DC-compensated transformers
- Blocking devices in neutral connections

In the following, the state of the art of these six mitigation strategies is described.

### 2.5.1 Elimination of Neutral Connections

The objective of the neutral point elimination method is to operate lines with a single neutral point on one side of the line and thereby eliminating the path for GICs [93]. The disconnection of a neutral point is not always possible, as e.g., autotransformers are most of the time neutral point grounded to limit overvoltages. Nevertheless there are other approaches proposed in literature: As shown in Figure 8, the elimination of neutral connection is accomplished by switching the transformer topology from a typical wye-wye connection to a delta-wye connection or by disconnecting the neutral point.

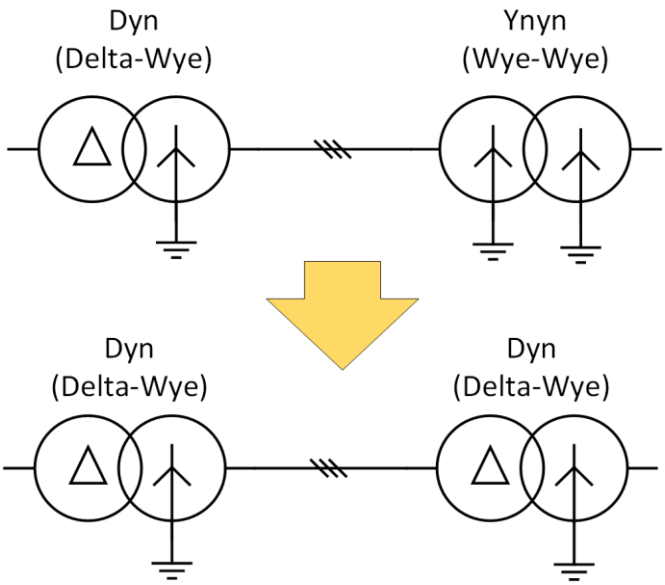


*Figure 8: Elimination of neutral connections*

There is no path for the GIC to flow through the grid if the line is only a point-to-point connection. This approach, however, has several drawbacks. Delta connections cause a phase shift, which makes connected grids more complex [93]. This vector group's topology has additional costs for new transformers and increases the risk of overvoltages during faults, which can harm assets.

Therefore, this approach should only be viewed as theoretical.

### 2.5.2 Series Compensation

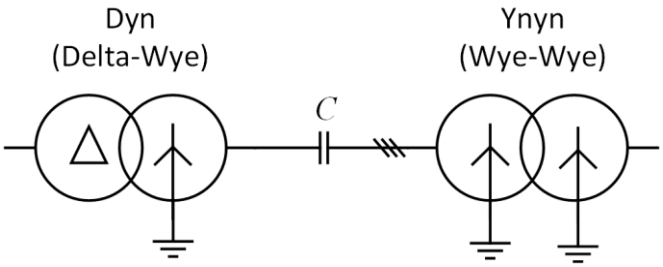


*Figure 9: Series compensation of transmission lines*

Another strategy for reducing the impact of GICs is to install mitigation equipment alongside with transmission lines. The devices can be capacitors in series [94], as shown in Figure 8, or variable series resistances with capacitors [95], which are proposed to avoid affecting normal operation. With these in-series connected devices, the flow of GICs on single lines can be decreased. However, during regular operation, this might cause grid disturbances. In a meshed connected power grid, the GIC may also distribute differently and cause disruptions on other lines, which are not protected with a mitigation device.

### 2.5.3 DC Diverters

Special shunt transformers called DC-diverters or grounding transformers are connected in substations to decrease the GIC stress on power transformers. The transformer that is protected has a higher resistance than the DC-diverter. The diverter receives the majority of the GIC, which reduces the GIC stress on parallel transformers [96, 97]. The GIC splits between the diverter and the transformer. Although the authors are unaware of any implementation, DC-diverters are considered to be extremely expensive.

### 2.5.4 DC Compensated Transformers

Direct current compensation (DCC) systems in transformers mitigate the effect of LFCs with a counteracting current through an additional winding. This compensation current flowing through the extra winding creates a direct flux with opposite sign of the LFC flux. For this purpose, a field sensor measures the flux in the transformer core, which is used as an input for a controller, which calculates the needed counter flux and respective current, which is then fed into the compensation winding [98]. This mitigates/cancels the direct flux in the core and therefore the half-cycle saturation effects. The LFC still flows through the transformer and only the effect is canceled. A principle scheme of the DCC is shown in Figure 10.

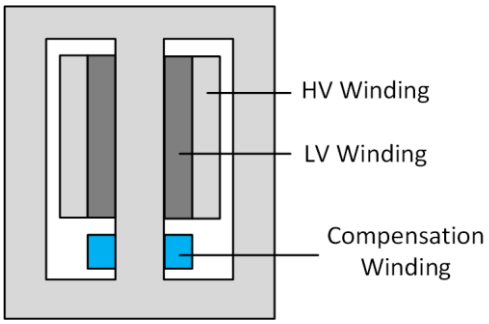


*Figure 10: Direct current compensation schematic*

As this method needs an additional winding on the transformer core, only newly built transformers can be equipped with DCCs. There are now several DCC generations in operation, some with an external current limiting reactor, as shown in [98], and others with power electronic added to the transformer cabinet.

There are several transformers with DCC in the Austrian power grid in operation. One of these transformers is also equipped with a neutral point measurement system with an additional DCC measurement, see section 3.2.2.

### 2.5.5 Neutral Point-connected Devices

The most popular mitigation strategy is to add additional assets to neutral points to block high LFCs. Devices that block the DC-behavior of GICs during solar storms include capacitors [32, 99–101], for example, in which the blocking element is bypassed with switches during normal operation when no neutral currents are present. These devices are standardized in [102].

Neutral point resistors raise the resistance for GICs and therefore lower the magnitude of neutral point currents. These resistors can be fixed [91, 99, 100], variable [95, 103, 104], or even variable with a centralized optimized controller [105].

A counteracting voltage in the neutral point is created by converter-based devices, such as a buck-boost converter, in more recent developments [106]. These gadgets can also be used to operate in grid-supporting mode in times with low solar activity, e.g., voltage regulation or voltage unbalance. Additionally, methods for pairing of harmonic suppression systems with DC blocking devices are under research [107]. The use of fast semiconductor switches in neutral points is another strategy for power electronics. By rapidly on and off switching of the neutral point connection, this device with switching frequencies of 1.2 kHz proposes a reduction in the GIC influence on transformers while maintaining the same short-circuit behavior with very fast bypass switching [108].

There are optimization algorithms available, that propose an optimal placement of mitigation devices [109–112].

All of these neutral blocking devices require careful placement and may cause additional disturbances during normal operation of the grid [113].

### 2.5.6 Corrective Switching

[114–116] pursue the strategy of switching lines in order to change the connections between substations and reduce GIC impacts. While [114] optimizes the grid connections to reduce the transformer reactive power loss, [115] models the AC load flow with additional transformer reactive power losses and reduces the costs of load shedding and generation dispatch required after a corrective line switching. Shutting down lines to reduce the effects of solar storms might not always be possible, though, due to grid operation, high load flows, or n-1 security. Therefore, additional mitigation devices may be needed to effectively reduce the LFC impact.

## 2.6 LFC Measurements

The measurement of LFCs is possible in various ways. The three main methods as well as a selection of measurements worldwide are presented in this chapter.

### 2.6.1 LFC Measurement Methods

#### 2.6.1.1 Neutral Point Measurements

As LFCs and especially GICs enter the high voltage grid through grounded transformer neutral points, this is the most common place to measure these currents. For this purpose, a current transducer, capable of transferring DC, is installed in the connection of the transformer neutral point and the substation grounding system. There are different transducer technologies in use, e.g. hall effect transducers [5, 117–119], clamp meters [120] or Hall sensors which are directly mounted on e.g., an earthing switch.

#### 2.6.1.2 Line Measurements

Another way of LFC determination in high voltage grids is the differential magnetometer method (DMM). This method uses two magnetometers, one placed directly under a high-voltage line and another one placed at some distance. The magnetometer under the line measures the magnetic field from the power line and determines the DC field. The second one is used as a reference magnetometer to subtract the earth's magnetic field from the line measurement. These kinds of measurements were performed in Namibia and South Africa for a limited amount of time [121]. As there was no neutral point measurement system in operation, the system's accuracy was not assessed. An important aspect of the measurements in [121] is that the magnetometers were placed under a single three-phase power line. Another measurement campaign done by [122] in the UK showed large differences between DMM and neutral point measurements. Measurements with DMM in Spain also revealed, that the method is highly susceptible to interferences and does not lead to satisfying results [123].

#### 2.6.1.3 Phasor Measurement Data

The usage of phasor measurement unit data to identify geomagnetic disturbances is based on the additional reactive power demand of transformers with DC bias. In [124], PMU Data is analyzed for two GMDs in the Chinese power grid. As there are no neutral point measurements available for the investigated grid, the measurements were only compared to GIC simulations, which, however, were not validated with measurements. As the reactive power of course varies in dependence on load currents, the transformer excitation current was calculated as the difference between high- and low-voltage side currents. The correlations vary and may not lead to satisfying results. However, it is clearly stated, that GMDs have an impact on reactive power demand and an indication of GIC impact is given.

### 2.6.2 LFC Measurements Worldwide

**North America:** Neutral point measurements in Canada and the US are done by transmission system operators, however, the measurement locations and data are not open to public. Despite this, DMM measurements were performed in Alberta, Canada by [125], which also had access to neutral point measurement data. Unfortunately, the magnitudes of the DMM measurements and the neutral point measurements differ a lot. New regulations in the US also demand a GMD action plan and GIC measurements by TSOs [126].

**Germany:** There is no continuous neutral point measurement network in Germany. However, there were temporary measurements performed with a closed-loop hall-effect sensor [117].

**Finland:** The first DC monitoring in Finland was set up in 1977 but was decommissioned again. In 2021, the installation of new neutral point measurement systems was started.

**Sweden**: In Sweden, a single transmission line was used for temporary GIC measurements: For this purpose, the line was disconnected from the grid and grounded via shunt reactors on both sides [8].

**Great Britain:** There are four permanent GIC neutral point measurements with hall-probe sensors installed in the Scottish power transmission grid [127]. Additionally, measurements with differential magnetometers (DMM) were performed by [122] under lines near neutral point measurements. The time course of the two different measurement techniques correlate well, however, some of the DMM amplitudes differ from neutral point measurements.

**Ireland**: Modelling of GICs in Ireland was done by [82, 128]. There is detailed information about grounding resistances and earth layers available; nevertheless, only one transformer is equipped with a neutral point measurement system, which can be used for model verification.

**Spain:** GIC measurements in Spain were done by neutral point measurement [85] with a hall-effect transducer and with DMM measurements below transmission lines [123]. The temporary DMM measurements were used to validate GIC calculations, nontheless, the solar activity was quite low and electromagnetic disturbances were identified as a serious problem.

**Russia:** In Russia, GIC measurements started in 2011 in the area of Karelia and Kola peninsula and are based on neutral point measurement. Between 2011 and 2018, more than 30 GIC events were registered and amplitudes of 40 A occurred. [129]

**South Korea**: To gain knowledge and protect the South Korean transmission grid from GICs, the first measurement system was installed in a transformer neutral with a rated voltage of 765 kV in 2012. Two additional measurement devices were installed in 345 kV transformer neutrals in 2014. The used current clamp in the transformer neutral is connected to a DAQ system, which transfers the data via Ethernet to a computer in the substation control room. During the measurement period between 2012 and 2015, maximum currents of +- 7A were measured. [130]

**Japan:** Measurements in Japan started at two 500 kV transformers in 2017 and expanded to another one in 2018. [120] describes different neutral point measurement systems, the chosen current transducers and analyzes recent measured geomagnetic activities during solar cycle 24.

**Australia**: GIC measurements in Australia started in 2012 as a cooperation between universities, energy market operator, meteorological service, transmission system operator and other partners. The location of the measurement devices was selected after primary calculations. The hall-effect current transducers are mounted on the transformer neutral connection and are directly connected to the Australian SCADA system [118]. The analysis and comparison between measured and calculated GICs in Australia in [83] show amplitudes of up to 18 A during some minor storm in October 2013. The number of measurement systems was increased to ten in Australia and Tasmania [83].

**New Zealand**: New Zealand has had ongoing neutral point measurements since 2001. The reason is the investigation of earth-return stray currents of the HVDC link between the two islands. It started with 13 substations and 36 transformers in 2001 and was extended to 22 substations and 60 transformers in 2018 [131]. A solar storm on 2 October 2013 led to 50 A in a measured transformer, which is a comparatively high value for a non-extreme space weather event [132]. In addition to neutral point measurements, there is a large number of harmonic distortion monitors. The combination of both datasets in [131] for a solar storm in 2017 shows the even total harmonic distortion caused by saturated transformers and suggests the usage of power quality analysis for GIC detection.

**Namibia**: Measurements in the Namibian Transmission grid were performed with hall effect current clamps in two substations [133]. Additionally, temporary DMM measurements were performed [121].

# 3 Measurement of LFCs in the Austrian power grid

This section is focused on the LFC measurements in Austria. At the beginning, possible measurements on transmission line are discussed. This includes the description of an optical measurement system under development as well as an overview of DMM measurements from project partners.

The bulk of this chapter deals with measurements of transformer neutral point currents and compensation currents. Therefore, the two different measurement system types are outlined and the measurement locations of the nine systems are described.

To conclude this chapter, measurements of a geomagnetic inactive day as well as from a GMD in April 2023 are shown and described.

## 3.1 Line Measurements

The measurement of small LFC in presence of high AC currents is difficult, especially on high voltage potential. Standard current transducers in power grids cannot measure DC currents, as no induction takes place. A promising method for measuring LFCs on high voltage potential is based on the Faraday effect [134], which is based on the influence of magnetic fields on the polarization angle of light. Such non-conventional current transformers are already available, but not with the necessary accuracy and resolution to measure small quasi-direct currents. The Faraday effect, shown in equation (55), describes the influence of a magnetic field on the polarization angle of light in a dielectric medium.

$$\theta = \nu\mu \int_0^L \vec{H} d\vec{l} \tag{55}$$

The rotation angle θ depends on the Verdet constant ν, which is a material property of the optical fiber, the magnetic permeability μ, and the integrated magnetic field H over the length L. By assuming $\mu = 1$ and the fiber to be a closed loop around a conductor with the current $I$, equation (55) can be simplified to (56).

$$\theta = \nu N I \tag{56}$$

This means with a fixed number of turns N around the conductor, the change of the rotation angle θ is proportional to the current I. The measurement method is less sensitive to grid faults since no magnetic core is required that could saturate at high fault currents. This means that the measurement method if designed properly, can provide reliable measurement data even during a fault in the power grid and ensure safe grid operation. Depending on the sample rate and resolution, also transient measurements are conceivable. As the optical fibers are not conductive, the optical measurement approach enables measurements on lines or transformer bushings without transducers and will be the first possibility to investigate the symmetry of GICs.

As part of the project FORESEEN, a prototype of the proposed measurement systems is designed and built and will be tested in field under real conditions [135, 136]. The author of this thesis was actively participating in this project.

DMM measurements, as described in section 2.6.1.2, were also tested by GeoSphere Austria in the Austrian transmission grid. The first results look promising, however, the temporary measurement was influenced by various disturbances. Nevertheless, more DMM measurements in Austria are planned.

## 3.2 Transformer Measurements

### 3.2.1 Neutral point measurements

Transformer neutral points are the connection between high voltage lines and ground and are therefore the entry point for LFCs. Neutral point grounding strategies in 220- and 380-kV networks have two central points of view. On the one hand, TSOs have to ensure that currents in case of line-to-ground faults are high enough to trigger protection relays (minimum fault current criterion). On the other hand, step and touch voltages caused by fault currents must not exceed values limited by standards [137] (maximum fault current criterion). To achieve these goals in the analyzed transmission grid, basically in every substation one neutral point per voltage level is grounded. Short circuit simulations are carried out to prove that the earth fault currents are within the desired limits.

At the time of writing, there are nine transformer neutral point measurements in operation in the Austrian power grid, measuring currents of nine transformers numbered NP01 to NP09 in eight substations, shown in Figure 11. The measurement system was developed and set up under the participation of the author of this thesis. The eastern and northern part of the grid is situated in a more or less flat area. NP01 and NP04 are situated in the same substation, close to the capital Vienna, which results in special effects, which are in more detail in section 4. At NP07, an active LFC compensation device is installed. Besides the neutral point current, the corresponding measurement device also monitors the operation of this device.

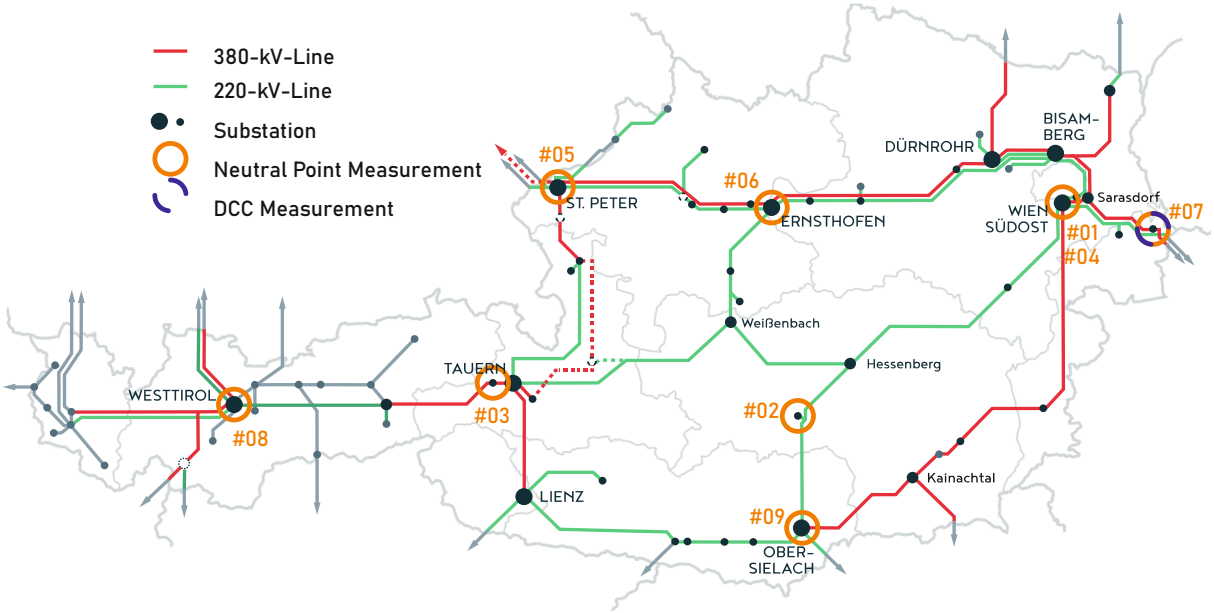


*Figure 11: Neutral point measurement systems in Austria*

TABLE 2 shows information about the transformer type and voltage level, measurement start time, and system type. The direction depicts the sign of the measured current: GND->Grid means a positive sign for currents flowing from the substation grounding system through the transformer into the grid and a negative sign vice versa. With this high number of measurement systems, it was possible to install at least one system for every transformer type operating in Austria, i.e. three-phase, transformer banks and autotransformers. The continuous long-term measurements and the number of devices are unique in Europe.

Additionally, there have been temporary measurements for a limited amount of time, which are not included in this table but will be introduced and discussed in other chapters.

*TABLE 2: Information about neutral point measurements, transformer types and starting time*

| MEASUREMENT NUMBER | TRANSFORMER TYPE | VOLTAGE LEVEL | MEASUREMENT STARTED | SYSTEM TYPE | DIRECTION |
|---|---|---|---|---|---|
| **NP01** | 3-phase | 380 kV | 08.2016 | Bypass | GND->Grid |
| **NP02** | 3-phase | 220 kV | 04.2018 | Bypass | Grid -> GND |
| **NP03** | 3-phase | 380 kV | 04.2017 | Bypass | Grid -> GND |
| **NP04** | 3-phase | 220 kV | 05.2017 | Bypass | GND->Grid |
| **NP05** | 3x 1-phase | 380 kV | 10.2017 | Bypass | Grid -> GND |
| **NP06** | 3-phase | 220 kV | 10.2021 | Bypass | GND->Grid |
| **NP07** | 3-phase | 380 kV | 01.2020 | Bypass | Grid -> GND |
| **NP08** | Autotransformer | 380 kV | 03.2021 | Bypass | Grid -> GND |
| **NP09** | 3-phase | 220 kV | 12.2021 | Mounted | Grid -> GND |

There are two different measurement system types in use which either bypass the grounding switch or are mounted on it.

Figure 12 a) and b) show the Bypass-type. During normal operation the neutral point (1) is connected via an earthing switch (2) to ground. When installing the measurement system, the earthing switch is opened, a mobile earthing equipment (3) is connected to the neutral point (1), fed through the measurement cabinet (4) and the current transducer (5) and connected to ground. The current transducer must be able to measure DC. There are several options for transducers, e.g., DC clamp meters or zero-flux transducers. The used zero-flux transducer measures DC by canceling a remaining direct flux in the core with a counteracting current. This current, produced in a secondary electric circuit is proportional to the current in the conductor. The measured current from the transducer (5) is forwarded to a simple data acquisition system DAQ (6). The DAQ consists of a power supply, active low pass filter, A/D conversion and single board computer. The additional input channels (7) are for DCC measurements, see section 3.2.2, and (8) depicts the AC power supply and fault circuit breaker.

As the analyzed neutral point currents have very small frequencies, a sample rate of 1 Hz is enough. Because of this sample rate, the use of a simple Raspberry Pi is possible. The data is sent live via GSM to a server for further analysis. A more detailed description of the measurement system can be found in [138].

a)


b)

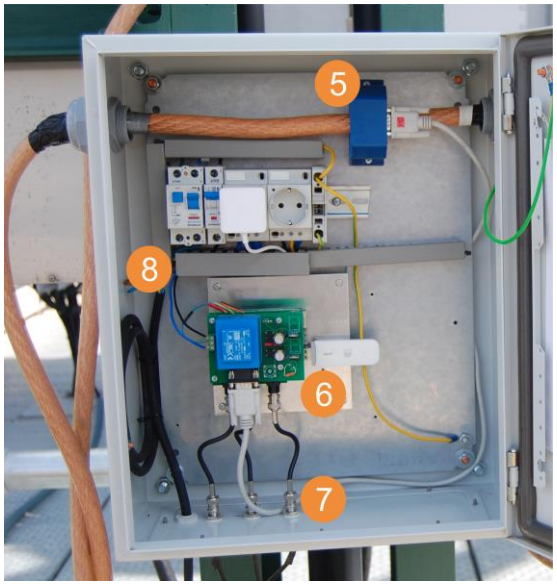


*Figure 12: Neutral point measurement system- Bypass Type*

Although this system is very easy to install in already existing substations with installation times of only a few hours, this type has one main disadvantage: the neural point cannot be disconnected remotely from the control room anymore. Especially in remote substations without on-site staff, this means restrictions in the operation of the power grid. This restriction is removed with the second type of the measurement system, where the current transducer is mounted on the earthing switch, as shown in Figure 13.

*Figure 13: Neutral point measurement system - Mounted type*

The used split-core transducer uses hall-effect sensors and therefore has a higher temperature drift. This is

compensated in the software by a compensation function that was developed during tests in a climate chamber. In operation, the temperature near the CT is measured. The temperature dependence is removed in the post-processing. To prevent possible long-term drifts, which may occur because of the Hall sensors, offset calibrations are performed on a regular basis during the first years of operation. For this purpose, the earthing switch is opened, and the offset is stored and corrected in the post-processing. Detailed information on the measurement device, the electronic setup, different versions etc. can be found in [138].

Both measurement types have a range of ± 25 A, which was suitable for the geomagnetic quiet time in a mid-latitude country.

### 3.2.2 Compensation Current Measurement

Transformer NP07, among others in the Austrian transmission grid, is equipped with a direct current compensation system (DCC) from Siemens Energy. The DCC produces a DC flux, which compensates the DC flux resulting from LFCs. For this purpose, a fourth winding is added on each of the three transformer legs. With these additional windings, a counter-flux proportional to the disturbing DC flux can be introduced. This does not cancel the neutral point current itself, but the resulting flux and therefore the effect on the transformer.

To measure the compensating currents $I_{DCC,x}$, three current transducers are placed at the fourth winding infeeds. With the winding ratio between transformer HV side $n_{HV}$ and DCC $n_{DCC}$, the DC in each phase $I_{DC,x}$ can be calculated according to (57). As this ratio depends on the number of high-voltage windings, the tap changer position influences these results and must therefore be considered. The three currents are not completely symmetrical, therefore this must be done for all three phases. The sum of the three-phase currents equals the neutral point current $I_{NP,DCC}$, which is equivalent to the measured neutral point $I_{NP}$.

$$I_{DC,x} = \frac{n_{DCC}}{n_{HV}} I_{DCC,x} \; \forall \; x \in [A, B, C] \tag{57}$$

$$I_{NP,DCC} = I_{DC,A} + I_{DC,B} + I_{DC,C} \tag{58}$$

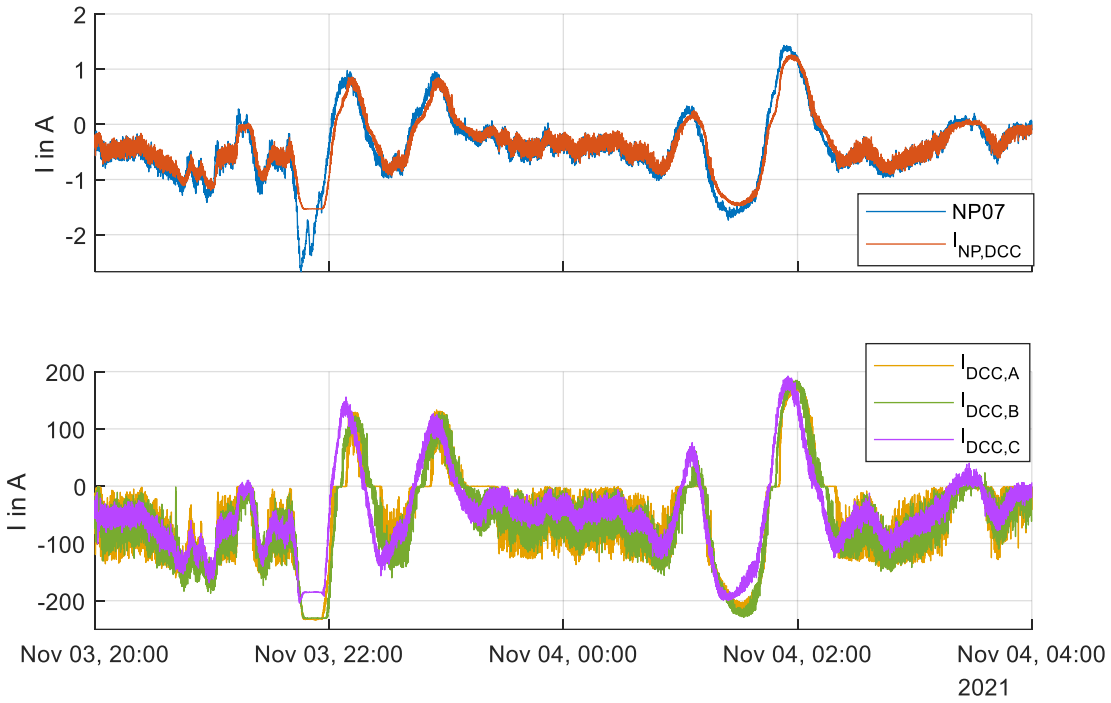


*Figure 14: Neutral point current comparison and DCC: blue: measured neutral current, red: calculated neutral current from DCC measurements, yellow, green, violet: measured DCC currents*

Figure 14 shows measurements during a solar disturbance from November 2021. The upper plot shows the comparison between the measured neutral point current and the current, calculated out of the compensation currents with (58). There is a slight difference between these currents, which results from the measurement tolerance of the compensation currents, the compensation capability, damping in the phase currents and the principal control of the compensation currents. In the lower plot, the three measured compensating currents are shown. It can be seen, that they are very similar in their time courses and amplitudes. There are different versions of DCCs with different ratings in operation in the Austrian power grid. The one equipped with the measurement is limited to 200 A per phase, which is capable of compensating a neutral current of approximately 1.5 A, depending on the tap changer position. If the neutral point current is too high, the DCC operates at its maximum power, as happened on November 3, 2021, at 21:50.

The DCC measurement also shows a steady infeed in the compensation windings, which means that the neutral point measurement does not have an offset, but there is a steady neutral current flowing through this transformer.

## 3.3 Measurements on an Average Day

March 14, 2023, was a typical day with low solar activity. The magnetic field measurements at Conrad Observatory, depicted in the upper plot of Figure 15, show the slow daily change, which is caused by the earth's rotation. The Kp values [15] for this day are between 0 and 1+, which marks a weak activity.

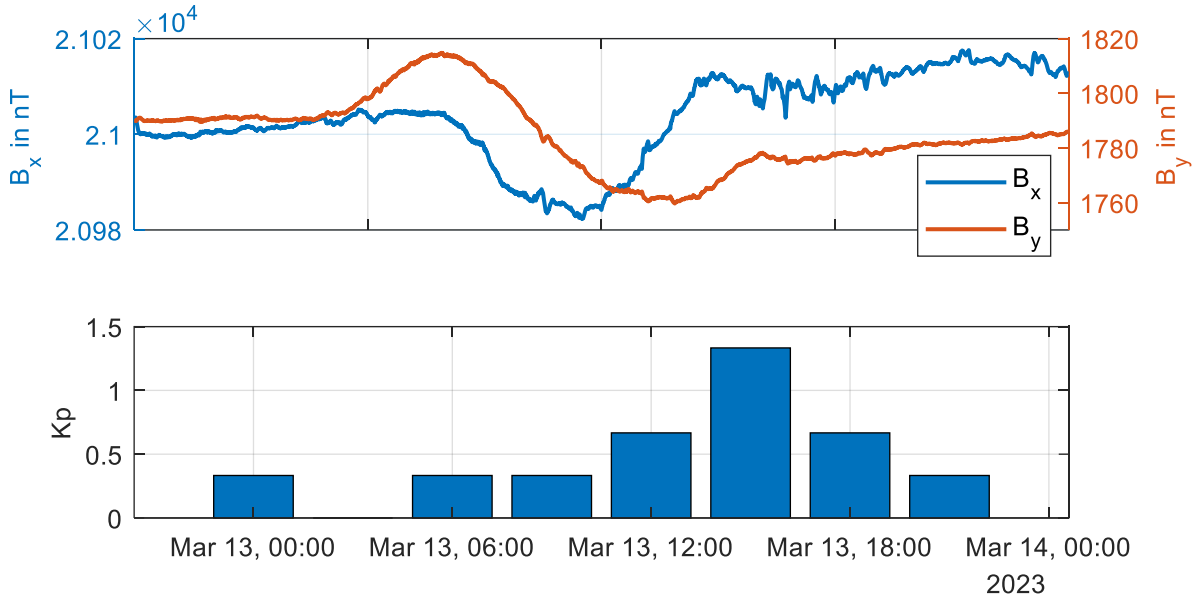


*Figure 15: Magnetic field and Kp values for a day with low solar activity*

The nine neutral point measurements for this day, depicted in Figure 16, show only small amplitudes. In the morning hours, the noise in NP01, NP04 and NP06 rises whereas NP07 has in general higher noise levels throughout the day. The reason for this background noise is discussed in section 4.

The slow change of the magnetic field, which takes several hours, is visible in some neutral points, e.g., NP01 and NP07. Additionally, a constant offset can be seen in almost all measurement points. This is not a measurement error but a very slow, nearly constant current flowing through the neutrals. This can also be seen in Figure 17, where the neutral point current and the DCC measurements of NP07 are depicted. The DCC is in continuous operation to compensate the nearly constant neutral current of 0.5 A.

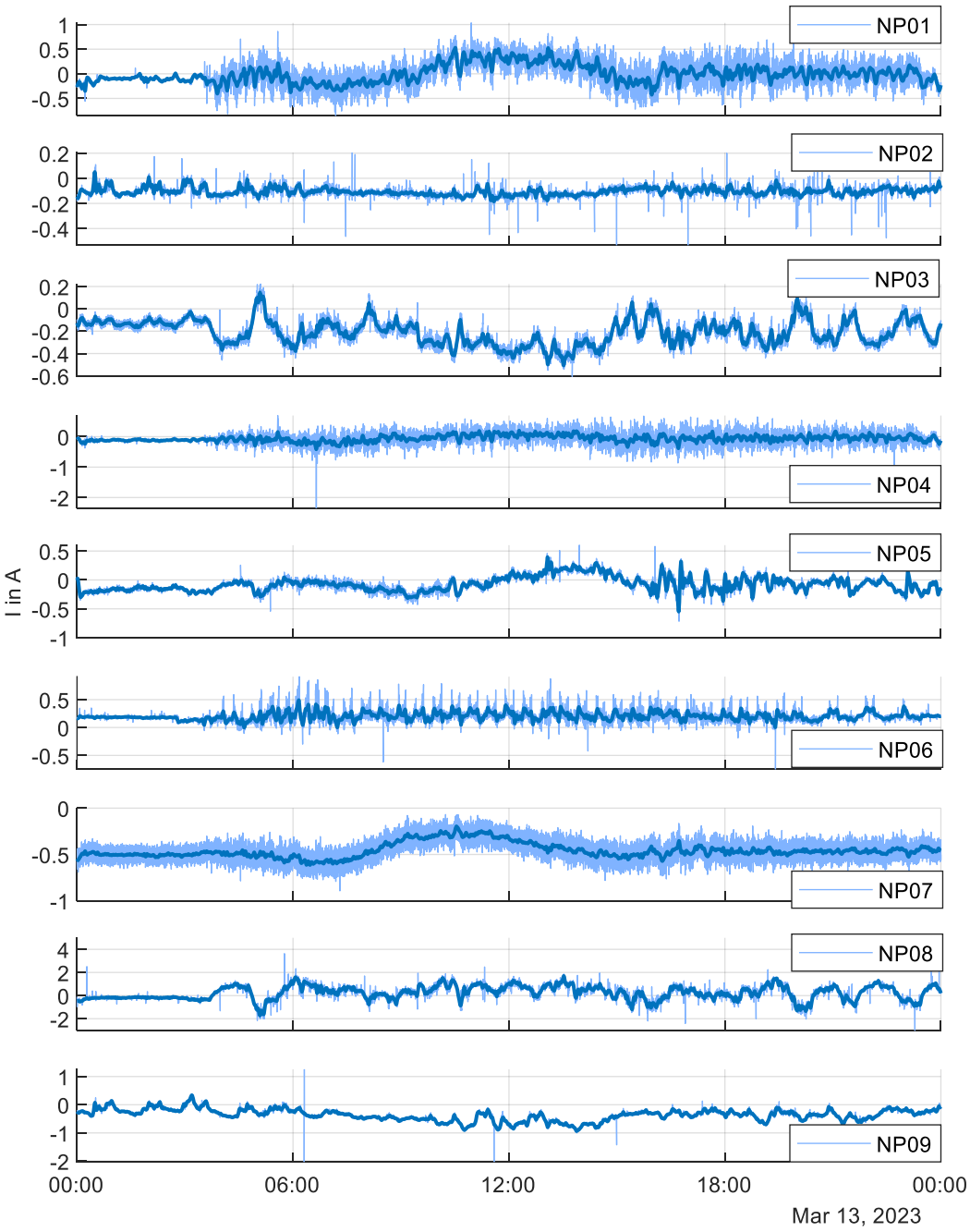


*Figure 16: Neutral point measurements for a day with low solar activity*

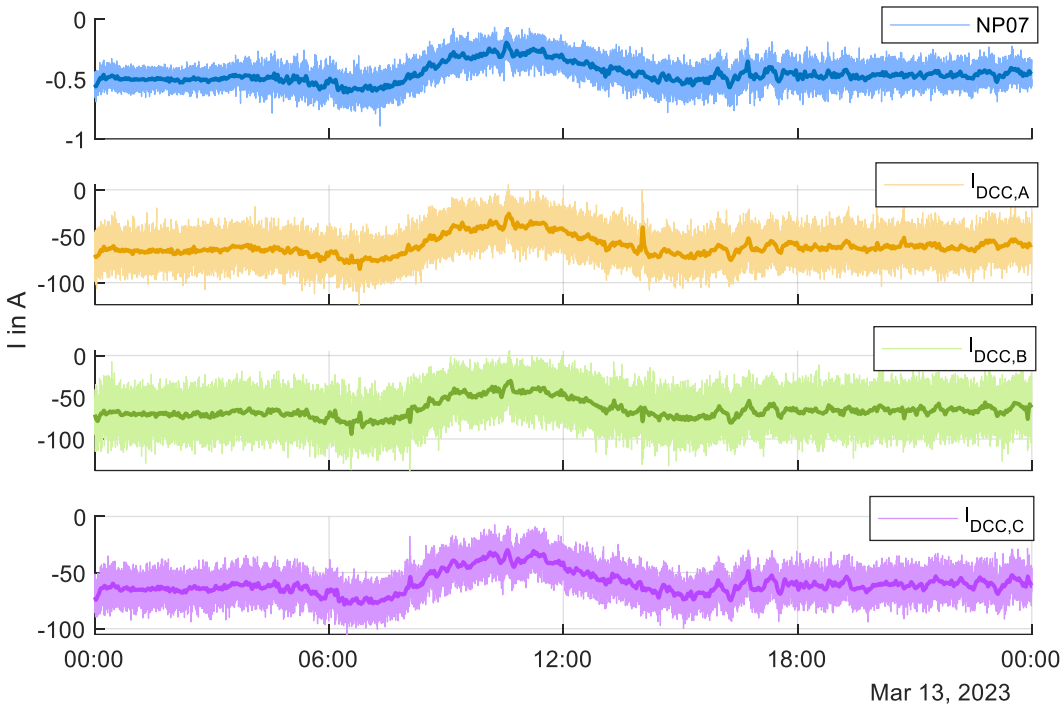


*Figure 17: NP07 and DCC measurements for a day with low solar activity*

The DCC currents in Figure 17 also show a slight asymmetry, which contradicts the generally assumed symmetrical distribution of LFCs. Therefore, measurements on high voltage potential, as proposed earlier, are of high interest.

## 3.4 The GMD of April 23-24, 2023

One of the highest GMDs in recent years occurred on 23-24 April 2023. As depicted in Figure 18, Kp values of up to 8+ were measured during this very active period. As the magnetic field measurement in Figure 19 shows, the GMD had several phases. The first rapid change in the magnetic field started at 17:35 followed by the first main disturbance between 19:00 and 22:00 (in the following described with phase 1) and a second major disturbance between 3:30 and 6:00 on the next day (described as phase 2).

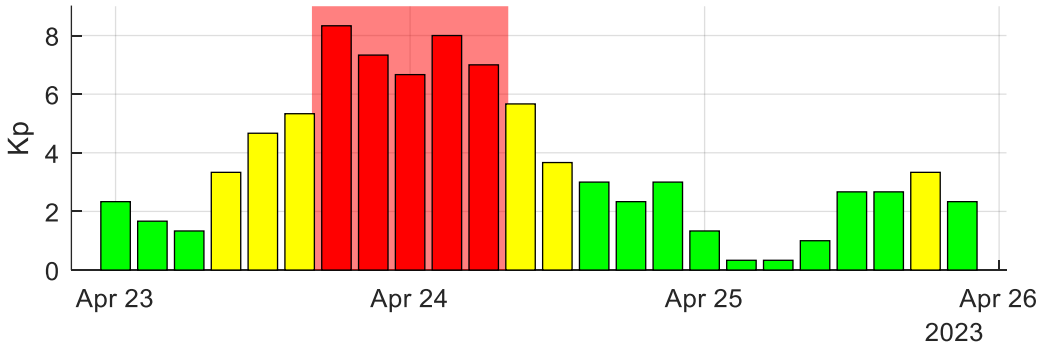


*Figure 18: Kp values for a geomagnetic active period in April 2023*

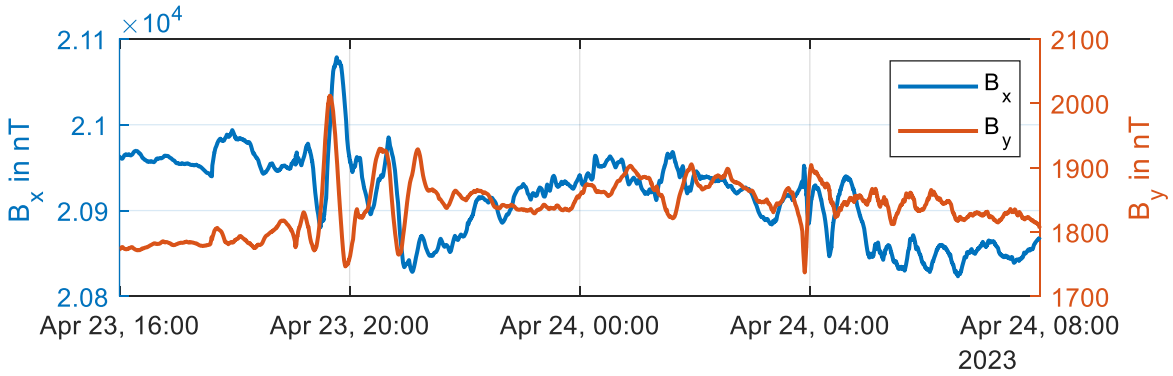


*Figure 19: Magnetic field measurement at Conrad Observatory for the solar storm in April 2023*

During this storm, seven out of nine measurement systems were in operation, the remaining two systems were due to transformer maintenance out of order. The measurements of the systems in operation are shown in Figure 20. The two main phases are clearly visible in all stations. The principal time course is similar in all neutral points, however, the amplitudes differ. By comparing the magnetic field and the neutral point currents, the sensitivity of some transformers, which is the direction of the electric field that leads to high currents and will be calculated in section 5.3.1, is already visible. For example the fast drop of $B_x$ just after 04:00 leads especially in NP05 to significant currents. As a change in $B_x$ leads to an electric field $E_y$, this means NP05 is very sensitive to electric fields in east-west (west-east) direction.

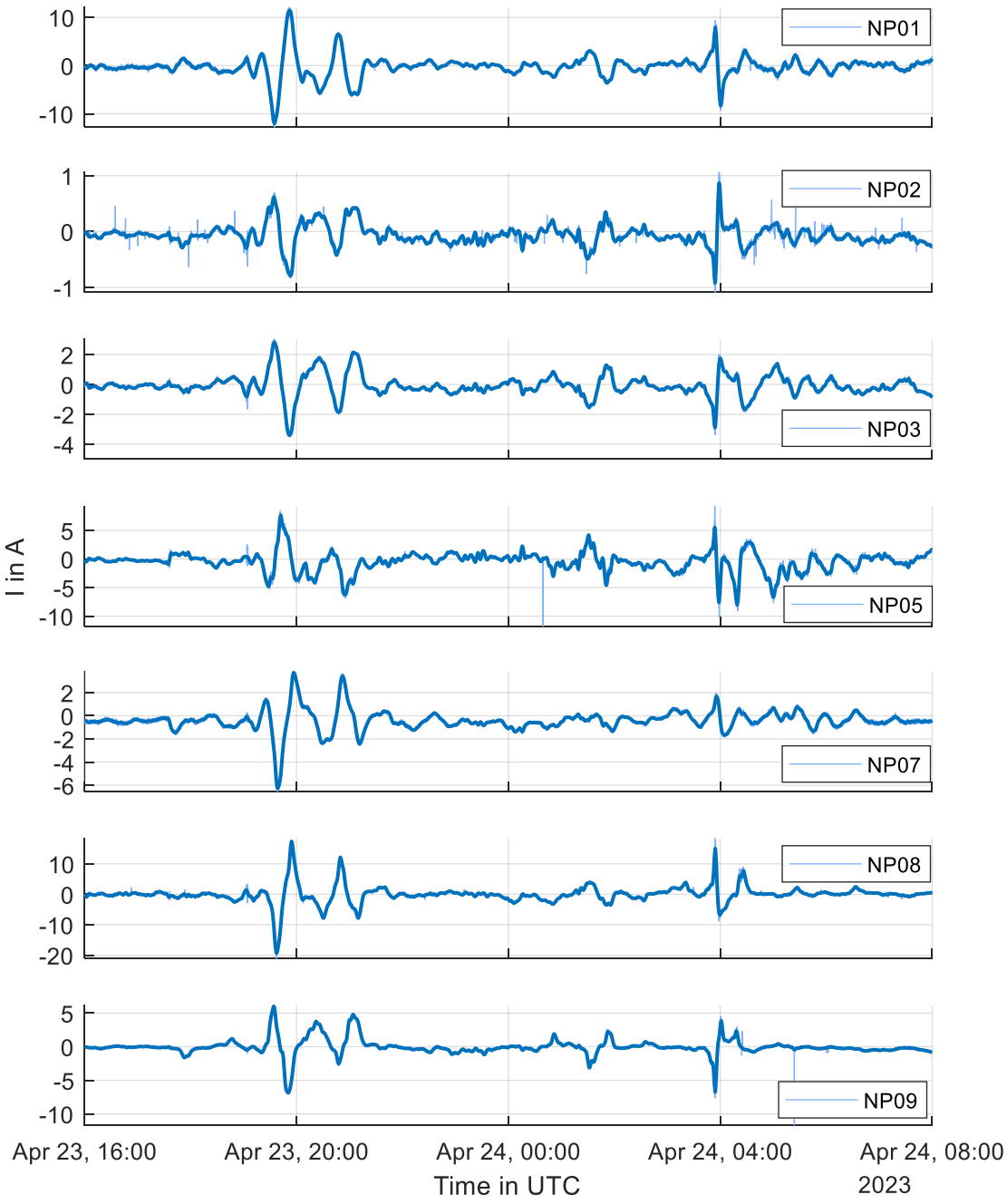


*Figure 20: Neutral point measurements during the storm of April 2023*

NP08 recorded the highest ever measured neutral point currents of -20.9 A in Austria so far. TABLE 3 summarizes the minimum and maximum currents for the two phases, the time between the positive and negative peaks and the mean gradient between the peaks.

As shown in Figure 19 and Figure 20, the two phases of the GMD are quite different in terms of slope and duration. The gradients in phase two are, except for NP07, higher for all measurements, which is reasonable for faster change of the magnetic field. The time between the extrema is nearly the same for all measurements, which can be led back to the relatively small size of Austria, which means no large differences in the magnetic field between the eastern and western parts of the grid occur.

*TABLE 3: Parameters of the two storm phases for the measurement systems in operation*

| **NEUTRAL POINT #** | **PHASE 1 23.04.2023 19:00 – 22-00 UTC** | | | | **PHASE 2 24.04.2023 3:30 – 6:00 UTC** | | | |
|---|---|---|---|---|---|---|---|---|
| | Max I | Min I | Time between extrema | Current gradient between max and min of storm | Max I | Min I | Time between extrema | Current gradient between max and min of storm |
| | A | A | min | A/min | A | A | min | A/min |
| **NP01** | 12.1 | -12.6 | 17 | 1.45 | 9.4 | -9.2 | 6 | 3.1 |
| **NP02** | 0.7 | -0.8 | 19.5 | 0.07 | 1.1 | -1.1 | 4 | 0.55 |
| **NP03** | 3 | -3.5 | 18 | 0.36 | 2 | -3.4 | 5 | 1.08 |
| **NP05** | 8.4 | -5.2 | 12 | 1.13 | 9.2 | -10.1 | 5 | 3.86 |
| **NP07** | 3.8 | -6.5 | 18 | 0.57 | 1.9 | -1.8 | 8 | 0.46 |
| **NP08** | 17.8 | -20.9 | 17 | 2.28 | 18 | -8.7 | 4 | 2.33 |
| **NP09** | 6.1 | -7.1 | 17 | 0.78 | 4.5 | -7.6 | 6 | 2.02 |

The magnitudes of the measurement points vary, of course, in a wide range. This has several reasons including the voltage level of the transformer, the earth structure below, the direction and number of connected lines, etc.

Although this was the highest-ever recorded GMD in Austria, no problems in operation of the transmission grid were reported or noticed.

## 3.5 Summary of LFC Measurements in Austria

LFC measurements in the Austrian Power Grid started in 2014 with temporary measurements. Since then, a continuous measurement network was implemented with, at the time of writing, nine measurement systems in eight different substations in operation. Eight of these neutral point measurement systems bypass the transformer earthing switch with mobile earthing equipment, which is afterward fed through a zero-flux current transducer. System NP07 is additionally equipped with a compensation current measurement. This DCC measurement shows activity also during geomagnetic inactive times, which means that other sources lead to LFCs which can be compensated. As these systems are designed for a maximum LFC, also saturations and limits can occur, as happened during solar storms. The trajectories of the measured neutral point currents, compensation currents and calculated neutral currents correlate very well.

The ninth system has a current transducer mounted on the earthing switch, which allows remote control of the neutral point connection again. Especially in remote substations without stationed staff, this simplifies the grid operation again.

The long-term measurements provide data of geomagnetic low active times as well as from several solar storms. Especially the times of low activity are used to identify other LFC sources in the following chapter. At the time of writing, the solar storm from April 2023 led to the highest ever recorded GICs in the Austrian transmission grid with -20.9 A in NP08. Fortunately, no disturbances were reported.

The neutral point measurement data is one of the key elements in the validation of GIC simulations. This is shown in sections 5.3 and 5.4.

# 4 Identified Sources of Low Frequency Currents

Parts of this chapter were already published in [43, 139]. The nine transformer neutral point current measurements show very different current waveforms. Not only do the amplitudes differ, which is reasonable due to the different locations, but also the frequency components are different. As described in [5, 43, 139], the LFC sources can be divided into geomagnetic sources, leading to geomagnetically induced currents, and artificial sources, i.e. human infrastructure. The frequency ranges for geomagnetic activity are usually between 0.01 mHz and 1 mHz. Artificial sources usually have frequencies higher than 1 mHz. Our measurement systems samples with 1 Hz, therefore only currents below 0.5 Hz are analyzed.

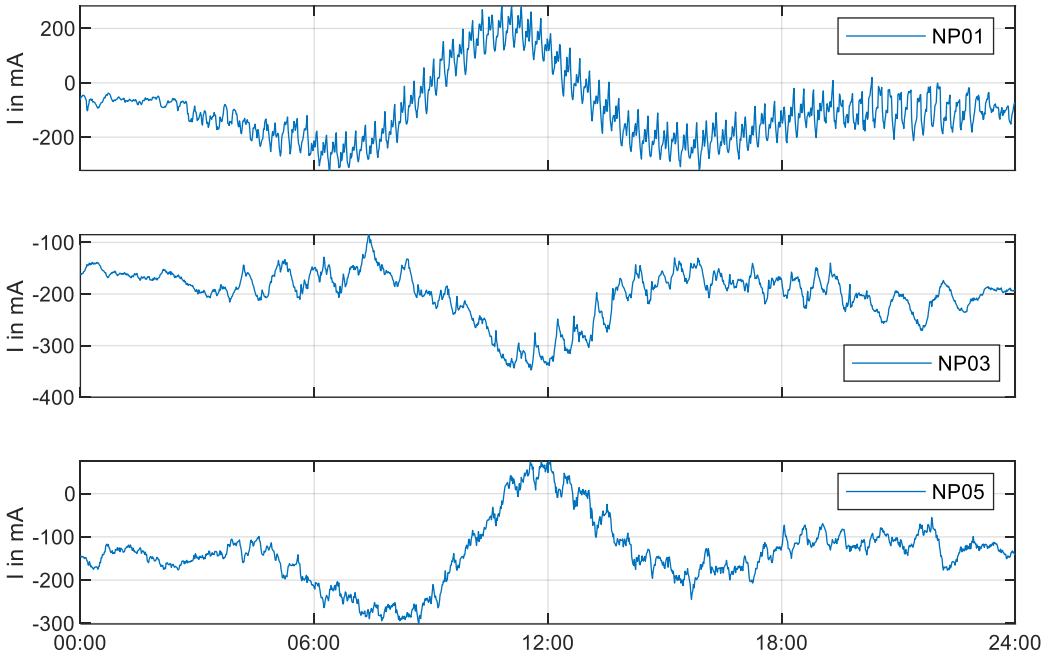


*Figure 21: Daily mean neutral point current for three measurements*

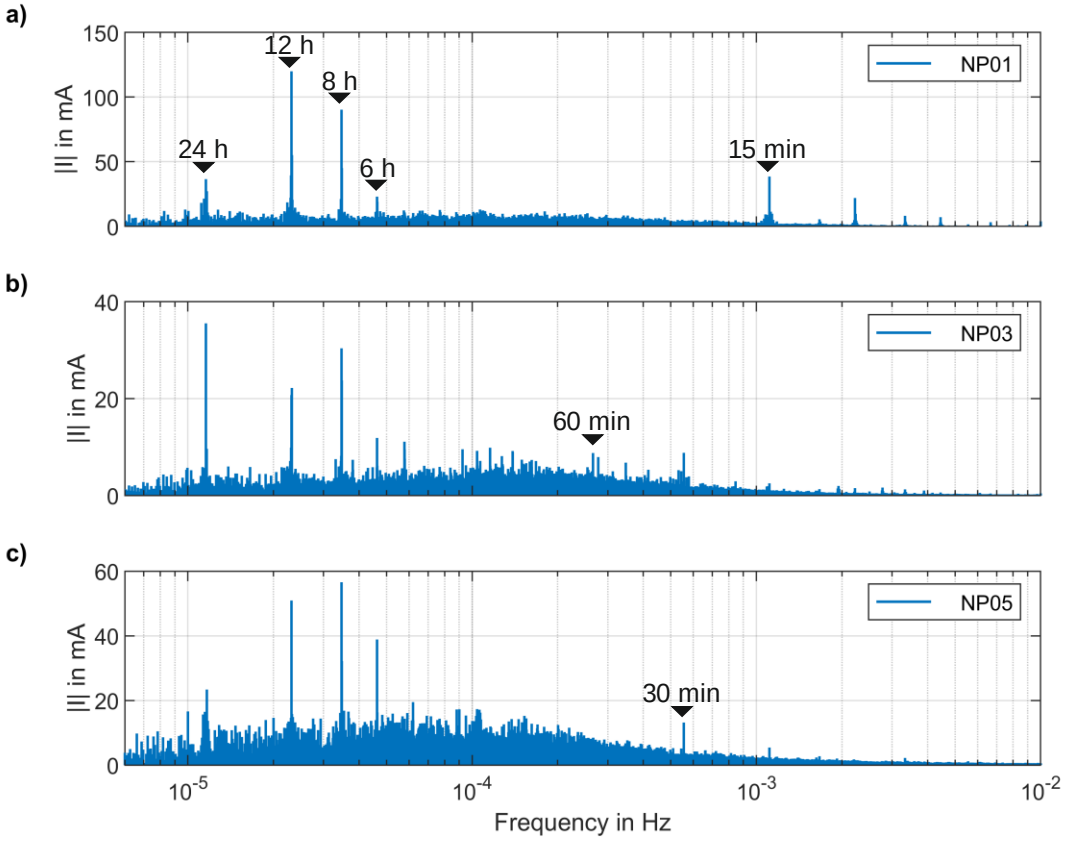


*Figure 22: Frequency spectra of three measurements*

The measured neutral point currents result from different sources, which can be identified through several methods. The measured currents usually have a daily pattern, which consists of a rather slow change and superimposed noise. The slow change results from the Earth's rotation and the related slow change in the magnetic field. This can be seen well by calculating an average daily time course of measurements, i.e. calculating the mean value of a signal for each time step in 24-hour interval for a time series of several days. Equation (59) shows this calculation, where $I_t$ is the mean current vector, $\mathrm{T}$ is the number of days and $\mathrm{t}$ is the time step which is dependent on the signal sample rate $f_s$.

$$I_t = \frac{1}{T}\sum_{d=1}^{T} I_{dt}, \qquad \forall t = 1, \ldots, \frac{1}{fs} \tag{59}$$

In Figure 21, this was done for three measurement sites over a time period of 11 months. The slow change is visible in all three measurements, however, the superimposed noise differs. This is also visible in the frequency spectra of these three mean time series, shown in Figure 22. All three spectra show dominant components with cycles of 24, 12, 8 and 6 hours, which result from the Earth's rotation and are also visible in geomagnetic field measurements [43]. The rest of the spectra show different prominent peaks, e.g. 15-minute cycles for NP01 or 30-minute cycle components for NP05. This leads to the conclusion, that not only a single source leads to neutral point currents, but several that are location-dependent and lead to different frequency components. In this chapter, different neutral point current sources are identified and discussed.

## 4.1 Public Transportation Systems

Public transportation system as a source of LFCs was identified in [5] by analyzing recurring patterns of neutral point measurements and comparing it to the operating hours of the Vienna subway system. The subway system has a DC power supply and is not directly connected to the public supply earthing system.

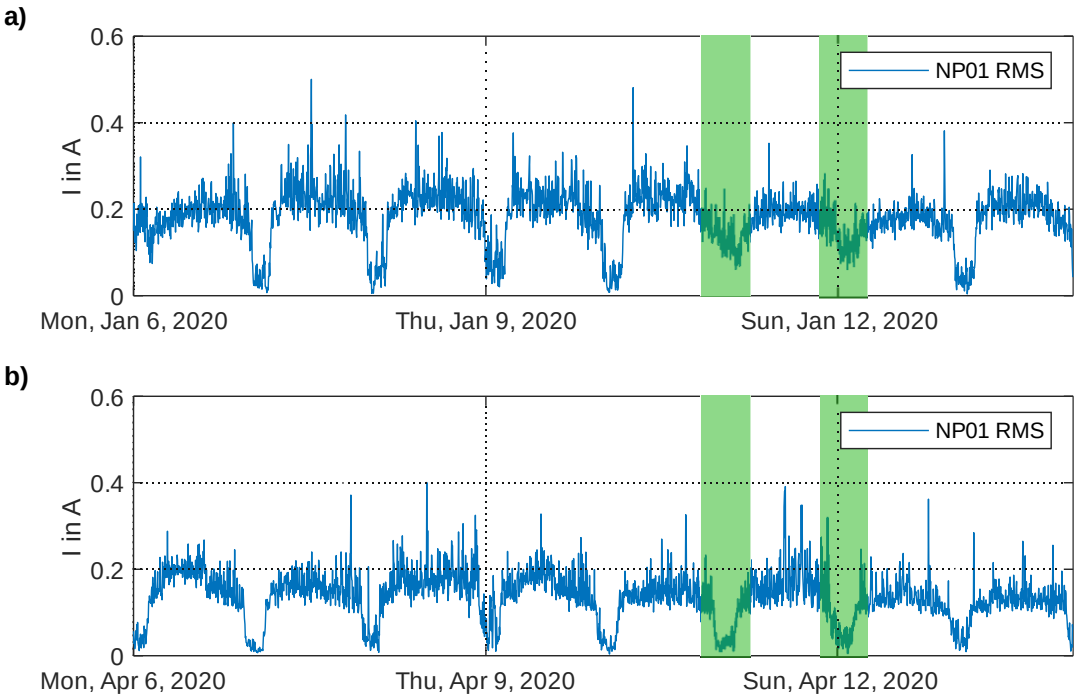


*Figure 23: RMS values for NP01 (weekend nights highlighted in green)*

To see the effect of the public transportation more clearly than in the raw measurement data, the calculation of a 5-minute RMS value is beneficial. Figure 23 a) shows this RMS-time series of a typical week at NP01. The current drops during night, when the subway stops its operation for a few hours from Monday to Thursday. During weekend nights from Friday to Sunday, the subway stays in operation with a reduced number of trains and longer time intervals. Therefore, also the measured currents at the high voltage neutral points do not drop as much as during weekday nights.

In March 2020, Covid-19 restrictions came into force and affected all areas of daily life. Besides numerous effects on the power grid, e.g., reduced loads, the restrictions also led to a change in the operating hours of in public transportation in Vienna. This is shown in Figure 23 b). Not only the overall current decreased, but the currents also dropped during weekend nights, as the subway stopped operation during these nights as well. The effect is clearly visible by comparing the green marked areas in plots a) and b) in Figure 23.

As mentioned, the earthing system of the subway's DC supply and the earthing system of the public supply are not connected directly but with Kirk Cells at specific points. This is done to prevent DC corrosion in public areas as well as because of safety concerns. The Kirk Cells block the DC voltage but shunt dangerous AC voltages to the ground. The locations of the Kirk cells are one of the few places, where both earthing systems are close together and accessible. Therefore, it is possible to measure a voltage between the two earthing systems. This was done for four different locations along one subway line.

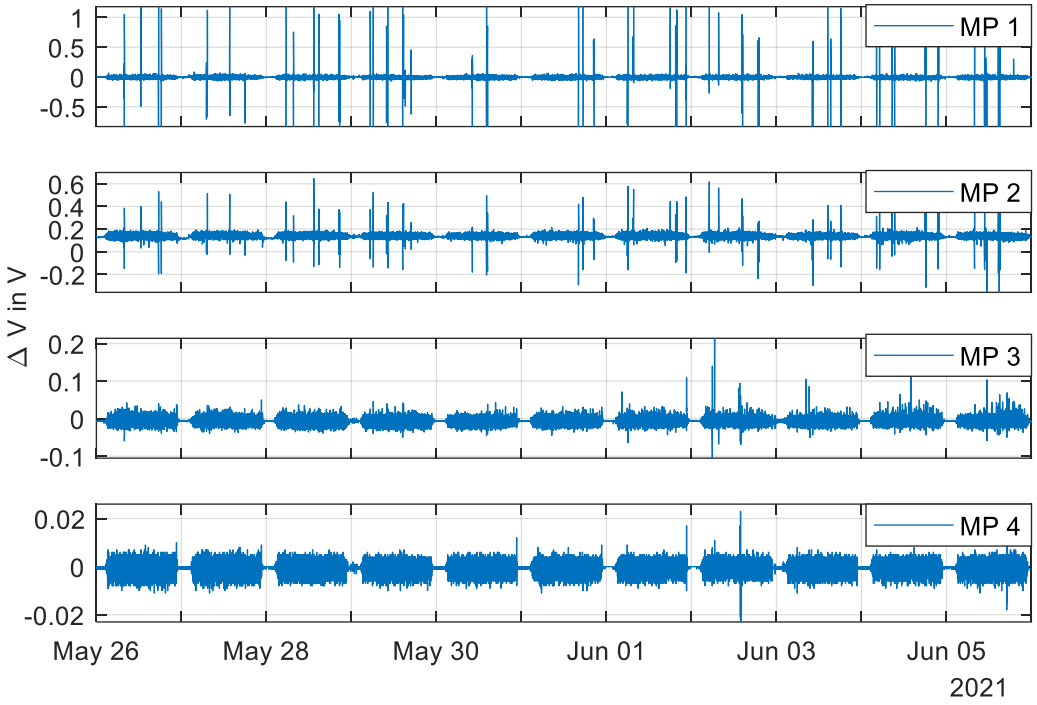


*Figure 24: Four measured voltages between grounding systems*

The measured voltages in Figure 24 have very different amplitudes, depending on the measurement location. This is mostly because of the different resistances between the two grounding systems, which are highly influenced by the age of the building. The older the subway stations, the more likely unwanted connections between the earthing systems are present, caused during the construction of nearby buildings or renovations. However, the daily pattern is similar in all measurement stations. By the time of voltage measurements, the subway still did not operate during weekend nights.

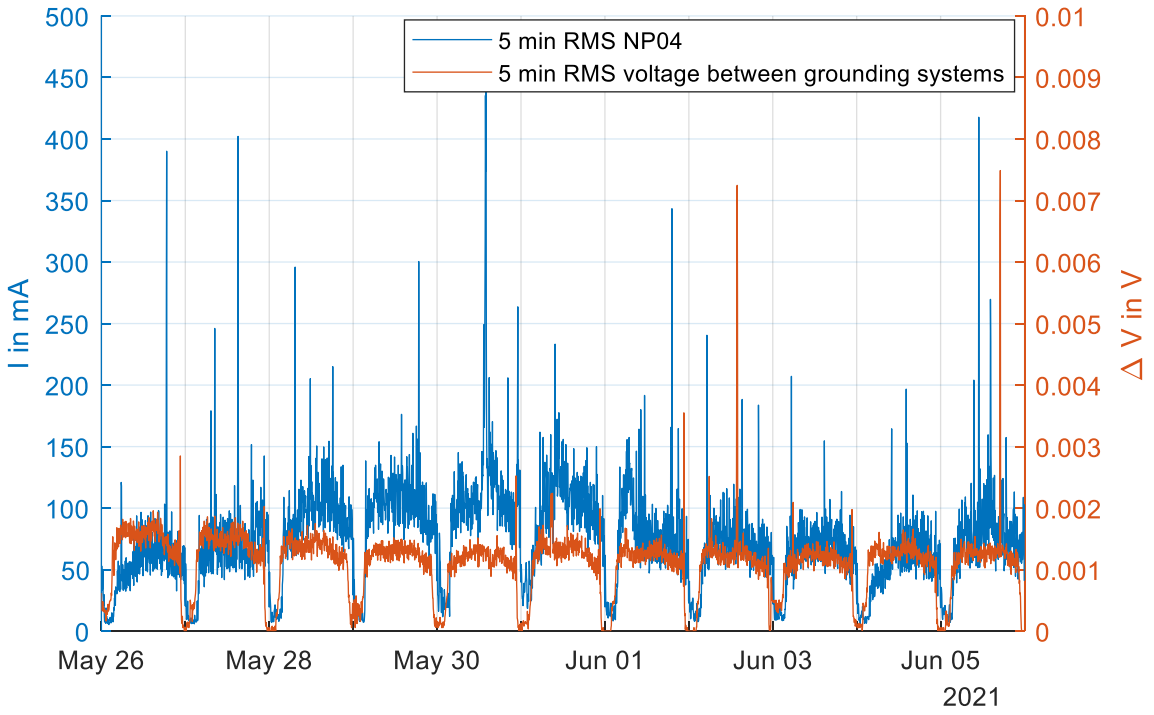


*Figure 25: 5-Minute RMS of NP04 current and a voltage between grounding systems*

Figure 25 shows the 5-minute RMS values of NP04 and one voltage measurement. It can be seen, that the daily pattern occurs in both measurements. Since the voltages are very small, no qualitative statement can be made about the relationship between rising currents and falling voltages over the course of the week. Nevertheless, a correlation is visible, which supports the relation between neutral point currents and public transportation.

## 4.2 Periodically Grid Frequency Deviations

The bulk frequency of 50 Hz in the interconnected transmission grid in Europe shows peaks and dips every ¼, ½, ¾ and full hour, which is caused by energy trading intervals [140],[141] and the related power station operation changes. The autocorrelation of mean bulk frequency trajectories reveals prominent peaks every 15 minutes. Discrete power dispatch, which follows a discrete schedule with 15-minute intervals, leads to jumps in the power supply [142]. This behavior can best be seen by calculating a mean value for every time step of a time interval under investigation. Similar as shown before in Figure 21, Figure 26 a) shows the mean bulk frequency for 24 hours of 30 days. The highest peaks occur on the hour, which correlates with the day-ahead trading intervals, the lower but more frequent peaks result from intraday trading.

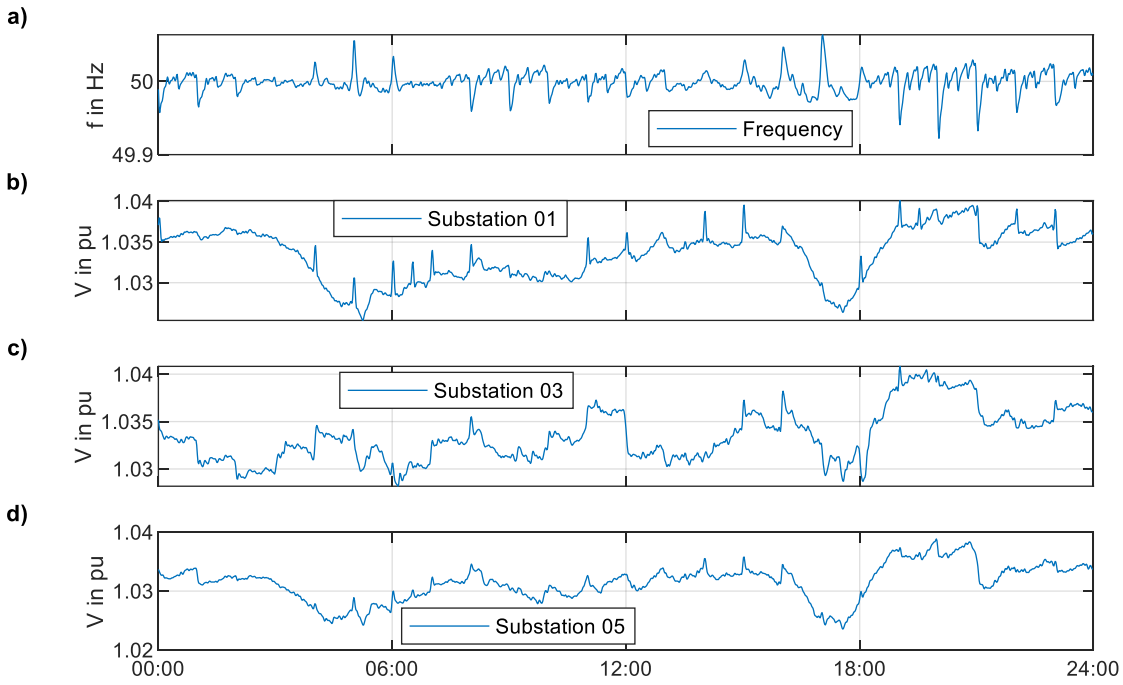


*Figure 26: Mean values of frequency and PMU substation voltages*

Besides in the bulk frequency, these peaks and patterns can also be seen in bus voltages. Figure 26 b)-d) show the 24-hour mean values of three 380-kV voltages in substations where also the neutral point currents NP01, NP03 and NP05 are measured. The substations were chosen because of their geographical locations (see map in 3.2.1).

The voltage in substation 03 in Figure 26 c) shows not only peaks as seen in substation 01 in b) but also remaining changes in the voltage level. Voltage regulation by connection and disconnection of machine transformers because of generation schedules, changes of transformer taps or use of shunt reactors can lead to these discrete voltage steps. The calculation of the daily trajectories of the voltages in the substations reveals that the changes appear exactly at the same time every day. Single events like faults are filtered by the mean calculation, therefore only recurring events lead to prominent peaks in Figure 26 b)-d). This analysis of voltages and bulk frequency in the frequency domain shows (depending on location) prominent peaks similar to those observed in the transformer

neutral point measurements.

Another way to make those periodic events in neutral point currents and substation voltages visible is the application of the autocorrelation function (acf) on the mean daily trajectories. During the autocorrelation, described with equation (60), a signal is shifted in time by τ and compared with itself to find recurring patterns in noisy signals. The autocorrelation of mean neutral point measurements NP01, NP03 and NP05 is shown in Figure 27 a).

$$r_{xx}(\tau) = \lim_{T\to\infty} \frac{1}{2T} \int_{-T}^{T} x(t) \cdot x(t+\tau) dt = \overline{x(t) \cdot x(t+\tau)} \tag{60}$$

An exact acf, meaning a perfect correlation after a sample interval, leads to $r_{xx} = 1$.

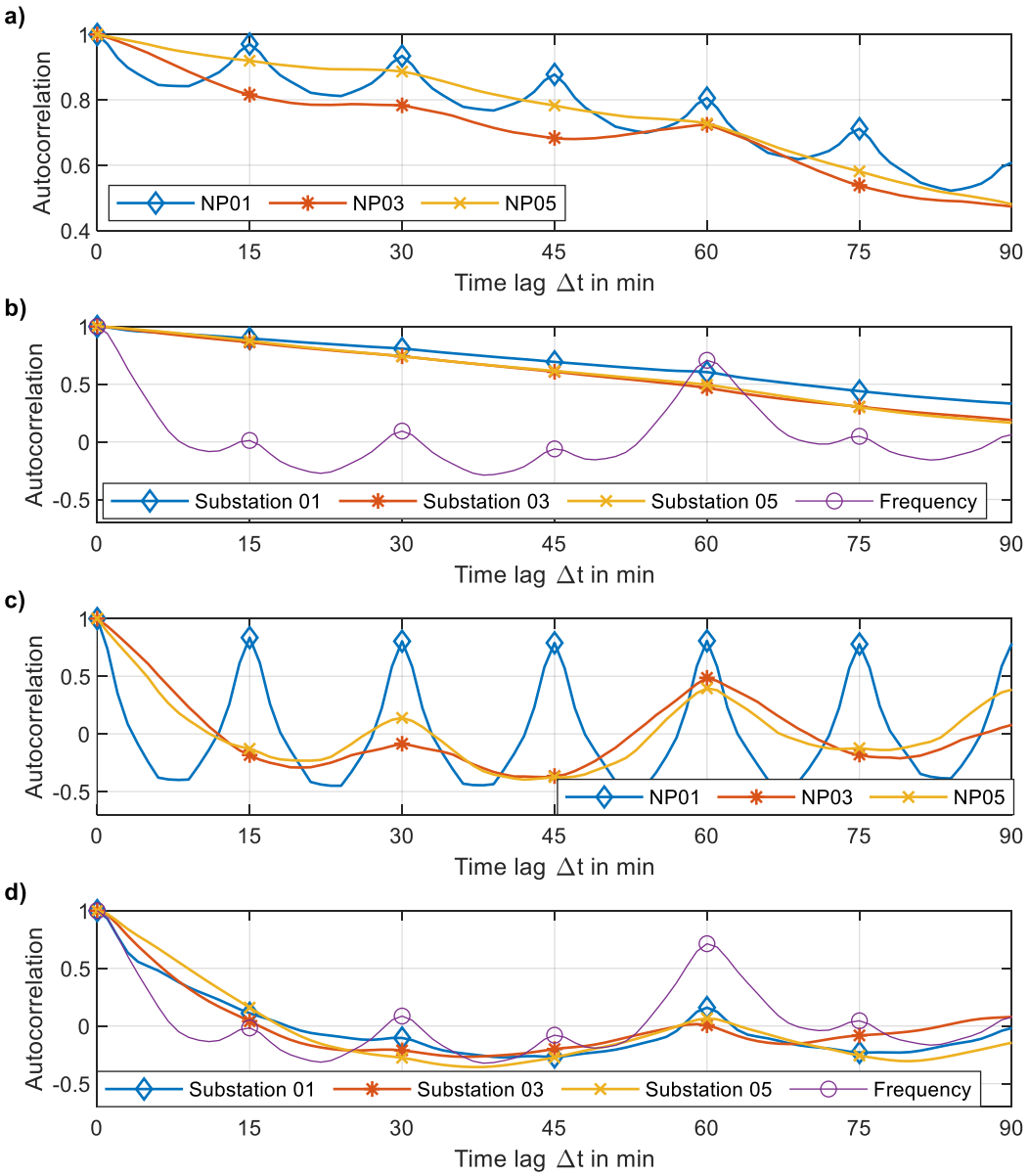


*Figure 27: Autocorrelations of neutral point currents, frequency and voltages. a) neutral point currents, b) voltages and frequency, c) neutral points filtered, d) voltages and frequency filtered*

The different prominent fast changes of the three neutral point current mean trajectories in Figure 21 also lead to different prominent correlation peaks in Figure 27 a). NP01 shows recurrences every 15 minutes, whereas NP03 and NP05 show higher autocorrelation values every 30 and 60 minutes. The autocorrelation of the mean frequency

and mean substation voltage in Figure 27 b) show the expected recurrences and high acf values for the frequency, which origins, as described earlier, from the energy trading intervals. The mean substation voltages, however, show in this plot no recurring patterns and only a steady decay of the acf. This is probably caused by the slow and rather high changes in the substation voltages. To eliminate the slow changes for this analysis, the mean neutral point currents, as well as the mean frequency and voltage data, are high-pass filtered with a cutoff frequency of 0.139 mHz, which is equivalent to a cycle time of 2 hours. This removes slow changes in the measurement signals, e.g. between 17:30 and 19:00 in the voltages, but also limits the acf analysis to time lags lower than 2 hours. Figure 27 c) shows the autocorrelation of the filtered mean neutral point measurements. The slow decay is removed and the recurring patterns of 15 minutes in NP01 and 30 minutes for NP3 and NP5 are now even more prominent. The autocorrelation of the filtered frequency and voltage data is shown in Figure 27 d). The frequency shows no visible change, as there is no slow change in the 50 Hz bulk frequency. Again, the higher acf values correlate with the market trading intervals. However, the substation voltages now show correlations every 60 minutes in all substations and slight correlations every 30 minutes for substations 01 and 03.

The acf of Substation 03 shows a stop of the decay at 30 minutes and a peak value at 60 minutes, which matches with the acf of NP03. Similar behavior can be observed between substation 05 and NP05, although the voltage data of substation 05 show the first peak at 60 60-minute time lag. Nevertheless, a causal relationship can be assumed.

As voltage changes are often caused by switching actions, indirectly caused by energy trading, recurring changes in grid topology are suspected to cause also neutral point currents. This hypothesis is analyzed in to following section 4.3.

## 4.3 Switching in Power Systems

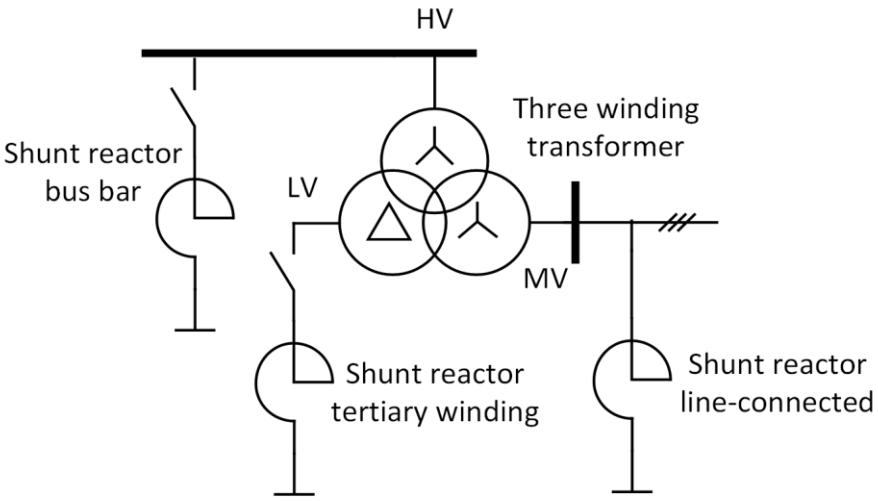


*Figure 28: Three winding transformer with shunt reactor in tertiary winding*

Shunt reactors are used to control the voltage in the transmission grid by compensating reactive power. This can be needed if there is a high number of cables installed or if overhead lines are lightly loaded. Figure 28 shows the typical connections of reactors: They can be directly connected to the lines, at busbars or in the tertiary winding of three-winding transformers [143], which is usually the case in Austria. The shunt reactors can be connected in wye (with or without neutral connection) or in delta and are usually connected via a switch. If the voltage in the grid area is too high, the switch is closed and the reactive power is compensated with the shunt reactor. Shunt reactors can be classified by their cooling medium (dry or oil) and by their core type, which can be gapped core or coreless [144, 145]. A gapped core type reactor is similarly constructed as a transformer but the core consists of steel plates

divided by air gaps. This design leads to a wider linear operating range before the core saturates. Coreless reactors, also known as air-core reactors, are not affected by saturation and therefore no remanence flux has to be considered for inrush calculations. Both reactor types can be constructed with a fixed rated power or as variable shunt reactors VSR with a variable rating, changed with a tap changer or with thyristor switches.

During the turn-on of inductors, high inrush currents occur, caused by the magnetization of the coil.

Assuming the voltage v(t) is perfectly sinusoidal and can be described with (61), the currents during the energization of the shunt reactor can be described as i(t) with (62).

$$v(t) = \hat{V}\sin(\omega t + \varphi) \tag{61}$$

$$i(t) = \frac{\hat{V}}{|Z|}\sin(\omega t + \varphi - \theta) - \underbrace{\frac{\hat{V}}{|Z|}\sin(\varphi - \theta)\, e^{-\frac{t}{\tau}}}_{DC\ component} \tag{62}$$

$$|Z| = \sqrt{R^2 + (\omega L)^2} \tag{63}$$

$$\theta = \arctan(\frac{\omega L}{R}) \tag{64}$$

$$\tau = \frac{L}{R} \tag{65}$$

Typically, the resistance of shunt reactors (e.g. 0.07 Ω) is very low compared to the reactance (e.g., 27 Ω), which means the losses are usually low. Because of the small resistive part, the damping of the DC component is very low (high X/R ratio) and it can take several seconds before it decays completely. The small resistance also means that the angle $\theta$ is close to 90°. If the connecting switch is closed at the zero voltage crossing, the DC component will be at the maximum. The inrush current phenomena and a possible current transducer saturation are well known, especially in the field of protection engineering. When the shunt reactor is connected directly to the busbar, the asymmetric close of the switches during energization leads to high zero sequence currents and high neutral point currents in the shunt reactors [145]. To reduce these currents, point-on-wave relays connect each phase individually at the peak voltage, leading to far lower neutral currents [144, 146]. To illustrate this behavior, a small grid with shunt reactors was simulated. The grid shown in Figure 29 consists of two transformers 600 MVA, connected with a 50 km overhead line, and two 100 Mvar shunt reactors, one connected at a busbar, one in the tertiary winding of Transformer 2. Both shunt reactors are modelled as air-core types, meaning the magnetizing curve is linear.

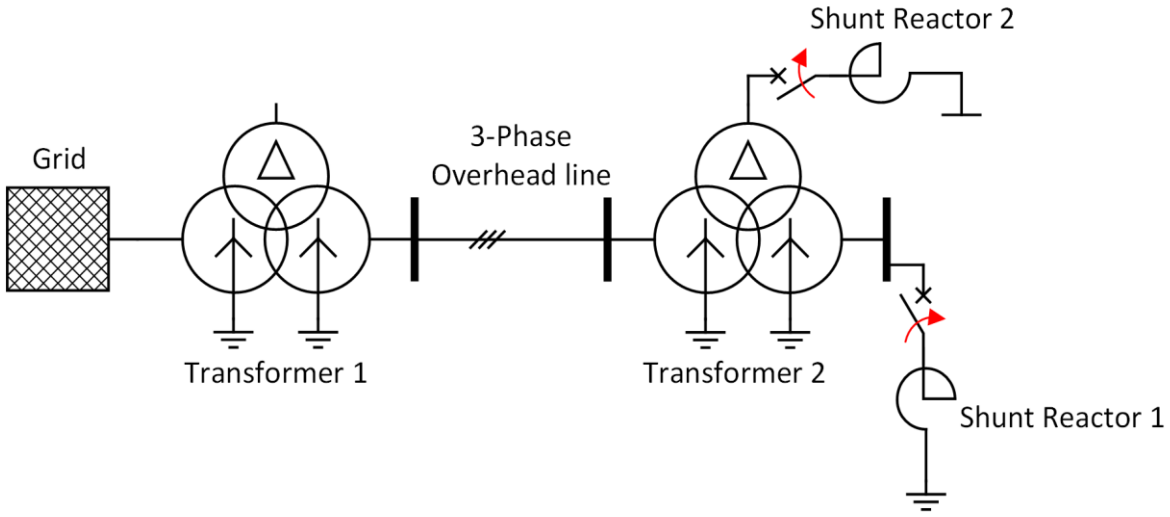


*Figure 29: Grid with shunt reactors*

At t = 1 s, the switch of shunt reactor 1 is closed and the reactor is energized. Figure 30 shows the neutral point currents of shunt reactor 1 during the turn-on process for the worst and optimal switching time. Depending on the grounded transformer neutral points, the DC flows through various transformers, leading to saturation of various assets. It is clearly shown, that the energization at the peak voltage leads to lower neutral point currents, meaning the possible saturation of e.g. current transformers is lower and the impact on the grid is not as critical.

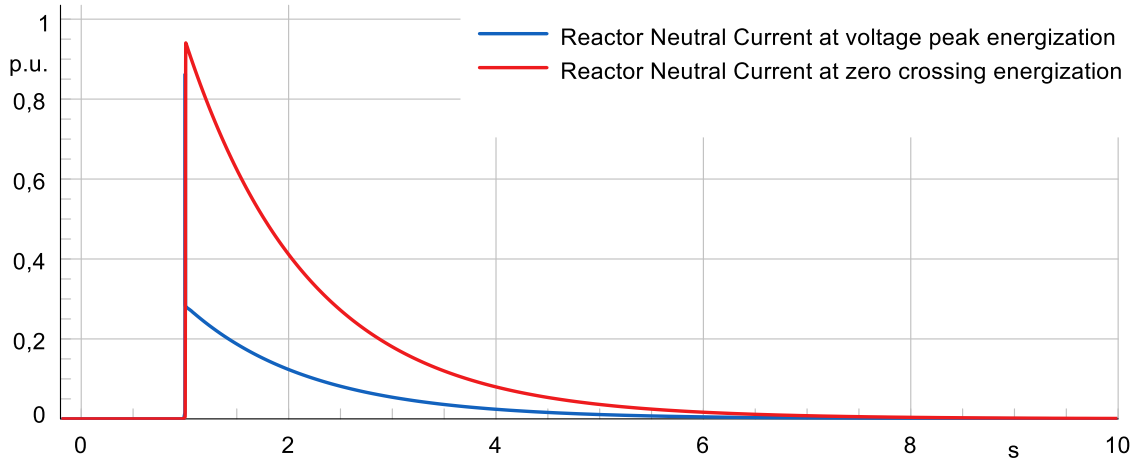


*Figure 30: RMS neutral point currents of busbar shunt reactor during energization*

The analysis of the inrush impact of tertiary connected shunt reactors is more complex. The tertiary winding as well as the shunt reactor is connected in delta, meaning there is no path for a zero-sequence current. If the grid is perfectly symmetrical and the voltage on the transformer HV side has only a positive sequence component, only positive and negative sequence currents occur and no DC inrush current can be observed during the shunt reactor energization on the tertiary winding. This is also the case if the voltages on the HV side are unsymmetrical because of unsymmetrical loads.

In reality, there is a slight asymmetry in transmission lines because of different line lengths (a few meters), not perfect transposition of overhead lines etc. This slight asymmetry leads to small neutral point currents in the transformer during the energization of a tertiary-connected shunt reactor. To demonstrate this effect, one phase of the overhead line in Figure 29 is 1% longer than the other two phases. Shunt reactor 2 is connected at t=1 s, leading to the neutral point currents in the HV neutral point shown in Figure 31. The already present zero-sequence, which is caused by the line asymmetry, gets shifted by an exponentially decreasing DC component.

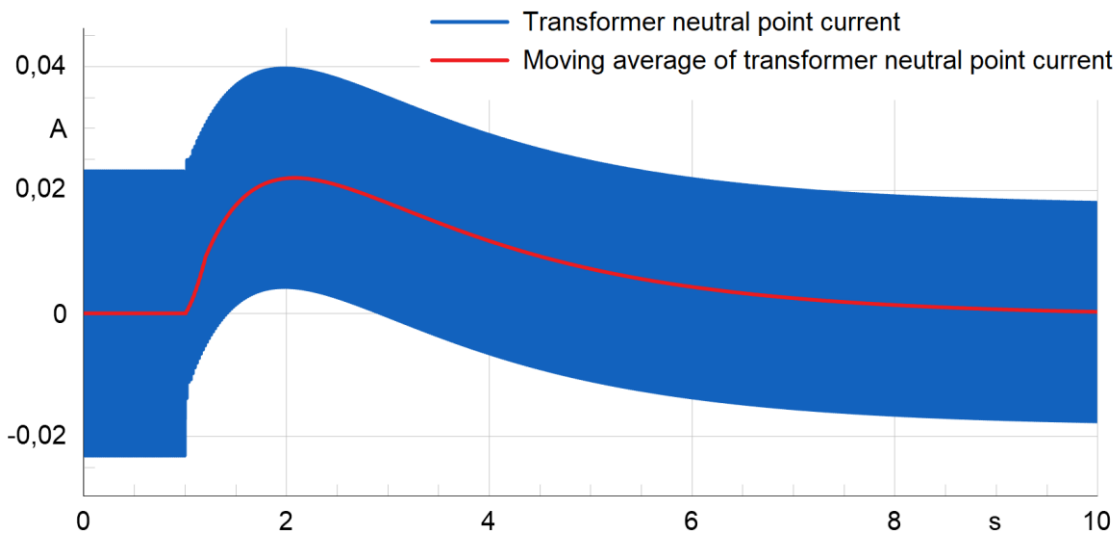


*Figure 31: Transformer neutral point currents during energization of tertiary connected shunt reactor*

Without discussing the magnitude of this DC component in the simulation, this behavior can be found in the real neutral point measurements. The data in the following figures contains the neutral point measurements, phasor measurement data as well as information about switching events provided by the transmission system operator. However, as these two sources are not synchronized and especially the neutral point measurement only samples with 1 Hz, the data is not aligned perfectly.

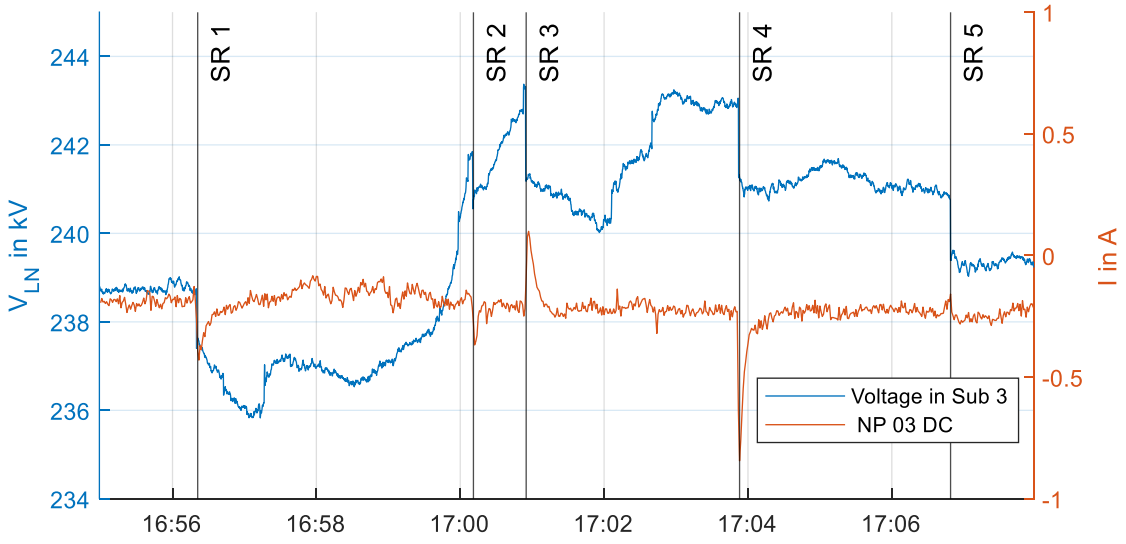


*Figure 32: Exemplary shunt reactor connections and relating neutral point currents. Blue – voltages in substation 03, orange – neutral point currents NP 03*

As mentioned before, shunt reactors are used to reduce the voltage on low-loaded lines. Typically, high changes in line loads occur at market interval times (15 min, 30 min, 1 hour), when large power plants change their operation point. Figure 32 shows a typical time when the voltage is controlled by connecting shunt reactors. The five shunt reactors SR 1 – SR 5 are located in Sub 3 and in close substations to Sub 3. Every time a shunt reactor is energized, depicted as a vertical line, the voltage decreases rapidly and causes a neutral point current in NP03. The magnitude of the neutral point current depends on the location of the shunt reactor, the time of connection as well as the grid symmetry, as described above.

For a limited period, the neutral point measurement system at NP03 was extended with an AC measurement part,

capable of measuring neutral currents with 5 kHz. In Figure 33 a detailed view of a typical voltage regulation with AC and DC neutral point measurement is shown. Again, the three shunt reactor connections regulate the voltage as desired, leading to neutral point currents. In the AC measurement, a zero-sequence current is already present before the shunts are connected, matching the simulations above. The magnitude of the neutral point current is not only affected by the distance to the energized shunt reactor: SR 1 in Figure 33 is close to the neutral point measurement system (connected via a 12 km long 380 kV line) but results in this case in far smaller neutral point currents than the energization of SR 2, which is connected via a 100 km long line.

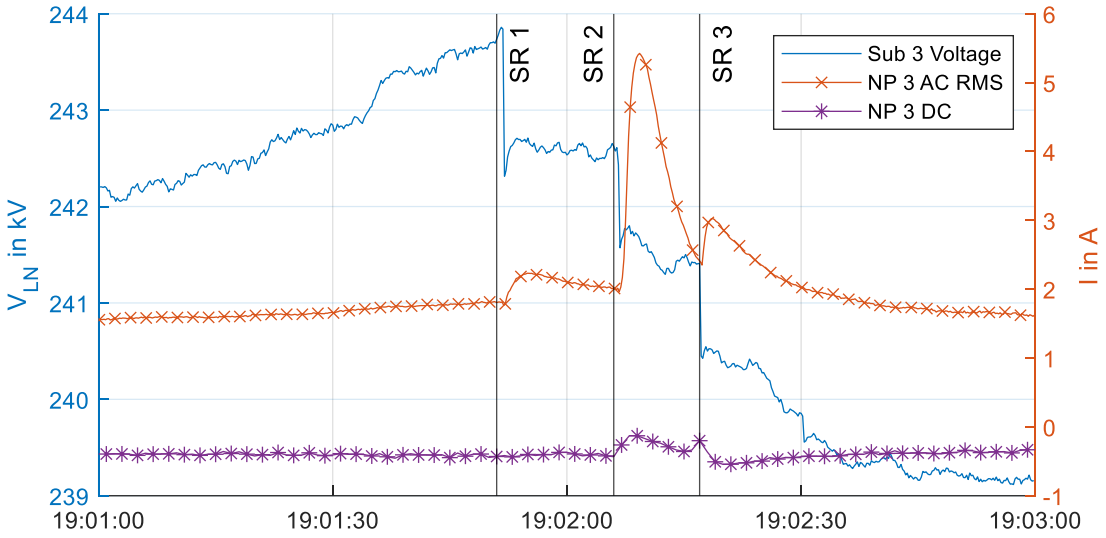


*Figure 33: Detail shunt reactor connections with influenced voltage and related neutral point current. Blue – voltage in substation 3, orange – AC RMS in neutral point current, violet – DC neutral point current*

That this shunt switching effect is not only a local phenomenon is shown in the following in other grid areas with more installed measurement systems.

Figure 34 shows a typical pattern of neutral point currents during the connection of shunt reactors in the tertiary winding in the grid area of NP05 and NP06. The first connection happens in the substation where NP05 is located, and the second in the same substation as NP06. The two substations are directly connected via approx. 110 km of two 380 kV and two 220 kV lines.

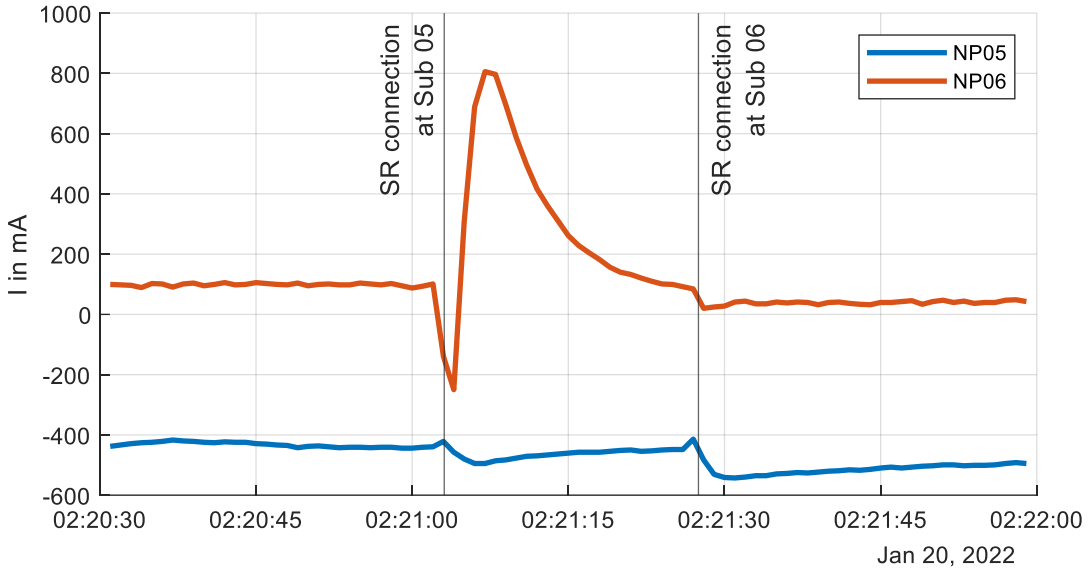


*Figure 34: Shunt reactor connection example at Substation 05 and Substation 06*

This effect does not occur only once but can be observed regularly at all measurement points in the grid. However, the amplitude, sign, decay time and range vary a lot. Figure 35 shows samples of the discussed shunt reactor energizations. The colored area marks ±10 seconds around the energization of the shunt reactor. The green areas mark the connecting process in Substation 05, where NP05 is installed and the yellow area marks Substation 06 and NP06.

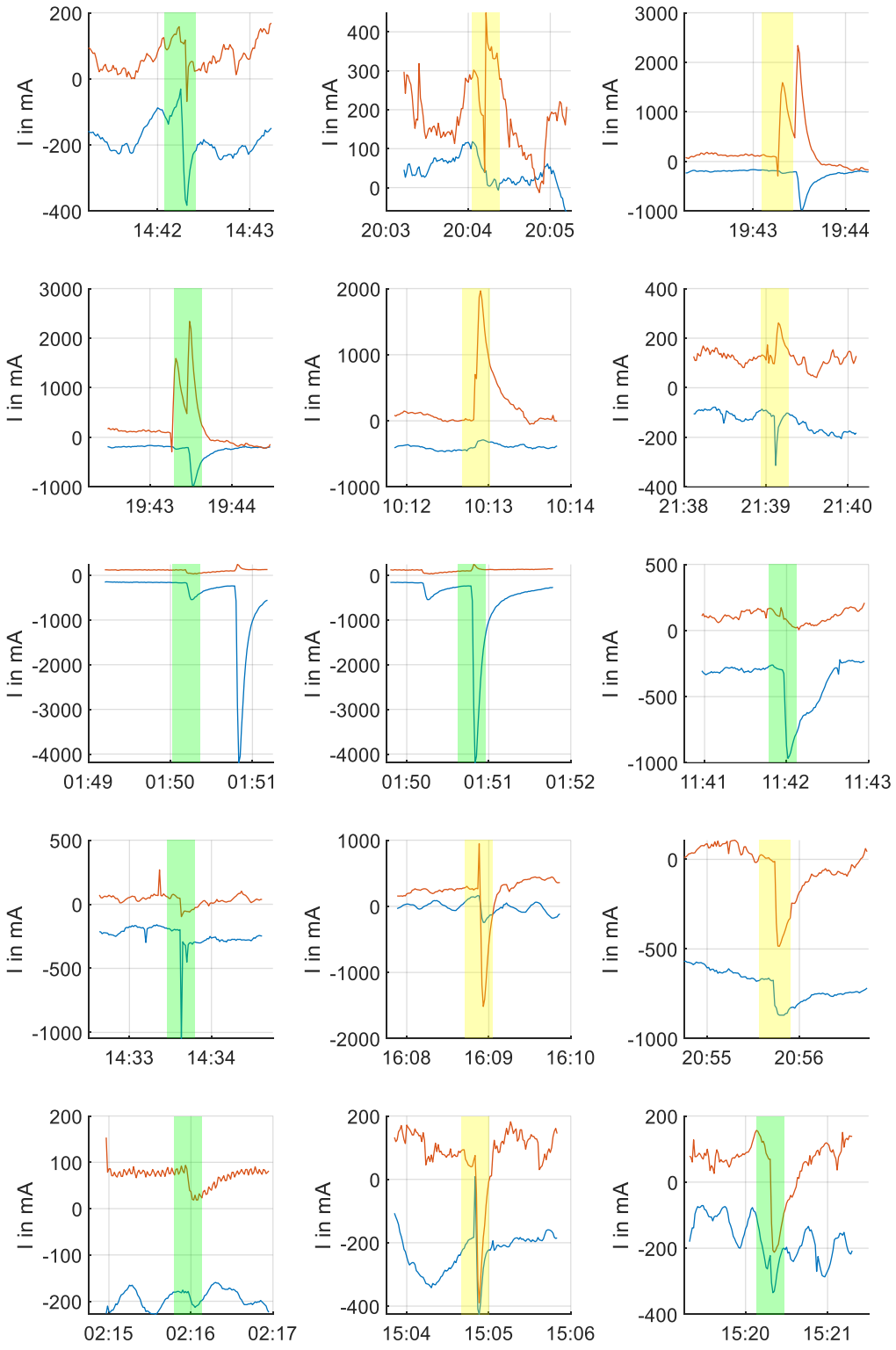


*Figure 35: Shunt reactor connections. Blue – NP05, red – NP06. Green marked – SR at Sub05, yellow marked – SR at Sub06*

The same effects can be observed during shunt reactor connections in substation 1 in Figure 36. The yellow area again marks the time around the circuit breaker closing and turning on the shunt reactor. The three shown neutral point currents are at NP01 (blue), NP04 (orange) at substation 1 and NP07 (yellow) at substation 7. The DC currents, caused by the shunt energization, can be clearly seen again, but there are major differences visible. First of all, there is a higher noise level visible, which was also discussed in Chapter 3. Because of this noise, the peaks caused by shunt reactors are not as prominent during the day as during the night. Secondly, although NP01 and

NP04 are in the same substation, not every peak is visible in both measurement points, the reason has yet to be found. And finally, although substation 1 and substation 7 are closer together than substation 5 and 6, no current peaks caused in substation 1 are visible in NP07.

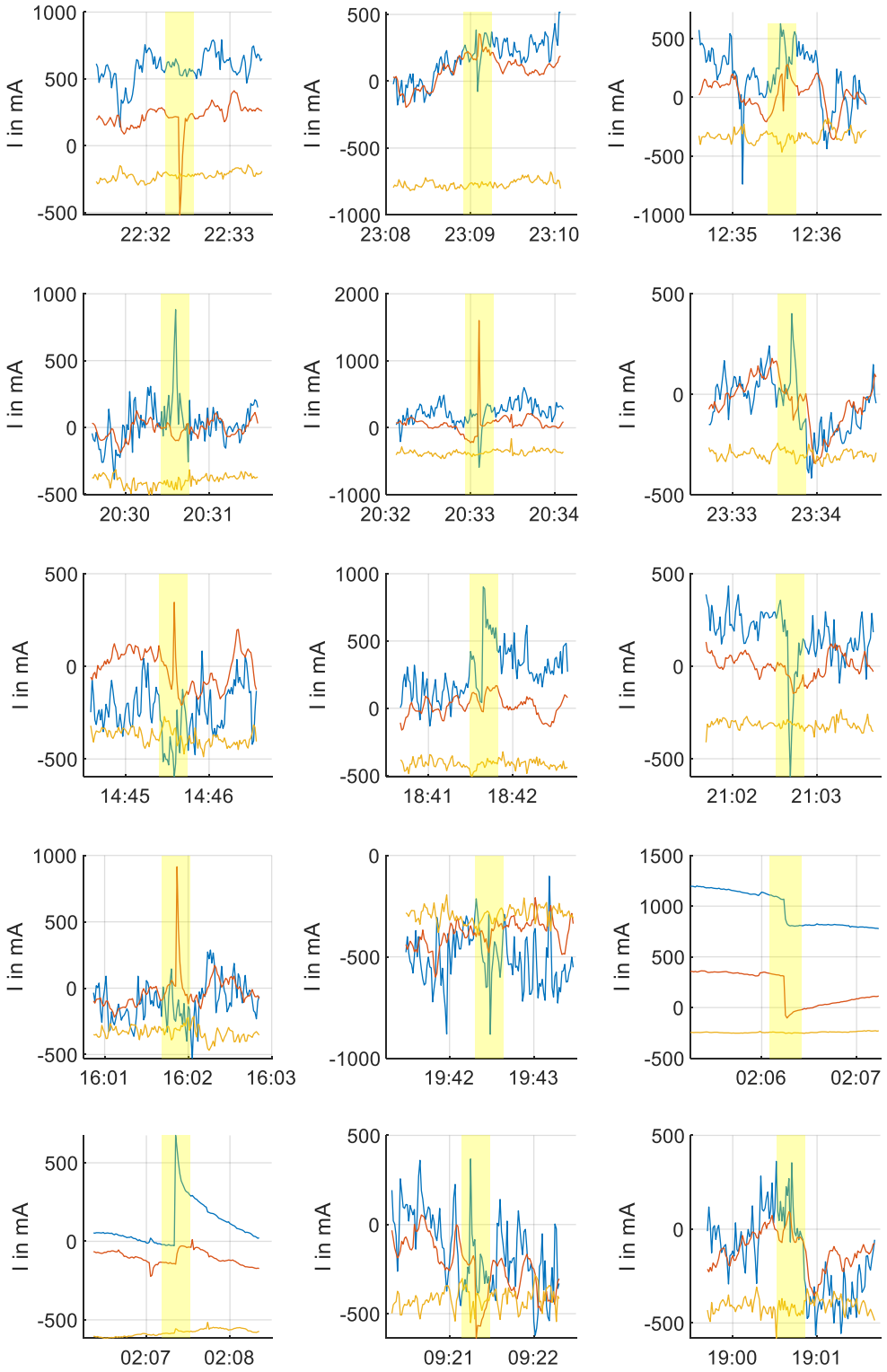


*Figure 36: Shunt reactor connections. Blue – NP01, red – NP04, yellow – NP07. yellow marked – SR at Sub01*

Similar effects, but with a faster decreasing DC component in the neutral point can be observed during tap changes in transformers. Figure 37 shows tap changes in substation 6 and neutral point currents of NP05 and NP06. The

green and red marked switching actions show tap changes of the two parallel transformers in substation 6, whereas the cyan marked times are tap changes of a phase shifting transformer in substation 6.

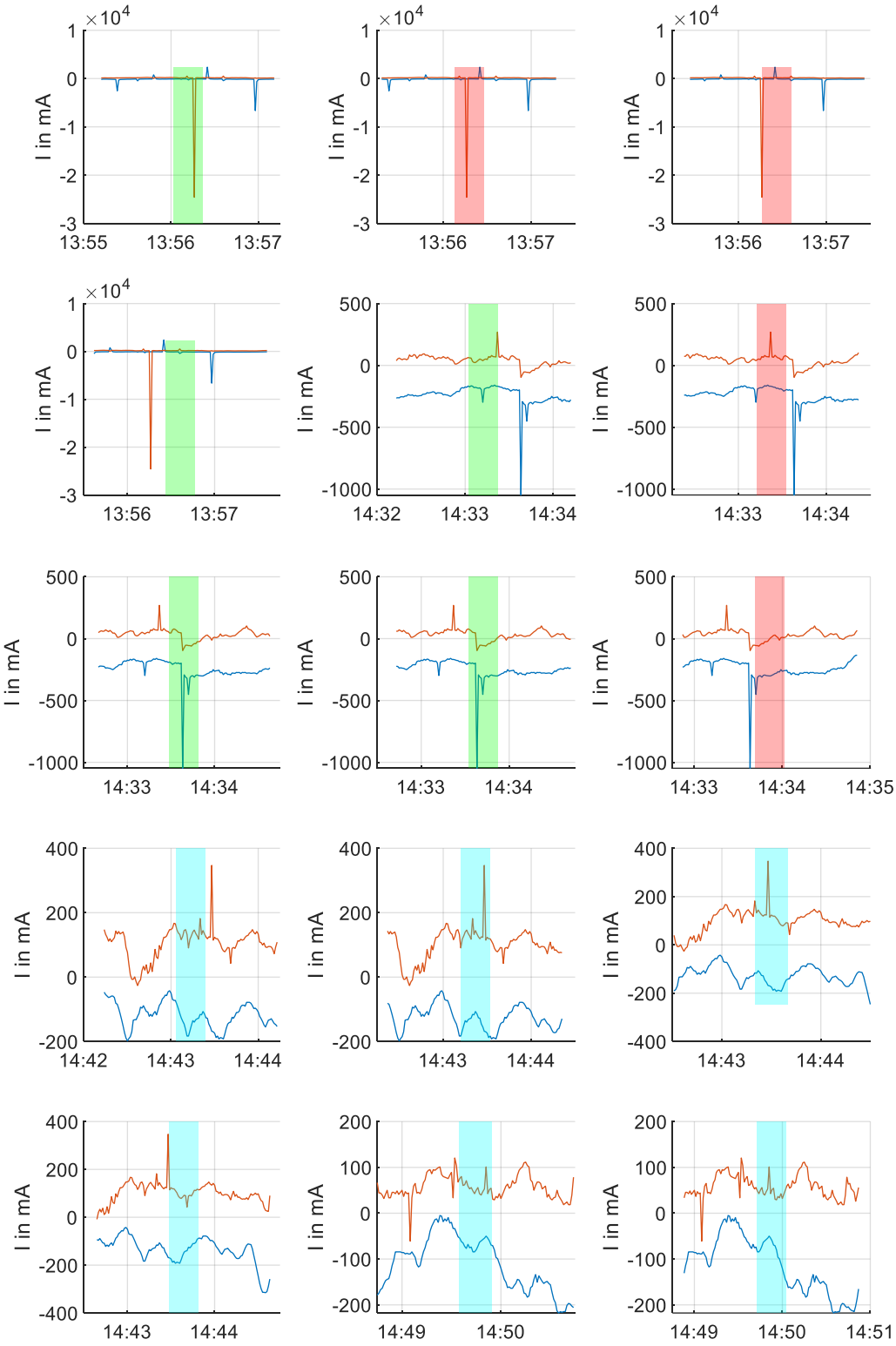


*Figure 37: Tap changes. Blue - NP05, red - NP06, marked - tap changes*

The identification of switching actions in the transmission grid as an LFC source is only possible with protocols from the TSO, as some switching actions are simultaneously performed or at least close together. For example, voltage control (outside of power stations) can be done with shunt reactors and with transformer tap changes and Figure

38 shows, that it is not one or the other but an interaction between several measures. Figure 38 additionally shows, that not all tap changes lead to a measurable change in the neutral point currents.

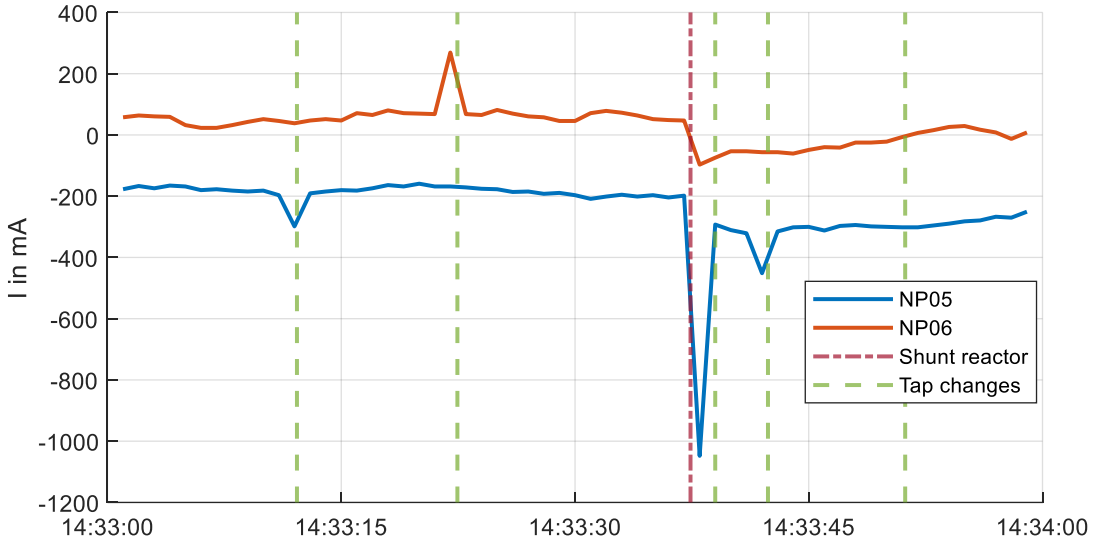


*Figure 38: Transformer tap changes and shunt reactor connections*

## 4.4 Power Electronics

Power electronic devices have been assumed to be LFC sources for some time. This includes distributed generation and power electronic converters [147] and DC ion current coupling between AC and HVDC lines [148, 149]. However, a measurement-based proof, that power electronics lead to increased low frequency neutral point currents is has yet to be found.

During a test of a digital power flow controller in the Austrian transmission grid, AC and DC measurements were performed in nearby neutral points. This device is connected in series with a line and injects a voltage to control the power flow on the line. For this purpose, in addition to the low frequency neutral point measurement system, a power system analyzer was installed. This allowed the measurement of AC and DC currents in the neutral point. Depending on the operational mode, increasing AC and DC neutral point currents were observed.

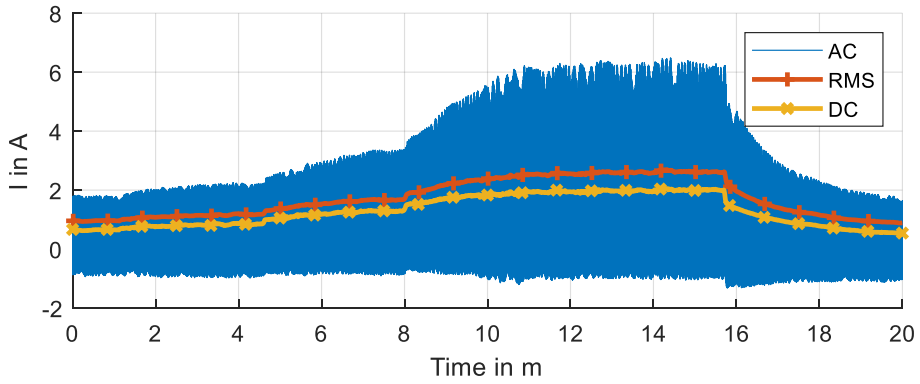


*Figure 39: Power electronic influence: blue – AC neutral point current, orange – RMS value of AC, yellow – low pass filtered DC neutral point current*

Figure 39 shows an example measurement during this test phase. The test started with already present neutral

points, caused by other sources. The injected voltage was ramped to a set value, which was then increased again. During the ramping, not only does the AC neutral point increase but also an increasing DC can be observed. Shortly before minute 16, the set point of the device was set to 0 and the neutral points decreased again. Other tests revealed that the sign of the injected voltage, i.e. the operational mode, has a high impact on the neutral point amplitude.

The digital power flow controller was only in operation for a few weeks, however, it clearly showed the impact on neutral point currents.

## 4.5 Space Weather

The highest neutral point currents, which also lead to major disturbances in power grids, are caused by geomagnetic disturbances. As already described in 2.4, the changes in the Earth's geomagnetic field lead to an induced electric field in the Earth's conductive surface, leading to LFCs in transformer neutral points. This process and the effects of it on the example of Austria are described in the next chapter.

## 4.6 Summary of LFC Sources

Public transport systems near neutral point measurement systems were identified as an LFC source in [5]. This was proven in this work. The measured current fluctuations correlate with the operating times of the subway system. Due to COVID-19 restrictions and a special operating timetable for the Vienna subway system, changes in the neutral point current pattern were identified which correlate with high neutral point measurements in close transformers. In addition to neutral point measurements, a voltage between the public and the subway earthing systems was analyzed. For this purpose, mobile DAQ systems were placed in the subway system for several days. The recorded patterns correlate with the neutral point currents, giving another indication of this connection.

Periodically bulk frequency deviations, which occur at the same time as deviations in neutral point measurements, lead to hypotheses of a connection. For the analysis, line voltages in substations with neutral point measurements were analyzed in detail. The bulk frequency, the voltages as well as the neutral point currents show similar recurring patterns. However, the physical and mathematical relation was not completely found.

Switching in power systems leads to inrush currents in the grid, but the connection to LFCs in transformer neutral points was missing. By combining neutral point measurements, line voltages and switching protocols from the TSO, a connection was formed. Calculations show, that due to asymmetries in the grid, the energization of shunt reactors in transformer tertiary windings leads to neutral point currents, although the tertiary winding is connected in delta without an earthing connection. But not only shunt reactor energizations lead to LFCs, also changing the transformer tap leads to spikes in neutral point measurements. These identified currents are rather small compared to currents during a solar storm, however, the usually low-pass filtered measurements are now better known.

Large power electronic structures are under suspicion to lead to LFCs. There are no HVDC lines in the Austrian Power Grid, but a digital power flow controller was in operation for a limited period. During this time, increased neutral point currents were measured, which correlate with the operation of this electronic device.

# 5 Calculation of GICs in the Austrian Transmission System

The calculation of GICs and the related effects on power grids consists of several stages, which are depicted in Figure 40. First, the input dataset (orange) needs to be prepared and formatted. The power grid data must include all lines, transformers, substations (with coordinates) and the relation of all these assets. The magnetic field measurements need to include measurements in latitudinal and longitudinal directions as well as a timestamp. Earth models include the resistivity of earth layers and the related depths. Electric field scenarios can be used to analyze worst-case scenarios or to perform different sensitivity analyses. This replaces the electric field calculation from magnetic field measurements. Subsequently, this data is processed and GIC calculations are performed, resulting in transformer currents. These currents are then compared to measured transformer neutral currents, reactive power demand is calculated, harmonics are estimated and mitigation actions are proposed. In the following, these calculation steps are described.

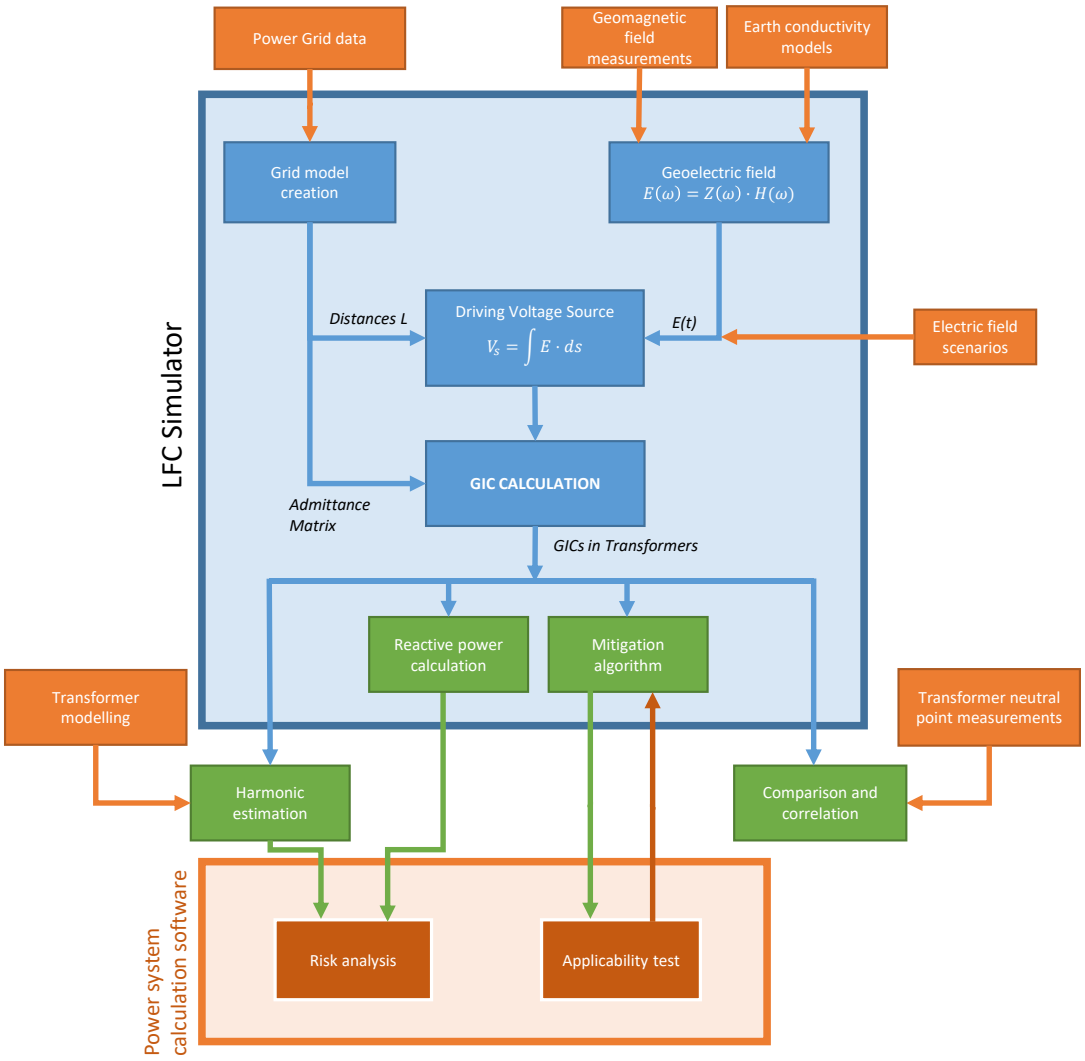


*Figure 40: GIC calculation method flowchart*

To perform GIC calculations fast and to provide the calculation method in an easy-to-use way to the scientific community and industrial partners, the LFC-Simulator was developed. It is a free-to-use Matlab app and is available at https://github.com/IEAN-TUGraz/LFC-Simulator.


*Figure 41: LFC-Simulator graphical user interface*

The GIC calculation is based on the plane-wave method, 1-D earth models and the nodal admittance method, described in 2.4. Figure 41 shows the main interface of the LFC-Simulator.

The LFC-Simulator also provides a quick graphical overview of the input data and simulation results in the form of different plots. The main window therefore shows the measured magnetic field data as time series and frequency spectra, the transfer function of the selected earth model, the time series of the calculated electric field, the simulated currents of transformers and the additional reactive power demand of a selected transformer. For further analysis, the results can also be exported into different file formats.

The different input datasets, results, simulation accuracy, sensitivity analysis, and usage of the results will be discussed in the following sections.

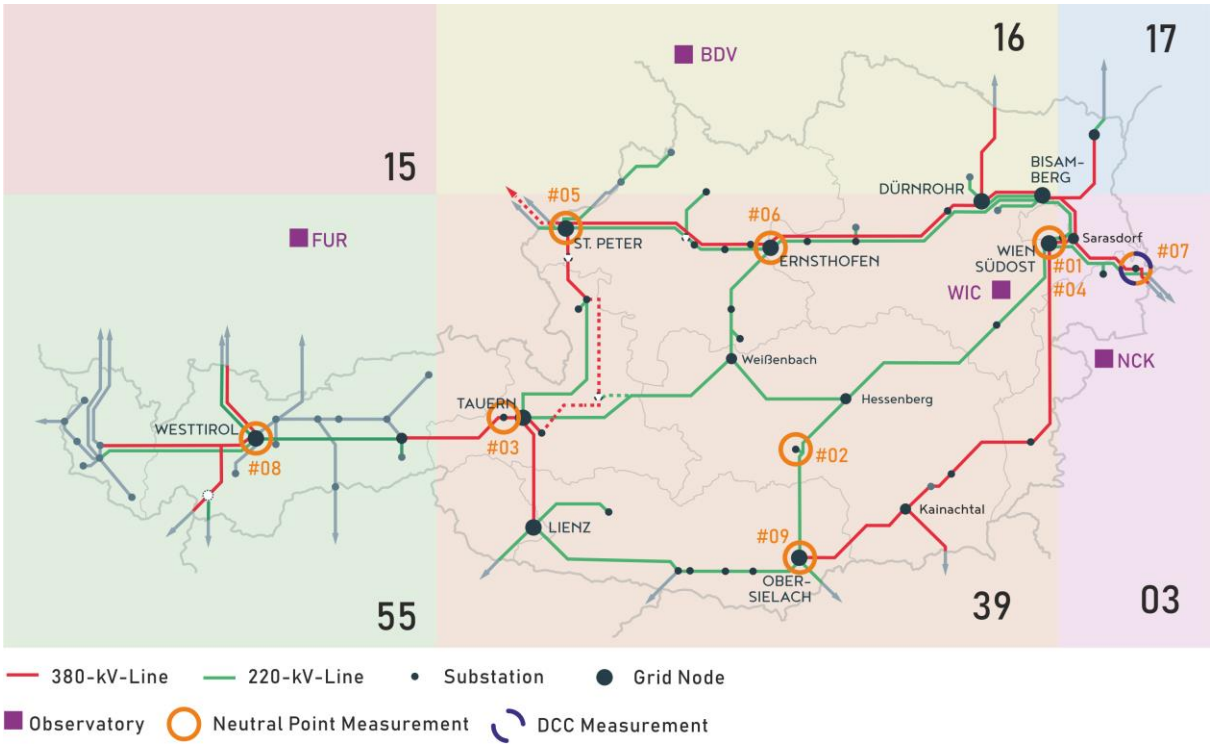


Figure 42: Earth models, observatories, Austrian power grid and neutral point measurement locations

To rate the influence and the simulation accuracy, several measures for the goodness of fit between simulation and measurement are used. The three evaluation parameters are the root mean squared error RMSE, the Pearson's correlation coefficient R and the performance parameter P. All three parameters use and compare the observed (real) value $o_i$, the mean observed value $\bar{o}$, the modelled value $m_i$ and the mean modelled value $\bar{m}$ in different ways. The number of observed and modelled values is N.

The RMSE, calculated with (66), is a piecewise comparison between observed and modelled values. In the used case the results are in Ampere. The disadvantage of this simple calculation is, that a slight time shift, wherever it may come from, may result in large differences and hence in large RMSE. A perfect match between the observed and modelled signal results in RMSE = 0.

$$RMSE = \sqrt{\frac{\sum_{i=1}^{N}(o_i - m_i)^2}{N}} \tag{66}$$

The Pearson's product-moment correlation coefficient, well-known in statistics, is a measure of the linear relation of two variables. It can take values in the interval of -1 to 1, where 1 means a perfect linear correlation and -1 means an anti-correlation.

$$R = \frac{\sum_{i=1}^{N}(o_i - \bar{o})(m_i - \bar{m})}{\sqrt{\sum_{i=1}^{N}(o_i - \bar{o})^2}\sqrt{\sum_{i=1}^{N}(m_i - \bar{m})^2}} \tag{67}$$

The performance parameter P in (68), used by [4, 150], compares the residuals of the observed and modelled time series. Values close to 1 indicate a good model, whereas negative values show anti-correlation. However, even a very good model only leads to P of around 0.6 [4].

$$P = 1 - \frac{1}{\sigma_o}\sqrt{\frac{\sum_{i=1}^{N}[(o_i - \bar{o}) - (m_i - \bar{m})]^2}{N}} \tag{68}$$

Additionally to these three measures for the goodness of fit, also a visual comparison of modelled and observed time series is applied.

## 5.1 Magnetic Field Measurement Data

Conrad Observatory (WIC) in Muggendorf in the south of Vienna is an INTERMAGNET-qualified ground-level observatory in a tunnel system. It is operated by GeoSphere Austria and provides 1 sample/second magnetic field measurements in x-, y- and z-direction. As described in section 2.4.1, only magnetic field changes in x- and y-direction lead to induced electric fields, therefore only these values are used in all further calculations.

There are also other nearby ground-level observatories around Austria, e.g. Budkov (Czech Republic, BDV), Fürstenfeldbruck (Germany, FUR) and Nagycenk (Hungary, NCK). These observatories are also marked in Figure 42. Since Austria is a relatively small country, the deviation in the geomagnetic field over the area is rather small and negligible. To prove this assumption, Figure 43 shows measurements of the four observatories WIC, BDV, FUR and NCK. The results are baseline adjusted, as only the change of the magnetic field leads to an induced electric field.

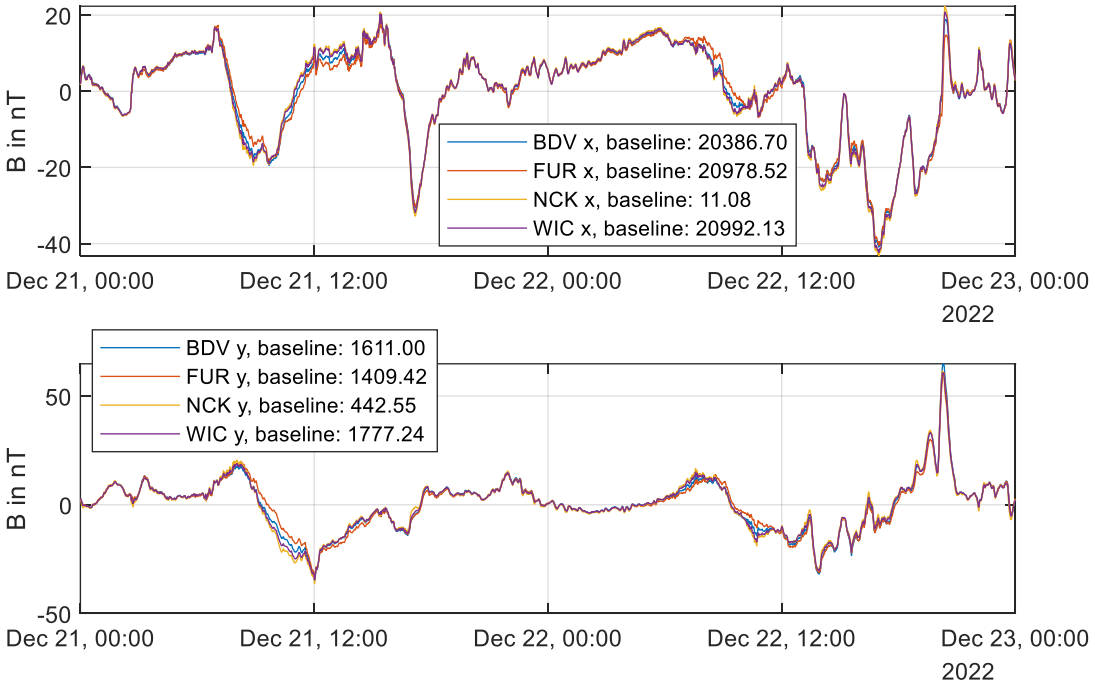


*Figure 43: Comparison B measurement (baseline adjusted) from different observatories*

In the following, the derivative of magnetic field data dB/dt originating from different observatories is analyzed with respect to correlation. The calculation results of the Pearson's correlation coefficient R between the magnetic field changes of two stations are shown in TABLE 4. The RMSE between magnetic field changes at WIC and another station is lower than 1 nT/min. The graphical interpretation of Figure 43, the high correlation values R and the very low RMSE values support the single observatory usage method.

*TABLE 4: Pearson's correlation coefficients and RMS error between magnetic field changes from two stations in x- and y-direction*

| | WIC TO BDV | WIC TO FUR | WIC TO NCK |
|---|---|---|---|
| **R($dB_x/dt$)** | 0.9899 | 0.9871 | 0.9888 |
| **R($dB_y/dt$)** | 0.9908 | 0.9753 | 0.9782 |
| **RMSE ($dB_x/dt$)** | 0.0788 | 0.0835 | 0.0949 |
| **RMSE ($dB_y/dt$)** | 0.0734 | 0.1164 | 0.1502 |

If the area of investigation is larger and this assumption is not valid anymore, the magnetic field can be interpolated between several observatories [151, 152].

Before using the magnetic field data to perform the electric field calculations, it is necessary to preprocess and precondition the dataset, which is described in the following: To reduce the spectral leakage, which occurs after the FFT transformation of a discontinuous time series signal, it is reasonable to remove the mean value and to taper both the start and end of the time series. This tapering procedure is performed using a cosine bell window [153] and avoids disturbing frequency components, although, it also influences the dataset of interest. Equation (69) shows the used window function from [153], where p is the proportion of the data that is tapered by the window. To prevent the damping influence of the tapering on the data of interest, it is advisable to add data before and after the time of interest and remove these data again in the post-processing. [154]

$$w_p(t) = \begin{cases} \frac{1}{2}\left(1 - \cos\left(\frac{2\pi t}{p}\right)\right), & 0 \le t \le \frac{p}{2} \\ 1, & \frac{r}{2} \le t \le 1 - \frac{p}{2} \\ \frac{1}{2}\left(1 - \cos\left(\frac{2\pi(1-t)}{p}\right)\right), & 1 - \frac{p}{2} \le t \le 1 \end{cases} \quad (69)$$

## 5.2 Earth Layer Models for Austria

The calculation of the electric field is done with the plane wave method and 1-D earth layer models, which are described in detail in section 2.4.2. Based on the EUROHM [61] dataset, Austria can be described with five different layer models, as depicted in Figure 43. The conductivity layers and related depths for those models are presented in TABLE 5. Each column represents a model data set with the number in the header referring to the EUROHM model. Each model is characterized by the number of layers and their resistivity and thickness respectively. For the lowest layer, no thickness is given since it extends unlimited.

*TABLE 5: 1-D earth layer model data for Austria from [61]*

| | 03 | | 15 | | 16 | | 17 | | 39 | | 55 | |
|---|---|---|---|---|---|---|---|---|---|---|---|---|
| LAYER | **ρ in Ωm** | **d in km** | **ρ in Ωm** | **d in km** | **ρ in Ωm** | **d in km** | **ρ in Ωm** | **d in km** | **ρ in Ωm** | **d in km** | **ρ in Ωm** | **d in km** |
| 1 | 5 | 3 | 1 | 4 | 1500 | 20 | 2000 | 100 | 1000 | 55 | 110 | 0.9 |
| 2 | 1000 | 57 | 200 | 4 | 500 | 20 | 25 | | 300 | 45 | 30 | 1.1 |
| 3 | 10 | | 0.5 | 1.5 | 800 | 110 | | | 1000 | | 10000 | 150 |
| 4 | | | 200 | 2 | 10 | | | | | | 90 | |
| 5 | | | 1000 | 100 | | | | | | | | |
| 6 | | | 10 | | | | | | | | | |

As shown in [4], Model M39 leads to the best simulation accuracy for Austria. Therefore, most of the calculations in this thesis will be done with M39. Nevertheless, in section 5.4, the influence of another Earth model on simulation accuracy will be discussed.

With this data, the electric field calculation, as described in section 2.4.2, can be performed.

## 5.3 Power System Calculation

### 5.3.1 Sensitivity Analysis

Depending on the electric field direction, each node/transformer is exposed to more or less GICs. This is called the sensitivity. A sensitivity analysis is a fast way to identify the direction of the electric field, where the highest current in each grid element occurs and in which direction the highest thread to the grid has to be expected.

For a general sensitivity analysis, an electric field E with constant magnitude and varying angle $\vartheta$ is used, as depicted in Figure 44.

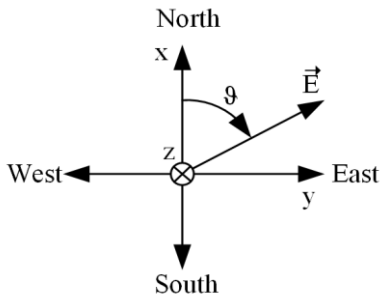


*Figure 44: Coordinate System with rotating E-field*

In Figure 45, the sensitivity analysis with a rotating electric field with E = 1 V/km is shown for the Austrian power grid. Each arrow depicts the magnitude of the worst-case current in the related transformer, where green arrows depict a 220 kV transformer and red a 380 kV transformer respectively. The angle of the arrow indicates the direction of the E-field corresponding to the maximum current. The resulting information can be used in several ways, e.g. as an indication where measurement systems should be installed or which transformers are exposed to high GICs. In combination with historical magnetic field measurements, high transformer currents can be analyzed on their occurrence probability. This means if a transformer is sensitive to electric fields in south-eastern direction but during a solar storm high electric fields only occur in north-western direction, the currents and hence the risk for this transformer is low.

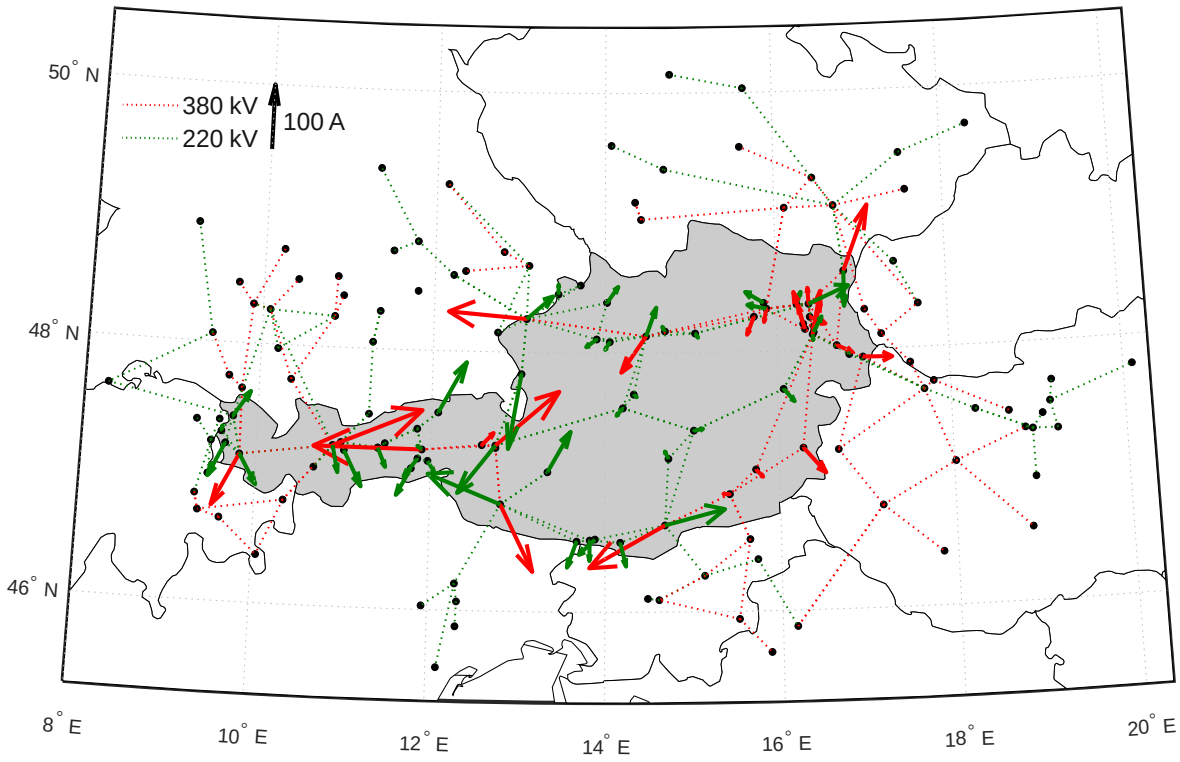


*Figure 45: Sensitivity analysis for the Austrian transmission grid with a rotating electric field E = 1 V/km*

As shown in [5], the maximum currents for each transformer in the Austrian power grid can be calculated and the change of these currents with future grid scenarios can be compared. This can be used during grid planning processes to see the influence on future grids. However, as changes in the grid topology have a high influence, as will be shown in the next sections, sensitivity analysis should be performed regularly.

### 5.3.2 Parameter study

Despite the magnetic field change (electric field direction), other modeling parameters influence the accuracy of GIC calculations. These parameters are basically the used earth models and unknown grid parameters.

Unknown parameters in the grid or non-recognized changes in the grid topology are one of the main reasons for modeling errors. The following three parameters are analyzed in detail:

- Substation grounding resistance
- Number of connected neutral points
- Line outages

**Substation Grounding**

The substation grounding resistance $R_G$ is the resistance between the substation grounding and remote earth (see Figure 6). It is defined in [137, 155] as the impedance between a point in the grounding system and the reference earth, which is a far-away specific point in the conductive environment. The neutral point is connected to the substation grounding system and is considered perfectly conductive. The main purpose of the grounding system is:

- *"To provide means to carry electric currents into the earth under normal and fault conditions without exceeding any operating and equipment limits or adversely affecting continuity of service.*

- *To reduce the risk of a person in the vicinity of grounded facilities being exposed to the danger of critical electric shock."* [155]

This is ensured by constructing the grounding system with meshed conductors and, if necessary, some deep rods, depending on fault currents, touch voltages and the soil. The measurement of the grounding resistance is defined in [156]. The measurement frequency is usually unequal to the bulk frequency but in any case AC. There are no successful DC grounding resistance measurements known to the author, therefore the AC grounding resistances are usually used in GIC calculation. Nevertheless, DC grounding measurements are desirable in the future and may lead to new understandings of GICs and their distribution in earth. If there is no data about the grounding resistance available, literature usually suggests a value of 0.2 Ω [89]. This value must be treated with caution, as high soil resistances make grounding systems hard to construct and e.g. [82] reports of grounding resistances of up to 6.35 Ω in some substations in Ireland.

The grounding resistances of substations in Austria are usually measured during commissioning. Unfortunately, the resistances are not known for all substations, especially for substations that were constructed a long time ago. The Austrian transmission system operator provided samples for grounding resistances for substations where also measurement systems are located. The range of these resistances is between 0.037 Ω and 0.3 Ω (personal correspondence of the author) for 220 kV and 380 kV substations, which means the grounding resistance is typically lower than the 0.2 Ω provided in literature.

In modern power system planning, grounding systems are calculated and designed in electromagnetic transient software, however, there are also rule-of-thumb formulas for meshed grounding systems. One of these simple approaches from [157] is shown with (70).

$$R_G = \frac{\rho_E}{2\,D} \tag{70}$$

The area of the meshed substation grounding system is substituted as a circle with diameter D, which has the same area as the substation. The specific earth resistivity $\rho_E$ is given in Ωm and considered homogeneous in the substation and the surrounding area. The area as well as the soil resistivity are also not known for numerous substations. To gather the missing area information, satellite data was used and the area was measured and approximated in open public geo-information platforms. The specific soil resistivity is more difficult to determine, as the range in Austria is between 50 Ωm to 1000 Ωm [158]. Even though there are maps available, that show a lateral distribution of electric resistivity, local variations e.g. changes in the soil during construction, are not available. TABLE 6 shows the measured and with equation (70) approximated grounding resistances for four substations in Austria. It can be seen, that the scale of the measured and approximated values is similar, except for Sub 4.

*TABLE 6: Substation grounding resistances*

| Substation | Measured $R_G$ in Ω | Approximated $R_G$ in Ω |
|---|---|---|
| **SUB 1** | 0.058 | 0.043 |
| **SUB 2** | 0.092 | 0.154 |
| **SUB 3** | 0.08 | 0.126 |
| **SUB 4** | 0.037 | 0.114 |

To analyze the impact of grounding resistance value uncertainty, two simulations are performed. The first one uses the 0.2 Ω from literature for all substation grounding resistances, and the second simulation reduces the grounding resistance to 0.1 Ω. Both simulations are performed with a rotating E-field with a constant magnitude of 1 V/km, however, the magnitude has no impact on the analysis here. Figure 46 shows the maximum occurring transformer

currents $I_T$ for the Austrian transmission grid, sorted by the magnitude. By reducing the grounding resistance, most of the neutral point currents increase, as depicted with the orange bars in Figure 46. The median change of the currents is about 12%. There is no clear correlation between transformer currents and high changes, but depends highly on the connected lines and the E-field direction: The transformer currents are calculated with equation (48) in 2.4.3.2 and are dependent on the transformer branch-node matrix $BNM_{Tra}$ and the nodal voltages $V_N$. The nodal voltage again is calculated with equation (47) and dependent on the driving voltage sources $V_S$ (depends on E-field direction) and the nodal admittance matrix. The change of the transformer currents therefore not only depends on the proportions in the admittance matrix, but also on the nodal voltages which are dependent on the E-field direction.

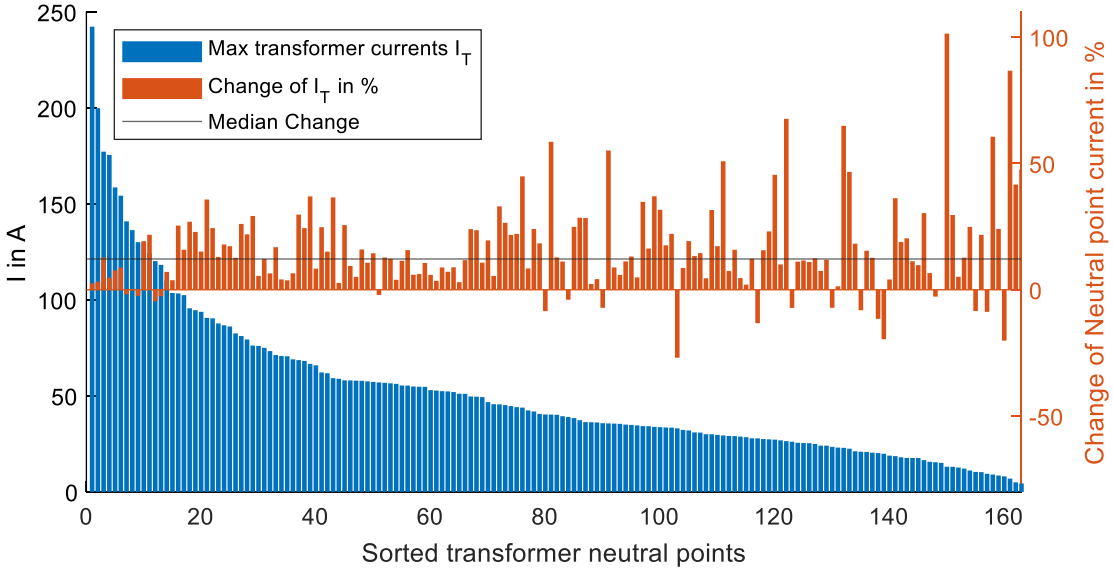


*Figure 46: Maximum transformer currents and percent change after grounding resistance bisection*

In addition to the change of the neutral point current magnitude, also the direction, in which the highest currents occur, is influenced by the unknown grounding resistance. For most transformers (90%), the change of the sensitivity direction $\vartheta$ is below 15°, however, also high changes of up to 50° occur in the two aforementioned simulations, as depicted in Figure 47.

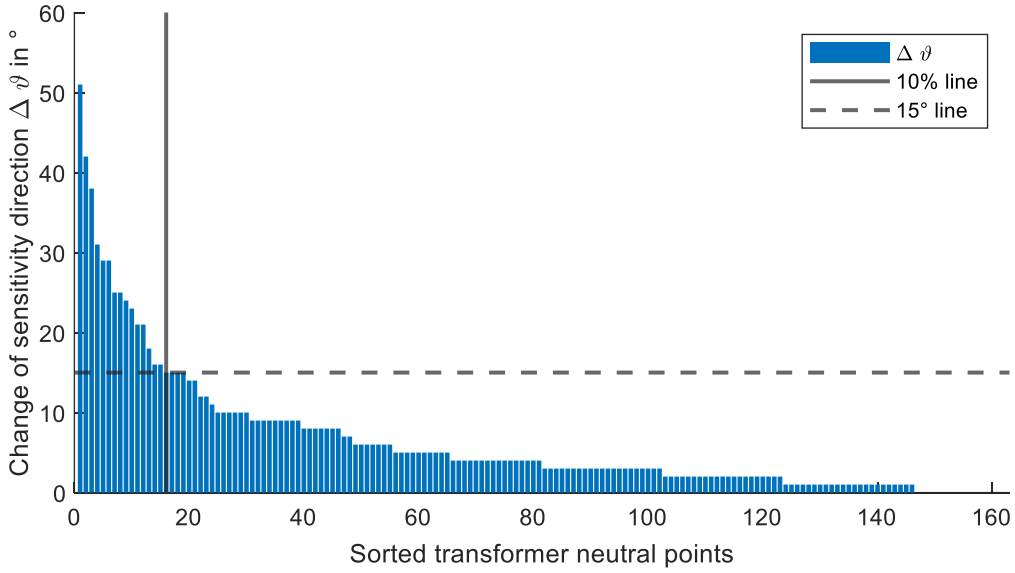


*Figure 47: Change of the angle $\vartheta$ in which the highest currents appear*

This change in the sensitivity direction, together with an uncertainty in electric field predictions, has an influence on a proposed mitigation method in section 7.

**Number and Location of Connected Neutral Points**

The number and place of connected transformer neutral points have, of course, an impact on the calculation of GICs. This chapter will give a brief impression, of why there is an uncertainty possible, especially if the data is gathered from publicly available sites, e.g. open street map, the ENTSO-E website or from the joint allocation office.

The publicly available data usually consists of substations, lines, transformers and sometimes loads and generators. The transformer data, depending on the data source, usually contains nominal power, voltage levels, winding resistances, vector group etc. but no information about the neutral point treatment. The number and location of neutral point connections are dependent on short-circuit restrictions, as the minimal and maximal line-to-ground fault currents are influenced by the zero-sequence of the grid.

According to IEC 60909-0:2016 [159] the line-to-earth fault currents are calculated by:

$$I''_{k1} = \frac{3}{|\underline{Z}_{(1)} + \underline{Z}_{(2)} + \underline{Z}_{(0)}|} \cdot \frac{cU_N}{\sqrt{3}} \tag{71}$$

With $\underline{Z}_{(1)}$ as the positive sequence impedance, $\underline{Z}_{(2)}$ as the negative sequence impedance, $\underline{Z}_{(0)}$ as zero sequence impedance, $U_N$ as nominal voltage and c as the voltage factor. $\underline{Z}_{(0)}$ is usually larger than $\underline{Z}_{(1)}$, which is depending on the neutral point treatment. This means the number of parallel neutral points in a substation has a direct influence on the short-circuit current.

The minimum fault current is needed for fast and reliable detection of the fault and fault location. Only with this information, line tripping and fault clearance is possible. On the other hand, $I_{k1}''$ must be below the maximum short-circuit current, which is responsible for personal safety and the ratings for equipment and assets. The necessary data for this calculation is usually not available in open source datasets and also depending on the data directly from the grid operator, which has uncertainties.

The unknown number and location of grounded transformers therefore have three main impacts:

- The overall resistance of the grid changes if there are more or less parallel transformers grounded, this leads to a different current distribution in the grid.
- If there are fewer transformers grounded than in the GIC calculations, a transformer may be exposed to higher currents than expected.
- A wrong distribution of the currents onto several transformers leads to a wrong calculation of grid-related effects, e.g. reactive power demand or harmonic emissions.

This means the knowledge about the actual connected neutral points and temporary changes of this configuration are essential for accurate GIC calculations.

**Line Connections**

Usually, the transmission grid is operated in complete meshing, meaning that all lines are connected in a substation. However, there are special cases where busbars are split or lines are used as an impedance-increasing element to control load flows. In publicly available grid data, this information is not included, because the data is normally a static model of the grid and the line connections result from operational aspects.

A practical example of this uncertainty was the impedance extension from Tennet to APG, where the 220 kV line from Germany was extended to Tauern and not connected in St. Peter in the first place. This means that LFCs coming in from Germany are forwarded to Tauern before influencing the substation where the line is connected the first time.

### 5.3.3 Reverse Parameter Calculation

This section is based on the author's work in [160].

As described in section 2.4.2, the electric field in the earth's conductive surface can be calculated with a plane wave approach and 1-D earth layer models. Usually, the Earth layer models are either taken from literature, e.g., [61], or gathered via geological surveys. With magnetic field measurements and suitable earth layer models, the induced electric field is calculated with equation (24) (see section 2.4.2 for details).

The calculation of currents in lines, transformers and substation grounding systems is done with nodal analysis [5], described in section 2.4.3.2. The final equation (49) can be rewritten as (72), where the matrix C describes the system network matrix.

$$[\boldsymbol{I}] = [\boldsymbol{C}] \cdot \begin{bmatrix} \boldsymbol{E}_x \\ \boldsymbol{E}_y \end{bmatrix} \tag{72}$$

C consists of the branch-node matrix, network and coupling matrices as well as geographical distances between substations. The current vector in (72) contains all calculated currents in the investigated grid.

As shown in [4], the correlation and the match between simulation and calculation are highly dependent on the used earth layer model. A combination of 1-D earth layers combined with a thin-sheet only leads to minor improvements. If the grid data is perfectly known, the key to better simulation accuracy is a better earth model.

If the electrical grid data is static and considered perfectly known, an inverse calculation of the induced electric field is possible [5]. For this purpose, (72) is transformed into (73).

$$\boldsymbol{E}_{inv} = inv(\boldsymbol{C}_T) \cdot \boldsymbol{I}_{T,meas} \tag{73}$$

The inverse, reduced transformer system network matrix $C_T$ leads in combination with measured currents $I_{T,meas}$ to the inverse calculated electric field $E_{inv}$. The number and selection of currents in the grid have a major influence on the calculation [160]. The electric field needs to be split into north- ($E_x$) and eastward- ($E_y$) components, as the magnetic field is measured in these two directions. Depending on the selected measured transformer currents used as input for the inverse calculation, this leads to different electric fields. The resulting inverse calculated electric fields are those fields, which lead to the measured neutral point currents.

By rearranging (26) and (27) and using the measured magnetic field and the inverse calculated electric field, the calculation of the earth's transfer function $Z_{inv,xy}$ and $Z_{inv,yx}$ is possible with equations (74) and (75).

$$Z_{inv,xy}(\omega) = \mu_0 \cdot \frac{E_{inv,x}(\omega)}{B_y(\omega)} \tag{74}$$

$$Z_{inv,yx}(\omega) = -\mu_0 \cdot \frac{E_{inv,y}(\omega)}{B_x(\omega)} \tag{75}$$

The two inverse calculated transfer functions $Z_{inv,xy}$ and $Z_{inv,yx}$ can now be used as frequency-dependent earth models. As this approach is theoretically possible, it requires perfectly known grid data and exact knowledge about

the different frequency components in the neutral point measurements. If this is not the case, the method may lead to wrong transfer functions and not useful results. As there are still uncertainties in some parts of the grid close to Austria, it is not applicable without large errors.

### 5.3.4 Location of Reference Node

The location of the reference node has no mathematical impact on solving the equations for the network currents itself, as described in 2.4.3.2, but on the distance between any node and the reference point. This introduces changes during the distance determination in equations (43) - (44), which have approximations included, and therefore in the voltage calculation.

To analyze the influence of this error, the reference node was moved from a substation near Vienna in eastern Austria to a substation in the Austrian Alps. For this purpose, two simulations with a rotating electric field are performed and the changes in the maximum transformer currents for these three substations are calculated.

*TABLE 7: Influence of reference node on maximum transformer currents*

| TRANSFORMER AT | CHANGE IN MAX CURRENT |
|---|---|
| **Original Reference Node** | +0.56 % |
| **New Reference Node** | +0.42 % |
| **Most western Substation in Austria** | +0.87% |

TABLE 7 shows the change of the maximum transformer currents in % of the original currents at the respective three nodes. The change for these three samples is below 1%, meaning the current at the original reference node changes by 0.56 % after moving the reference node to the new substation. This means, there is a dependency of the reference node calculable, but in the case of Austria this is negligible. The reason is simply the relatively small size of Austria. However, if larger grids are calculated, e.g. the whole European grid, the influence of the reference node has to be considered.

### 5.3.5 Grid Size

Considerations about the influence of grid size on GIC calculations focus on too small grids or too less included important nodes. This may lead to the known edge effects at the boundaries of the grid, where too large GICs occur because the simulated line ends although the real grid is going onwards. This problem is normally prevented by including at least one additional node (substation) outside the grid of interest. To analyze this, the power grid of Austria is reduced to a relatively small grid in the western part. The grid consists of substation NP08, all connected lines and two further substations connected to these lines. This means a reduction from 870 to 180 nodes, meaning overall 30 substations and transformers and 54 lines from the original 143 substations and 241 lines respectively. The simulation with a rotating electric field leads to maximum changes in 13 line currents, which are connected to the node of interest, between 0 and -6%. Compared to the reduced grid size and the far lower number of nodes, this would be an acceptable tradeoff. However, the transformer neutral current in the substation of interest changes by -22%, which is a change that cannot be ignored. At this point, it is not possible to decide if the calculations are more or less accurate with the reduced grid size, as the change cannot be rated without measurement data. This will be shown and discussed in section 5.4. Nevertheless, this means that, at least in some cases, two additional considered nodes may not be enough for GIC calculations.

### 5.3.6 Shield Wire

The influence of shield wires on GIC calculations was discussed several times in the past. The resistance of shield wires was considered too high compared to line resistances and therefore negligible, which was analytically shown in [161]. However, in [162] it is pointed out that the influence of shield wires on GIC calculations depends on tower footing resistance. An increased line current of +20% was calculated for special cases and asserts the significance of shield wires. The authors of [162] also calculated an equivalent resistance which includes the shield wire and can be connected in parallel with the substation grounding. This reduces the number of new tower nodes drastically. The induced electric field along the line will be neglected for the shield wire influence. In [163], an equivalent voltage source is added to the method of [162]. It is shown, that the shield wire not only increases GICs on long transmission lines but also reduces the currents on short lines.

In contrast to the LP-Method used by [162, 163], the LFC Simulator uses the nodal admittance method (for further details see section 2.4). Figure 48 shows a schematic of a single line between substations A and B and an included shield wire. The shield wire is parallel to the line but split into n segments. After a wire segment i with the resistance $R_{sw,i}$, the wire is grounded at the tower with the grounding resistance $R_{g,Ti}$.

For a first estimation of the influence of the shield wire on GIC calculations, the shield and the towers are added like lines and separate substations as shown in Figure 48. On the one hand, this increases the numbers of nodes and the computational effort is higher, on the other hand, the influence of equivalent resistance estimations is not introduced into the calculation. Typically, the distance between two towers is around 300 meters, therefore the number of towers was derived by the distance in km between two substations, the coordinates of the towers are equally distributed along the line between the substations. The tower resistances are all set to $R_{g,Ti}$ = 5 Ω in the following calculations, but the shield wire resistances $R_{sw}$ are taken from line datasets. The shield wire resistances are typically three to six times higher than the line resistance and not divided by 3, as done for the three phases.

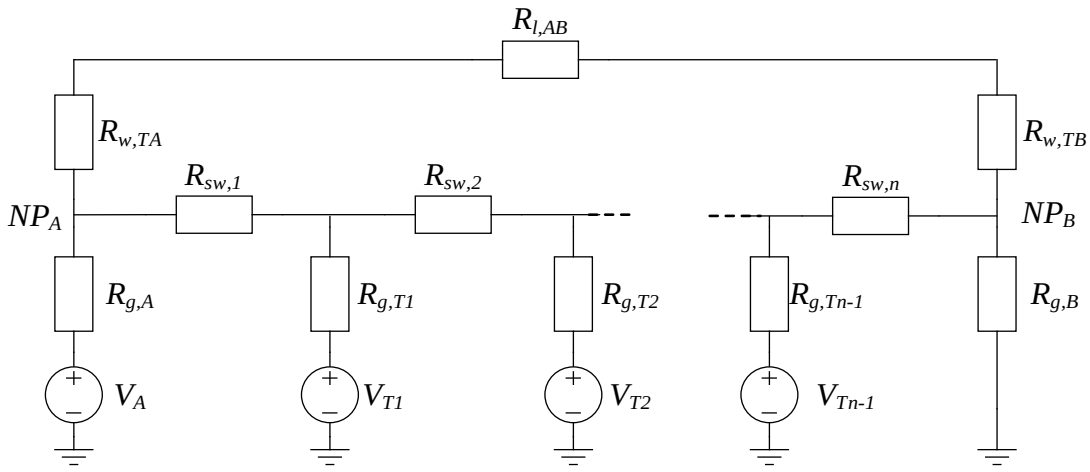


*Figure 48: Single line with shield wire*

The influence of the shield wire is tested on 220 kV lines with a neutral point measurement system nearby. First considerations assume a rotating electric field. The upper plot in Figure 49 shows the transformer current at the measurement station NP08. This transformer is connected to several 220 and 380 kV lines (for details see Figure 11). The two lines in the western direction are mounted on the same towers, which means there is one common shield wire mounted. The lines are approximately 90 km long, resulting in 300 shield wire segments. Also, the two lines in the northern direction are mounted on the same towers for about 80 km, resulting in 273 shield wire segments. The currents in Figure 49 are normalized on the base of the maximum current at this transformer without considering the shield wire. The currents of NP08 are nearly the same and show only an increase in the magnitudes of 0.2% when considering the shield wires.

The second grid element, where the shield wire effect is tested, is at NP08, where on the two lines in the western direction the shield wire is implemented. The length of the line to the next substation is 47 km and consists of 155 shield wire segments. As seen in the lower plot of Figure 49, the currents decrease, as also proposed by [163]. However, the change of the magnitude is only -4.4%, which might be considered a relatively high difference, but section 5.4 will show that this can be neglected without hesitation.

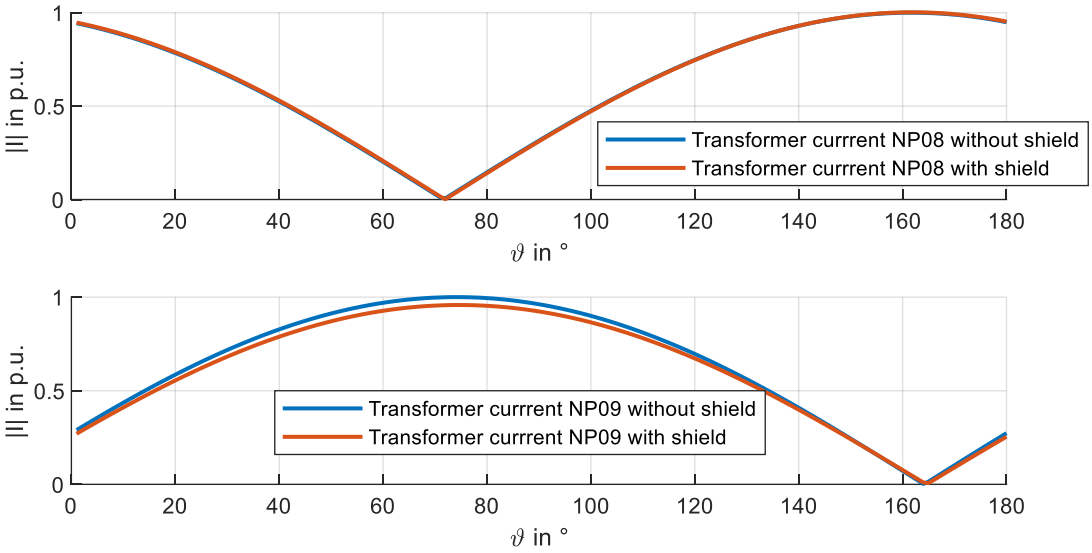


*Figure 49: Comparison of two neutral point currents with and without shield wires*

As described, the shield wires were implemented as lines and the towers as substations. That this is not completely necessary, besides the relatively small changes in neutral currents, can be seen in Figure 50, where the currents in the tower grounding systems are shown for the two implemented shield wires near NP08. The closer the towers are to the substation, the higher the currents in the grounding systems. The different maximum values depend on the grid topology, e.g. the line direction and the substation grounding currents. After several towers, the currents tend to be 0. This shows the applicability of the in [163] proposed equivalent resistance and source. However, due to the already shown relatively small impact, the shield wires can still be neglected in the author's opinion.

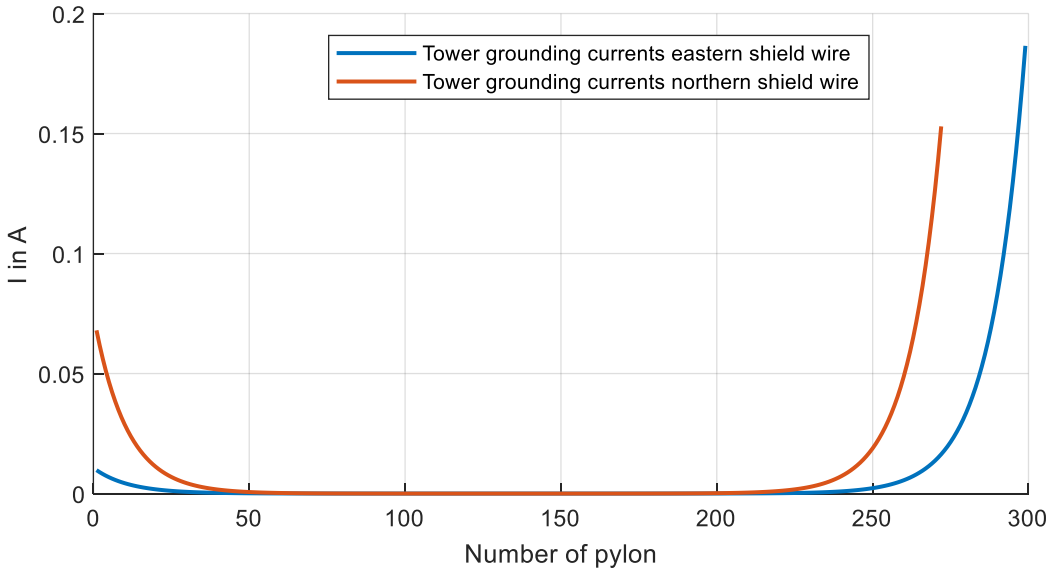


*Figure 50: Currents in the tower grounding systems*

The reason, why exactly these two transformers and the connected lines were investigated can be found in the next

section 5.4, where calculations and measurements are compared.

## 5.4 Verification of Calculations Using Data from the April Storm 2023

The verification of GIC calculations with measurements is an important task to prove the accuracy and to identify problems therein. This is mainly done with measurements during GMDs. On April 23 - 24, 2023, the largest solar storm since the beginning of GIC measurements in Austria hit our Earth. This event is used in the following to compare simulations and measurements of the Austrian power grid.

As already described, the usage of the earth layer model M39 and also M55 led to overall good results. Figure 51 shows the measurements of the seven systems in operation during the GMD impact on Earth as well as the simulations for the respective transformers, calculated with M39. In general, an overestimation of currents is more acceptable than an underestimation, as too low calculated currents would lead to an understated risk of a GMD.

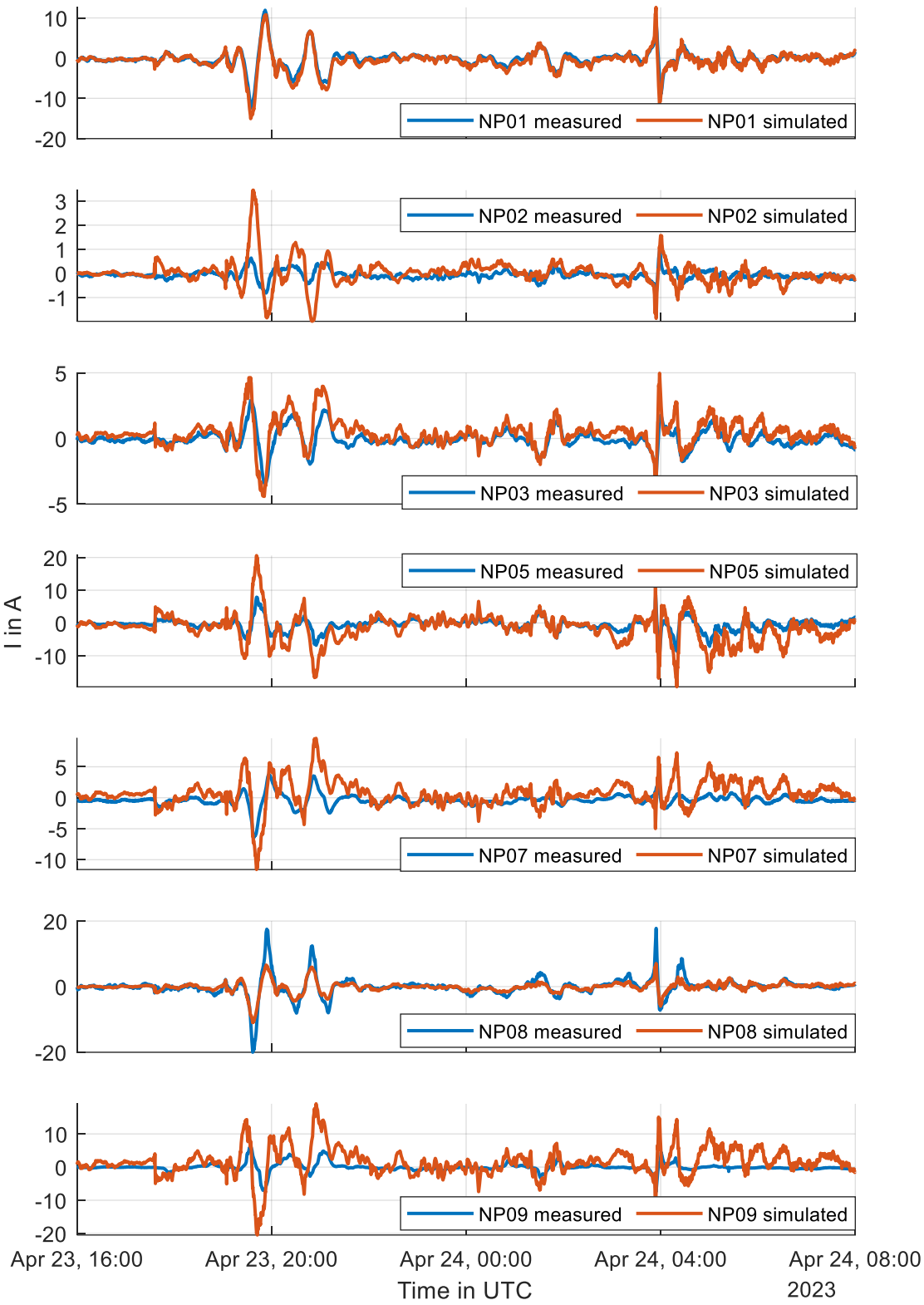


*Figure 51: Measured and simulated currents for the April 2023 solar storm*

*TABLE 8: Goodness of fit parameters for the solar storm of April 2023*

| | NP01 | NP02 | NP03 | NP05 | NP07 | NP08 | NP09 |
|---|---|---|---|---|---|---|---|
| **R** | 0.961 | 0.426 | 0.817 | 0.904 | 0.688 | 0.919 | 0.537 |
| **P** | 0.661 | -1.625 | 0.136 | -0.563 | -0.796 | 0.45 | -1.99 |
| **RMSE** | 0.841 | 0.472 | 0.79 | 2.94 | 1.956 | 1.547 | 4.042 |

The comparison yields ambivalent results:

- Simulation and measurement for NP01 and NP03 fit very well
- Simulation of NP05 and NP07 show the correct time course but are approximated too high
- NP02 and NP09 are both 220 kV neutral points, the simulation results overestimate the measured currents
- Simulations of NP08 are underestimating the measured currents

Simulation and measurement of NP01 show the overall best fit. There are several reasons for this good fit, e.g., the grid around NP01 is very well known. The grid model shows a high degree of accuracy, as no cross-border lines with uncertain parameters are connected in this substation. Additionally, due to the high number of connected lines in all directions, small individual inaccuracies do not have such a high influence on the result.

The simulations for NP05 show the importance of accurate and latest grid data: one of two 380 kV lines connected at the transformers of NP05 was disconnected during the first GMD impact and connected shortly before the second impact. Figure 52 shows three currents: the measured current at NP05, the simulated current without taking the temporary line outage into account and the simulated current with the actual grid. Although both simulated currents show an overestimation, the impact of the line out of service can be clearly seen. This is another indicator of the importance of accurate grid data. The further overestimation, which is visible despite the consideration of the 400 kV line outage, probably results from the cross-country connection to Germany, where detailed grid data is missing.

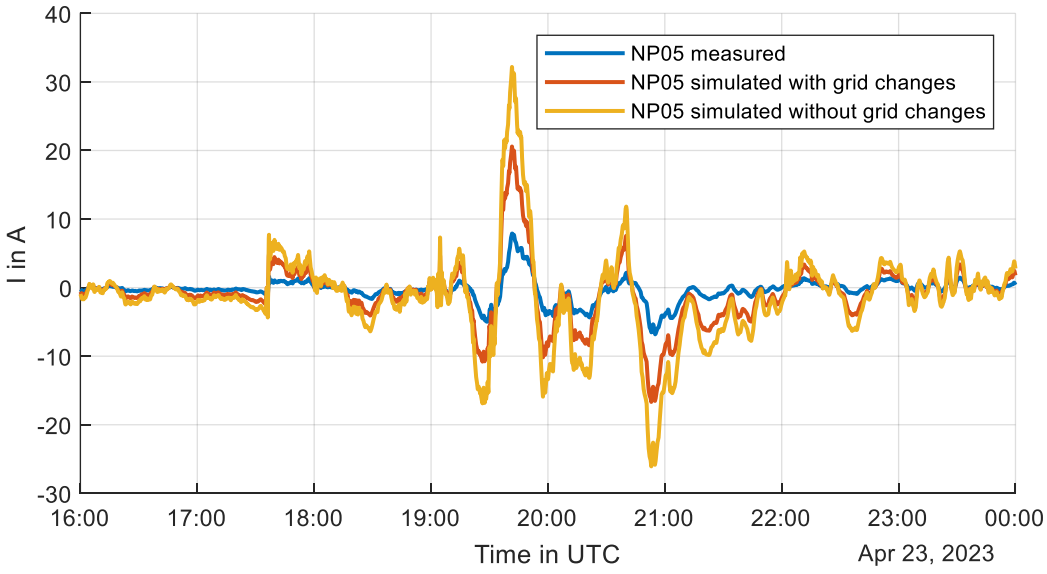


*Figure 52: Comparison of the influence of accurate grid data on measurement vs simulation at NP05*

The investigation of the cause for the high discrepancies between measurement and simulation for NP08 is done in the following:

During the first extrema of the storm, the electric field had a north-west direction. Taking this into account, the resistance in north-western direction seems to be too high. By reducing the resistance of the four connected lines

in this direction by 30%, the negative peak can be approximated much better, as shown in Figure 53. However, the following positive peak is still underestimated. The goal here is not to trim the grid data for a perfect simulation result but to show the influence of different parameters on the grid. The comparison between simulation and measurement at NP08 perfectly shows, that grid data has a major influence on simulation results. In the case of the simulated grid, the information about lines in Austria is good to a certain point of detail, however, cross-border lines, lines and transformers in neighboring countries, number of grounded neutral points, substation grounding resistance etc. are either taken from publicly available sources or estimated. Especially the publicly available datasets are usually (at least at the time of writing in Autumn 2023) of moderately good quality and only show the static grid model, which is usually not up to date. Of course, the calculation of the electric field, and thus the selection of the used earth model, has a major impact on the simulated currents. Although NP08 is situated in the Alps and according to [61] the earth layer model M55 is suitable for this region, Figure 53 shows that the simulated currents with M55 lead even to a further underestimation. Reasonable explanations are the lines to Germany which end in flatland and therefore in a quite different geological area.

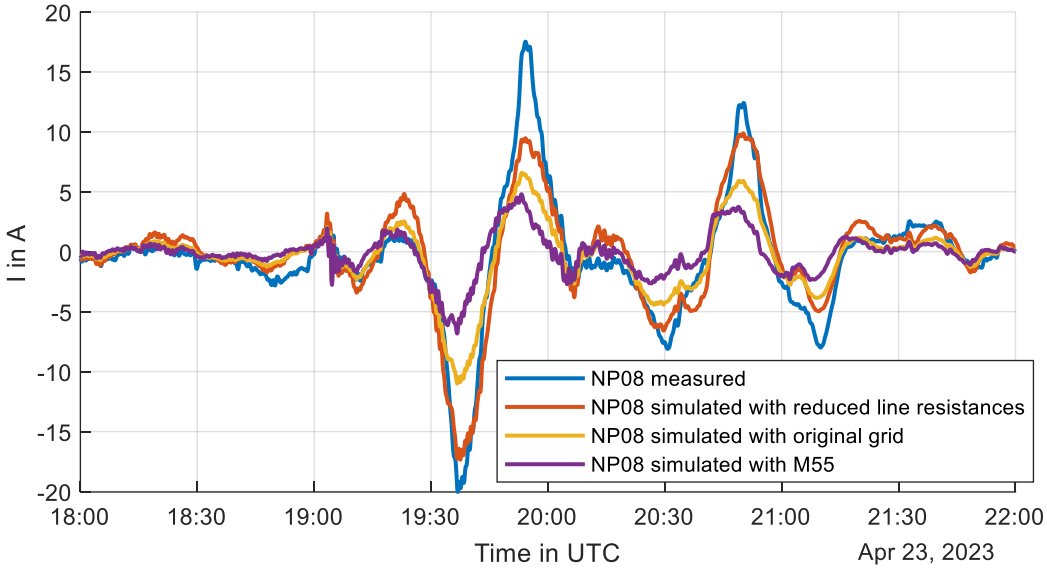


*Figure 53: Measurement and calculations for NP08*

By analyzing this comparison, it is obvious that the effect of shield wires, as described in section 5.3.6, can be neglected as there are by far more serious uncertainties in grid data and earth models.

The grid size and effects of too small grids, briefly discussed in section 5.3.5, influence the simulation accuracy. In the case of NP08, a grid reduction to NP08 plus two nodes in each direction, leads to a further reduction of the already too small calculated peak currents. Regarding the analyzed solar storm, this means a negative peak in the first phase of only -8 A. The time course however is nearly not affected by the grid reduction.

The simulations at NP02 and NP09 are also overestimating the currents in the 220 kV neutral point. This problem is not completely resolved yet. Generally, the accuracy of all 220 kV neutral point simulations is lower than the accuracy of the 380 kV calculations. Possible reasons are uncertainties in the grid data, e.g., not all lines are meshed, or the substation grounding resistances are not correct. However, the error introduced by neglecting the shield wire is not as critical and therefore not considered.

## 5.5 Summary of GIC Calculations

Magnetic field measurements on ground level are the starting point in GIC calculations. There are several observatories around Austria, because of the relatively small size of Austria, the usage of only one observatory is sufficient. It was shown, that the absolute values of the Earth's magnetic field vary between four observatories but the differences in changes in the magnetic field are negligible. This means an interpolation between observatories is not necessary, which simplifies the simulations.

Austria can be described with five different earth layer models from [61]. These models show different conductivities and layer depths for different parts of Austria. As shown in literature, the usage of M39 is the most suitable for Austria.

During a sensitivity analysis, an electric field with a constant magnitude is rotated and applied to GIC calculations. This shows the direction in which the highest currents tend to occur for each line or transformer. Information from these calculations can be used for several analyses, e.g. where are the highest GICs expected to occur, where could new measurement systems be of interest or how future grid expansion influences GICs.

The performance and accuracy of GIC calculations are influenced by several parameters. Of course, the different earth layer models show an impact on GIC simulations, but also unknown grid parameters influence the calculations. One of the most significant, and yet not resolved issues is the substation grounding resistance. In power grids, the substation grounding resistances are measured with AC, leading to an AC resistance. Additionally, not every grounding resistance is known, which makes assumptions necessary. Typically, the resistance is set to 0.2 Ω. It was shown, that this value is too high for the Austrian grid in most cases. A reduction to 0.1 Ω can lead to high changes in transformer current magnitude and sensitivity direction. Therefore, DC grounding resistance measurements would be desirable.

Too small grids have a major influence on GIC simulations. Although it is common practice to include one or two additional nodes, it is, at least for some points, not enough for a high simulation accuracy. This leads to challenges especially for nodes close to borders, as gathering grid data from several countries is a difficult topic.

The effect of shield wires was recently discussed in literature. The analysis done in this work confirmed the principal results in literature, however, the changes in transformer currents in the Austrian transmission grid are negligible.

The solar storm from April 2023 is a interesting case for comparisons between simulations and measurements. Some of the simulated currents show a very good fit, however, there are still discrepancies between simulation and measurement. The major factors for these differences are unknown or wrong grid data, e.g., no information about line outages.

# 6 Effects of LFCs on Power Grids

Neutral point currents lead to several effects in power grids, as described in section 2. This work focuses on the analysis of two effects: The additional reactive power demand and the generation of harmonics. The principal considerations about the implementation of equivalent harmonic current sources for harmonic load flow calculations, representing the effects of transformer core saturation are shown and the effect on voltage harmonics is discussed. Additionally, the used principal calculation method of reactive power under DC bias is shown and the effect on the grid is presented with two scenarios in the Austrian transmission grid.

## 6.1 Harmonic Distortion

The electromagnetic modelling of transformers, leading to a detailed model of the exciting current in dependence on DC-bias, requires information about the construction of the transformer. However, the detailed modelling of transformers is not the focus of this thesis. Therefore, the harmonic emissions, i.e. the harmonic transformer currents, can be taken from literature, e.g., [44, 45], or in the case of this thesis from simulations by the transformer manufacturer, done for the different transformer types in the Austrian transmission grid.

There are different methods to include the harmonic distortion of the magnetizing current due to LFCs in load flow analysis. The first, and most intuitive one, is the implementation of the saturation characteristic into the transformer and connecting LFC sources to the transformer neutral points. With electromagnetic transient (EMT) simulations, the distorted currents are directly calculated for each transformer for each time step of the calculation. This is applicable for single transformers or small grids, however, as soon as a system with several transformers is analyzed, the simulation of a few minutes can take up to hours, as described in [164]. To reduce the simulation time and to be able to do far less time-consuming harmonic load flow analysis, the method described in [165–167] splits load flow and the non-linear saturation analysis. First, a fundamental load flow and GIC calculation is performed, leading to voltage and GICs at each transformer terminal. With this data, a non-linear saturation analysis in time domain is performed, which results in distorted exciting currents. The transformation of the exciting currents from time into frequency domain results in the harmonic spectrum, which can be used (after convergence) for harmonic load flow analysis. Details about the magnetic circuit-solving process can be found in [167]. The harmonic spectrum of the exciting current is then implemented as a current source in a fictitious extra wye-connected winding in the transformer model. Therefore, the harmonics purely act on the transformer magnetization current.

The correct implementation of harmonics, caused by transformer saturation, without a saturation curve is by adding a current source in parallel to the main inductance. However, as most power system software tools are not capable of adding a current source inside an already existing model, an estimating approach is described in the following:

According to the law of induction, (76) describes the voltage $v$ resulting from a change over time in the magnetic flux $\Phi$ time the number of turns $N$. The reformulation of (76) to (77) can be understood as the flux in the transformer is the integral over time of the applied voltage.

$$v = -N \frac{d\Phi}{dt} \tag{76}$$

$$\Phi = -\frac{1}{N} \int v \, dt \tag{77}$$

If the voltage has a cosine form with only one fundamental frequency, as depicted with (78), the integral of (78)

results in (79) and the relation of (80), the magnitude of the flux is proportional to the voltage magnitude, can be formed.

$$v(t) = \hat{V} \cdot \cos(\omega t) \tag{78}$$

$$\Phi(t) = -\frac{\hat{V}}{N\,\omega} \cdot \sin(\omega t) \tag{79}$$

$$|\Phi| \sim |v| \tag{80}$$

If the voltage is a harmonic, as described with (81), the division by the inner derivative of the cosine in (82) leads to the proportional magnitude relations of flux and voltage through the harmonic order *n* in (83).

$$v_n(t) = \widehat{V_n} \cdot \cos(n\omega t) \tag{81}$$

$$\Phi_{\mathrm{n}}(t) = -\frac{\widehat{V_n}}{Nn\omega} \cdot \sin(n\omega t) \tag{82}$$

$$|\Phi_{\mathrm{n}}| \sim |\frac{v_n}{n}| \tag{83}$$

The saturation curve is considered without any hysteresis and described with two slopes, as done in [46, 168]. The linear region up to the saturation flux is described by the impedance $X_h$, the saturation region is described by the air-core inductance $X_{sat}$. Equation (84) describes the magnetizing current $i_m(t)$ in dependency on the flux for the saturated and unsaturated transformer core.

$$i_m(t) = \begin{cases} \dfrac{\Phi(t)}{X_h}, & \Phi(t) < \Phi_{sat} \\ \dfrac{\Phi(t)}{X_h} + \dfrac{\Phi(t) - \Phi_{sat}}{X_{sat}}, & \Phi(t) \geq \Phi_{sat} \end{cases} \tag{84}$$

If the flux $\Phi(t)$ is lower than the saturation flux, the magnetizing current is undistorted.

If LFCs flow through the transformer, a DC-flux is superimposed in the core, leading to offsets and the form in (85):

$$\Phi(t) = \Phi_{AC}(t) + \Phi_{DC} \tag{85}$$

This offset leads to high magnitudes in the magnetizing current as soon as $\Phi(t) \geq \Phi_{sat}$. Figure 54 shows the fluxes and currents, assuming a linear inductance $X_h$ of 100 p.u. and an air-core inductance of 0.4 p.u. The $\Phi_{AC}$ is set to 1 p.u., which is also the end of the linear region ($\Phi_{sat} = 1\,\mathrm{p.u.}$). A DC flux offset of 0.1 p.u. is superimposed. The resulting time course and spectrum are shown in Figure 54.

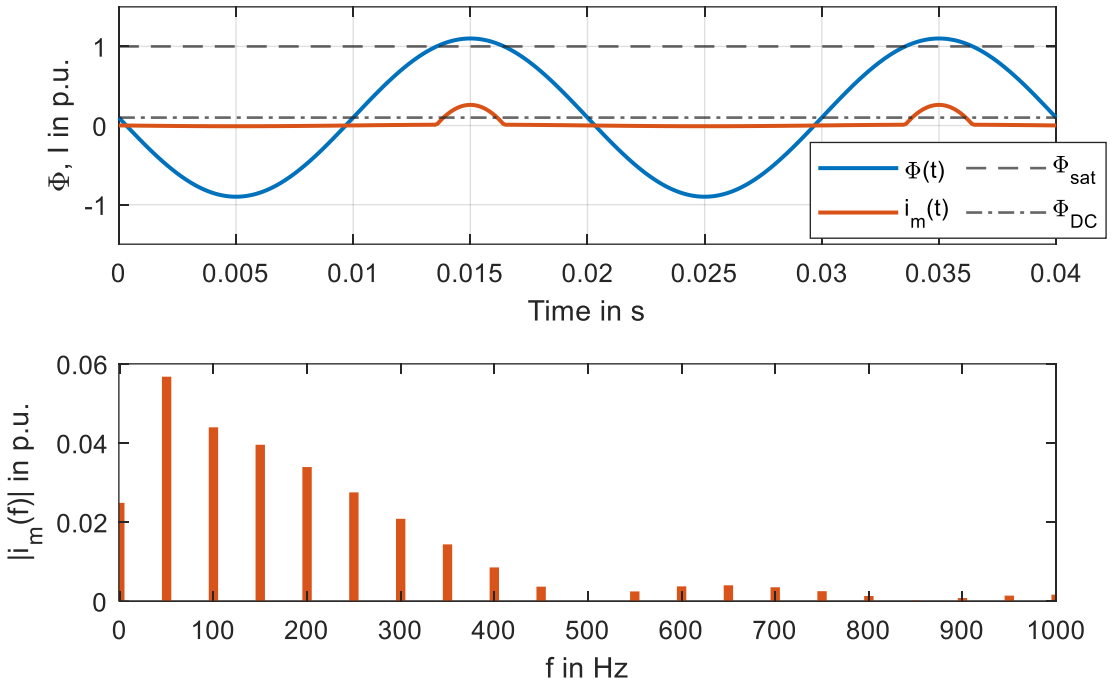


*Figure 54: Flux, magnetizing current and frequency spectra during 0.1 p.u. DC flux*

During these harmonic considerations, it must not be forgotten, that the direction of the DC in the neutral point has an influence on magnetizing current harmonics. This is shown in TABLE 9 for a positive and negative 0.1 p.u. flux in the transformer.

*TABLE 9: Harmonic angles in dependency of DC direction*

| **f in Hz** | | **0** | **50** | **100** | **150** | **200** | **250** | **300** | **350** | **400** |
|---|---|---|---|---|---|---|---|---|---|---|
| **Harmonic angle in °** | Positive DC | 0 | 90 | -180 | -90 | 0 | 90 | -180 | -90 | 0 |
| | Negative DC | 180 | 90 | 0 | -90 | -180 | 90 | 0 | -90 | -180 |

With increasing DC flux, the harmonic also increases, however, as the saturation is non-linear, and in the considered case approximated with a piece-wise linear approach, the increase in the different harmonic components is also non-linear. A closer look at Figure 55 shows, that the fundamental component H1 of the magnetizing current increases with increasing direct flux and has a convex behavior. By plotting H1 over the DC of the magnetizing current H0 in the lower plot, H1 shows a concave form. This different behavior (convex or concave) is caused by the non-linear relation between DC flux and DC magnetizing current, as visible in the upper plot of Figure 55. When $\Phi_{DC}$ is set to 1 p.u., the DC component (H0) only increases to 0.8 p.u. but caused by the far lower air-core inductance the fundamental (H1) increase to 1.25 p.u.. Hence, plotting the higher increase rate of H1 over the lower rate of H0, the behavior is concave. This is especially important during the comparison of results in literature.

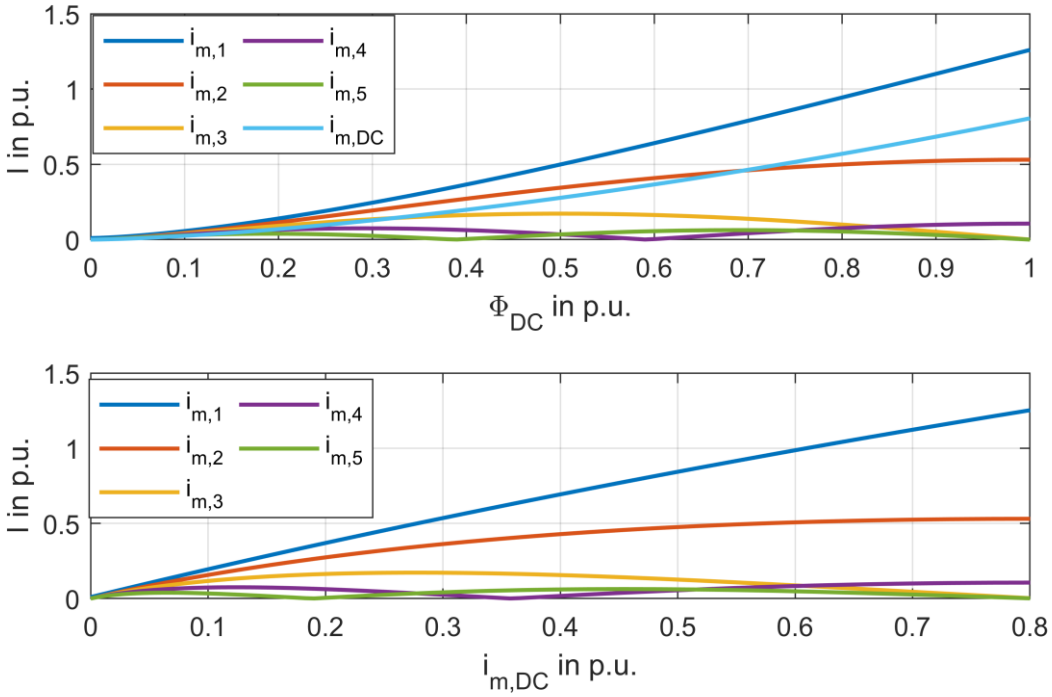


*Figure 55: Harmonics of the magnetizing currents in dependence of the DC flux and DC in magnetizing current*

The results in Figure 55 are calculated under the assumption of an undistorted AC flux respectively an undistorted voltage with constant amplitude at the transformer terminals. However, harmonic currents will cause harmonic distortion in the voltage, which – as well as deviations of the fundamental magnitude - will have feedback on harmonic current generation. As long as the voltage distortion or deviation in magnitude is rather small (i.e. a few percent of the nominal voltage), this effect can be considered in a linearized way. For this purpose, a sensitivity analysis was done. The correlation between harmonic currents and DC was determined for different magnitudes of the fundamental voltage (0.9 to 1.1 p.u.) and different amplitudes of the 2$^{nd}$ harmonic (0 to 0.4 p.u.).

The resulting dependencies on the voltage magnitude are depicted in Figure 56 to Figure 58.

The effect of higher fundamental voltages on the magnetizing current fundamental is, as expected, nearly linear, i.e. $i_{m,1}$ increases without DC by 0.1 p.u. The effect on the second harmonic can be neglected but as the increased fundamental now leads to saturation, not only in one but in both directions, even without DC, H3 increases as soon as the fundamental is larger than 1 p.u.

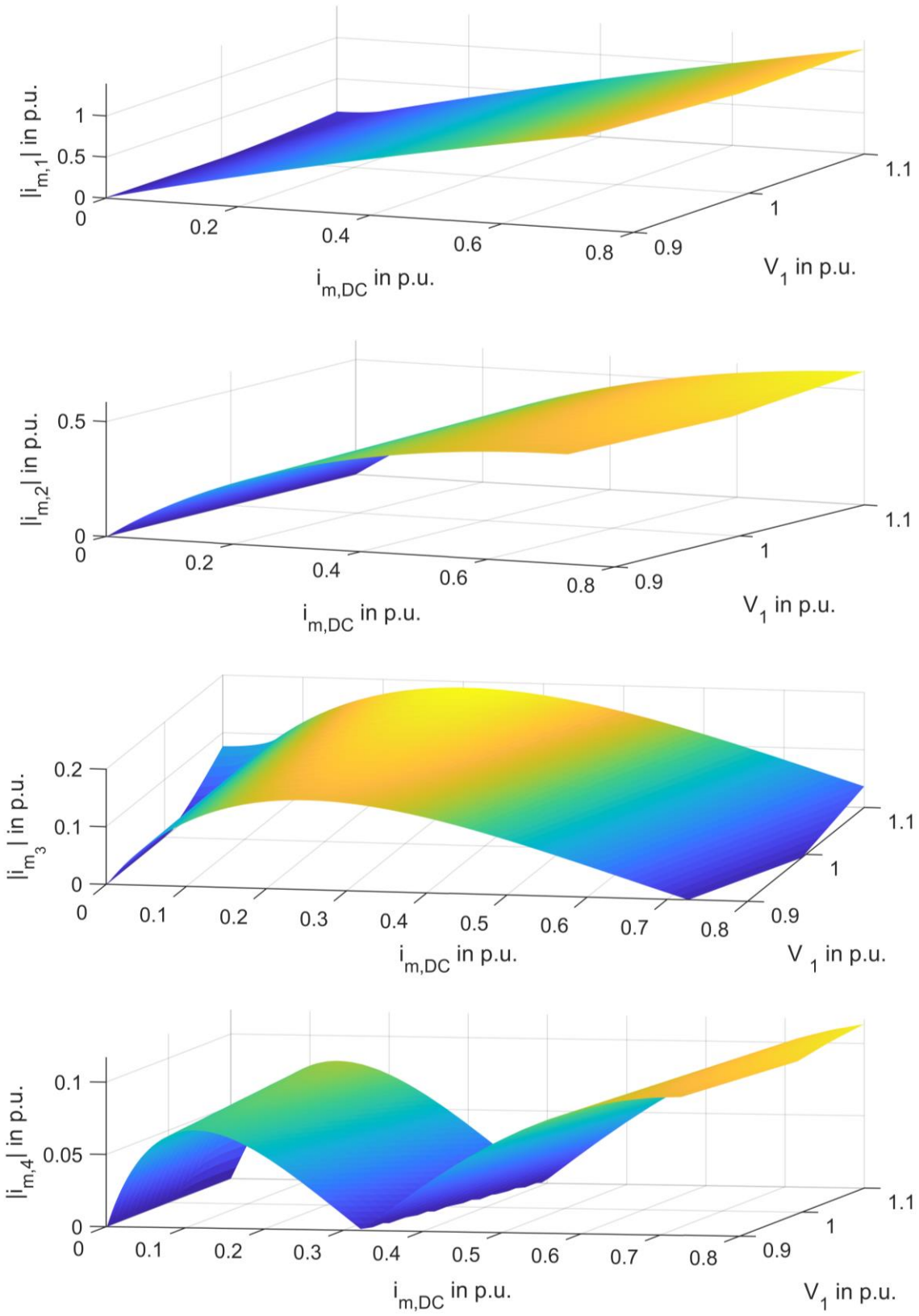


*Figure 56: Relation between harmonics 1-4 in the magnetizing current, DC in magnetizing current and the fundamental voltage amplitude*

The resulting dependencies on the 2nd harmonic in voltage are depicted in Figure 58. To demonstrate the effect, the fundamental voltage is superimposed with a 0.2 p.u. second harmonic in Figure 57. The distortion in the voltage

can be clearly seen, however, as described with equations (82)-(83), the effect in flux, and therefore in the magnetizing current, is reduced.

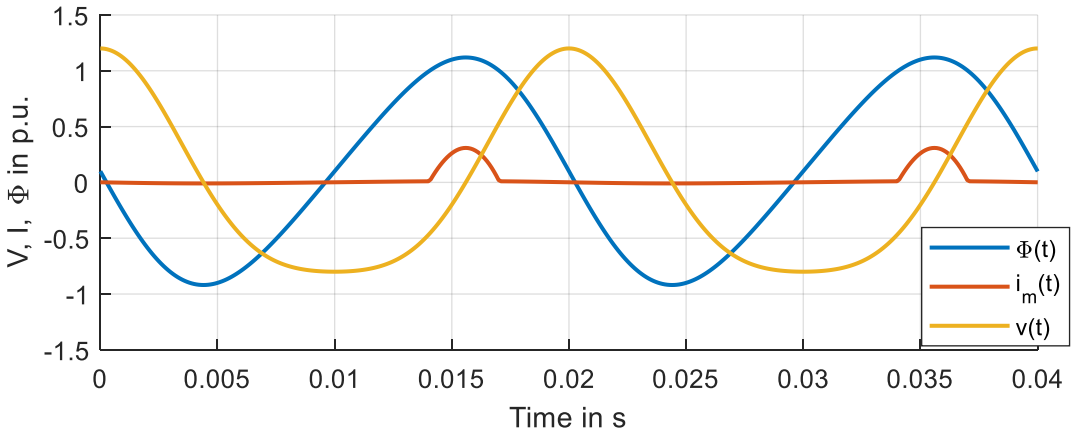


*Figure 57: Distorted voltage, flux and magnetizing current*

The superposition of different DC and harmonic levels in the flux leads to distortions in harmonics, not only in the magnitudes but also in the phase angles. This is depicted for 1st to the 4th harmonic in Figure 58 and Figure 59 (5th to the 8th in the Appendix). The principal relation between DC and current harmonics stays the same with highly increased harmonics in the flux. However, the higher the second harmonic in the flux, the higher stay the currents with increased DC, e.g., 3rd harmonic decreases to 0 at 0.8 p.u. DC and no superimposed second harmonic, but with a 0.2 p.u. second harmonic in the flux, the local minimum is at 0.7 p.u. The angle is not significantly affected by the harmonic distortion of a second harmonic but only by the increasing DC in the magnetizing current. It should be considered, that a 0.2 p.u. second harmonic in the flux means a 0.4 p.u. second harmonic in the terminal voltage and the fundamental voltage was not decreased, therefore it is an extreme and unlike value. Nevertheless, the influence of voltage harmonics on transformer current harmonics is significant. This means that the implementation of a harmonic current source for harmonic load flows without a feedback loop may lead to wrong and unsatisfactory results. The influence on the fundamental and second order harmonic currents is smaller, but they show the highest increase rates when DC flux is applied. Therefore an approximation with a current source is considerable. If higher order harmonics are also approximated, the results, especially the voltage harmonics, must be checked to classify the simulation accuracy.

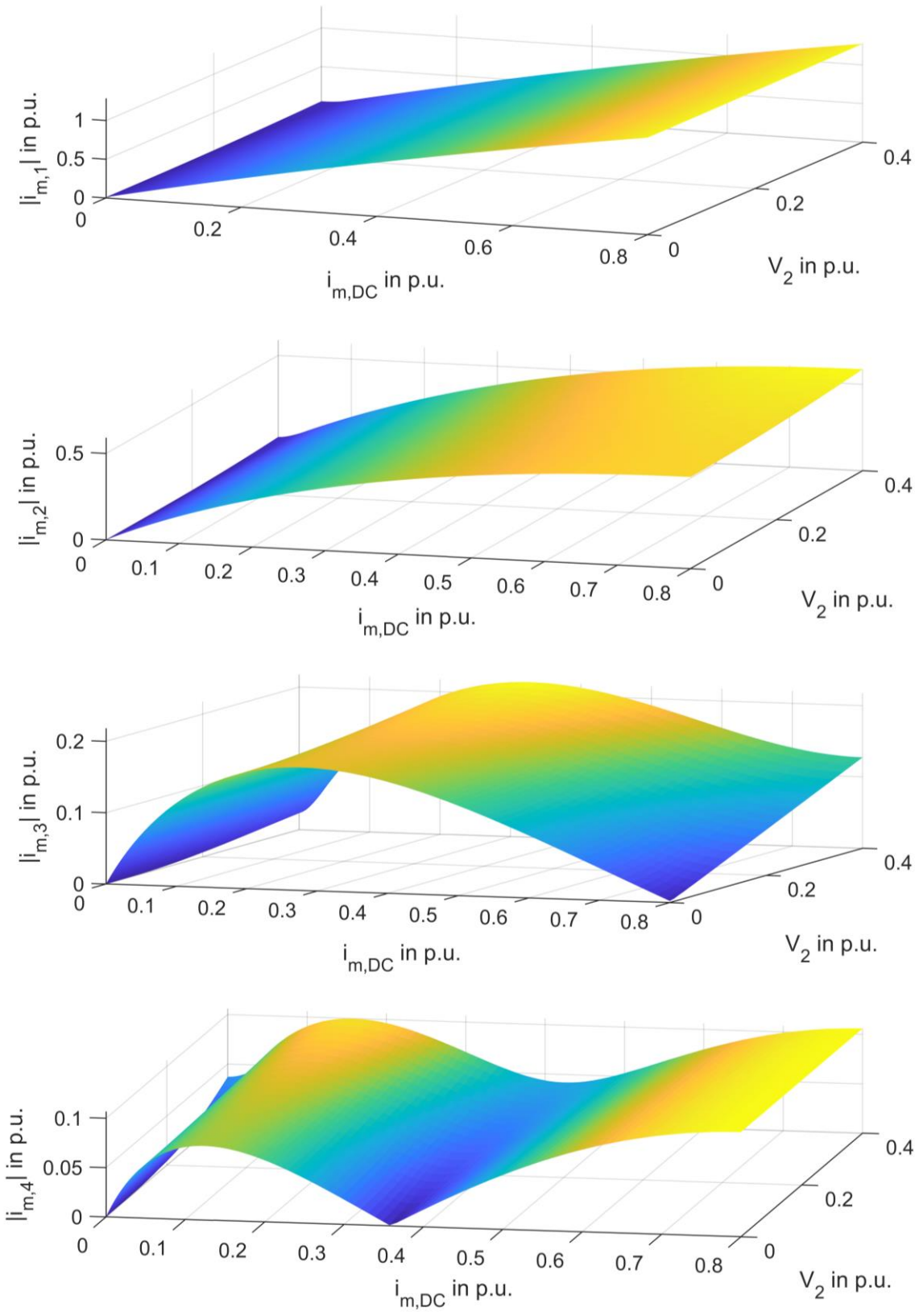


*Figure 58: Relation between harmonics 1-4 in the magnetizing current, DC in magnetizing current and second Harmonic H2 in voltage*

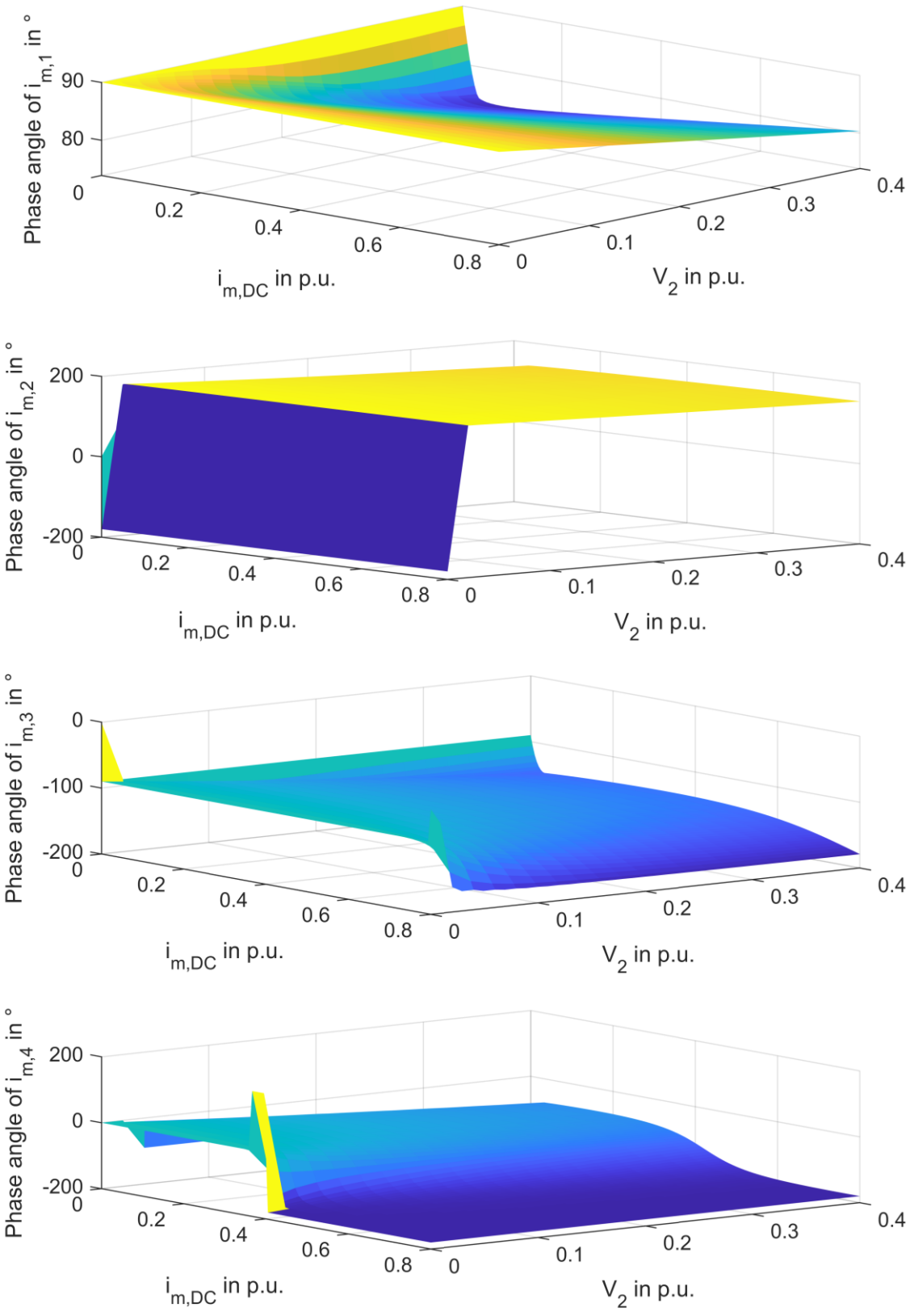


*Figure 59: Relation between harmonics phase angles H1-H4 in the magnetizing current, DC in magnetizing current and second Harmonic H2 in flux*

The implementation of the harmonic current source in the transformer neutral point is not practical because of the following reasons:

- Zero-sequence harmonics from other sources than the transformer would be blocked

- A three-phase harmonic source implementation is not possible in the neutral point
- Adding a DC source would need EMT simulations again

As mentioned above, it is in most power system calculation software not possible to add a current source inside an already existing transformer model. Therefore, instead of implementing the harmonic current source in parallel, to the main inductance of the transformer, which would be the most accurate place, it is placed at the transformer terminal (HV), as depicted in Figure 60. Since $X_{\sigma p}$ and $X_{\sigma s}$ can be neglected compared to Xh (ratio 1 : 100 or higher), the error introduced is probably significantly smaller than the error during the magnitude and angle.

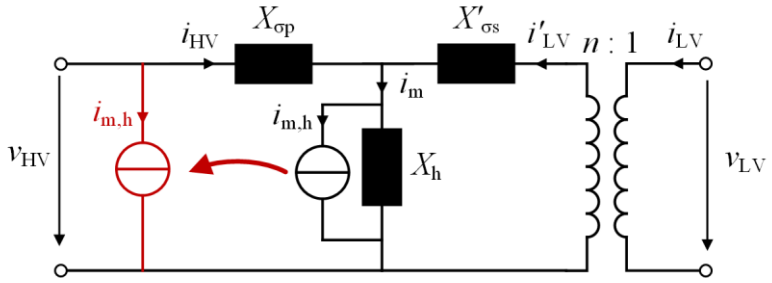


*Figure 60: Transformer schematic with harmonic current sources (resistances and capacitances are neglected)*

To analyze the impact of transformer current harmonics on power grids, the following steps are proposed:

- Collecting data about the harmonic behavior of transformers in the grid
- Performing a GIC calculation with a constant electric field (similar to the angle selection in the following section 6.2.2.1) and determining the DC currents in the transformer neutrals
- Performing an initial harmonic load flow to check if the voltages (fundamental and 2$^{nd}$ harmonic) are within the considered boundaries from above
- Adding a harmonic current source to the terminals of each transformer in the grid (as depicted in Figure 60) using look-up tables
    - As 2$^{nd}$ and 3$^{rd}$ harmonics show the highest magnitudes, it should be suitable to implement only these
- Performing the harmonic load flow iteratively, adjusting the spectrum of the current source
- Checking if the fundamental and 2$^{nd}$ harmonic voltages are within the boundaries of 0.9 to 1.1 p.u. and 0 to 0.2 p.u. respectively

The results of this harmonic analysis can be used to interpret the impact of GICs on e.g., voltage stability or protection devices.

## 6.2 Reactive Power Demand

Besides the harmonic generation of transformers under DC bias, additional reactive power demand, caused by the distorted magnetizing current, can lead to disturbances in the grid.

One of the effects of saturated transformers in power grids is the increased reactive power demand, as described in section 2.3. To analyze this impact, several calculation steps are needed. First of all, standard GIC calculations either with magnetic field data or with a constant electric field are performed. The resulting reactive currents in transformers can afterward be used to calculate an additional reactive power demand for each transformer in the grid. The impact on the grid also depends on the actual loading of the transformer, load flows, reactive power reserves etc. Therefore, the additional reactive power demand is integrated into load flow calculations, which are

done in DigSilent Power Factory where voltage stabilities and limits are analyzed. The split between GIC simulations in the LFC Simulator and the load flow calculations in PowerFactory result from a modular approach, which means no load flow data, scenarios, generators, etc. need to be implemented again in a second tool. This chapter is partly based on the author's work in [169].

### 6.2.1 Transformer Modelling

During the GIC simulation transformer currents are calculated in high- and low-voltage windings if both neutral points are grounded. To calculate the overall reactive power demand of a transformer, and subsequently the reactive power demand of a substation, an effective current $I_{GIC}$ is introduced. According to [91], and also discussed in section 2.4.3.3, this is possible by taking the transformer ratio and transformer type into account. The described transformer equations (51) - (54), taken from [91], always assume, that both neutral points of a transformer are grounded and that GICs flow therefore in both windings. However, in the Austrian transmission grid usually only one side of a transformer is grounded, e. g. if there are two 380/220 kV transformers in a substation, only the 380 kV neutral from the first transformer and the 220 kV neutral from the second transformer are grounded. This is due to protection purposes to limit the line-to-ground fault currents as well as for easier identification of fault locations. This grounding strategy means, that the calculation of the effective current from [91] needs adaptions, otherwise, the resulting DC-flux in the transformers can be underestimated, as the absolute value of sums can be smaller than the sum of absolute values:

$$|a + b| \leq |a| + |b| \tag{86}$$

Three-winding transformers with delta connection of the tertiary winding can be treated as two-winding transformers. The effect of the tertiary winding, which would dampen the effect of rapid DC currents and therefore reduce the reactive power demand, is not considered with this model. Figure 7 in section 2.4.3.3 shows on the left the simplified circuit diagram for two winding transformers. $R_1$ and $R_2$ are the winding resistances of high- and low-voltage sides with the respective number of turns $N_1$ and $N_2$. The tap changer is assumed to be fixed during the simulation, as this would change the effective current during the load flow calculation. However, this could have a positive influence on the voltage stability. The resistance $R_G$ is the substation grounding resistance to remote earth.

$$I_{GIC} = |I_{HV}| + |I_{LV}\frac{n_{LV}}{n_{HV}}| \tag{87}$$

By splitting the absolute value from (52) into (87) for the currents in the high voltage winding $I_{HV}$ and low voltage winding $I_{LV}$, the resulting current is not underestimated if one has a negative sign.

The auto-transformer effective current equation stays the same as in [91] and shown in equation (54), as the grounding topology cannot be changed here.

The effective currents are always positive because the additional reactive power is due to positive or negative half-cycle saturation. The calculated effective currents can now be used in the calculation of additional reactive power demand.

As shown in section 6.1, the increase of the magnetizing current with increasing DC is not linear, also FEM simulation data and past measurements show that the relationship between DC, or generally speaking LFC in the transformer neutral, and the reactive power demand Q of the transformer is not linear. This is due to different saturation behaviors from transformer parts. However, reactive power demand can be approximated using a piecewise, in this case two, linear approach. A schematic representation of this concept is depicted in Figure 61,

where $QSlope_{Low}$ and $QSlope_{High}$ represent the two linear sections with different slopes. $I_{Th}$ is the threshold value to switch between the different slopes. If only one slope is used, either there will be an offset at zero current or there will be an overestimation at higher currents.

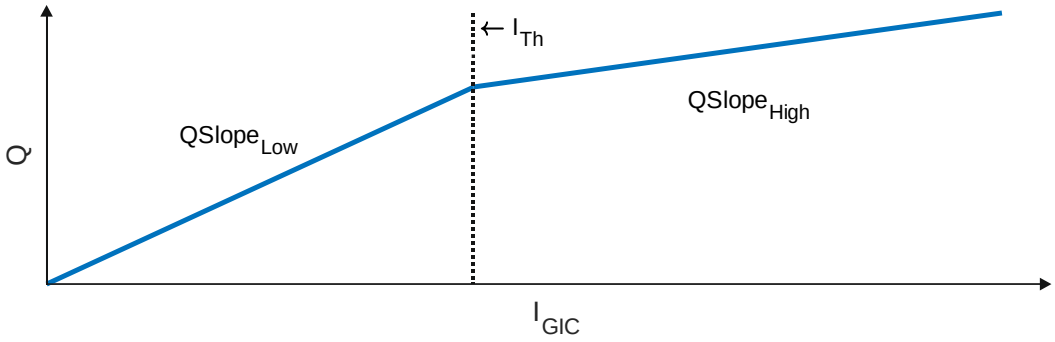


*Figure 61:* Reactive power demand as a function of the effective transformer current (schematic)

Using this approximation, the reactive power demand can be calculated with (88), where $k_1$ is the slope of $QSlope_{Low}$ and $k_2$ is the slope of $QSlope_{High}$. This calculated reactive power only corresponds to additional fundamental reactive power without any harmonics.

$$Q(I_{GIC}) = \begin{cases} k_1 \cdot I_{GIC}, & I_{GIC} \leq I_{Th} \\ k_1 \cdot I_{Th} + k_2 \cdot (I_{GIC} - I_{Th}), & I_{GIC} > I_{Th} \end{cases} \quad (88)$$

For practical application, the parameters $k_1$, $k_2$, and $I_{Th}$ can be determined by computational simulations or calculations [44], through considerations done in section 6.1, or as in this case by the transformer manufacturers.

The results of an exemplary calculation are depicted in Figure 62. For this example, the FEM simulated reactive power demand $Q_{Ref}$ of a real 600 MVA transformer (provided by the transformer manufacturer), which is part of the Austrian transmission grid, is compared with the piecewise linear approach. $I_{GIC}$ is the effective DC neutral point current of the transformer.

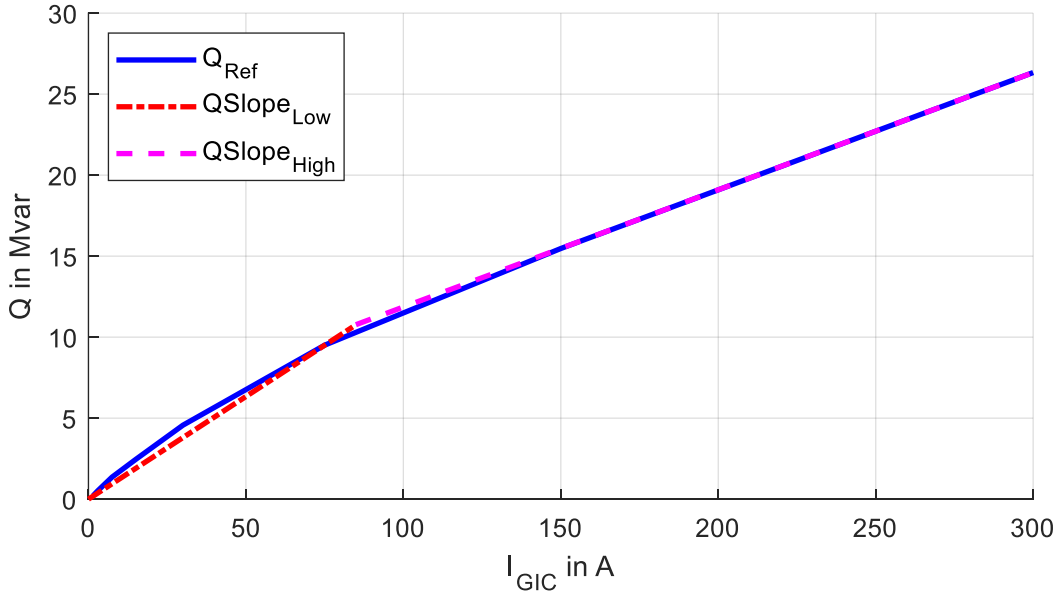


*Figure 62: Reactive power demand of a 600 MVA transformer*

Resulting parameters: $I_{Th}$ = 84.93 A; $k_1$ = 0.1263 Mvar/A; $k_2$ = 0.072 Mvar/A

### 6.2.2 Reactive Power Grid Analysis

To estimate the range of the reactive power demand of the grid under investigation, an electric field *E* with an amplitude of 1 V/km is rotated and applied to the GIC calculation, followed by the presented reactive power calculation. This rotation, as described in Figure 44, leads to different maximum currents in transformers and reveals the sensitivity direction of the transformers and system. At an electric field amplitude of 1 V/km the transformers sensitive in the respective direction usually have reactive power demands above the threshold current from Figure 61. The result is the additional reactive power demand in dependency on the rotating angle $\vartheta$. In Figure 63, the sum of all additional reactive power demands of all transformers in the grid is shown. The maximum occurs at an angle of 60° and 240°. This angle is used in further calculations for the direction of the electric field.

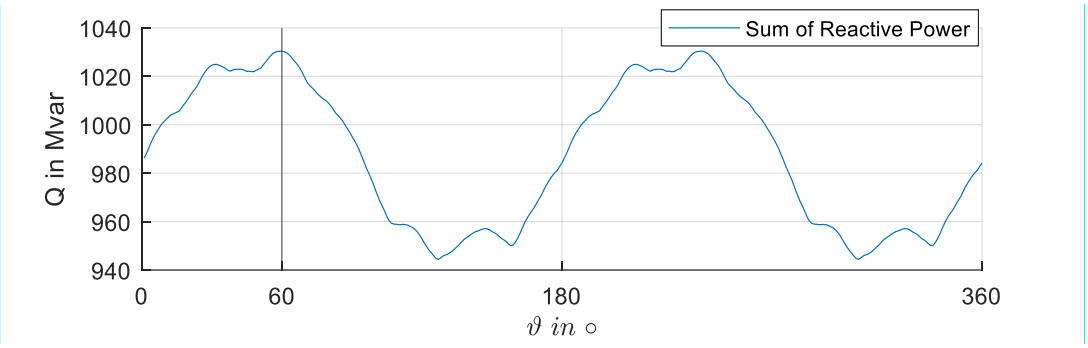


*Figure 63: Sum of additional reactive power demand of the simulated grid*

Typical QV-analysis in power system calculation software shows the influence of reactive power on the voltage at a selected point. This is done by adding a reactive power generator to the power grid and changing its output. The result is the dependency of the voltage on the reactive power from that generator. However, the used power system analysis tool DigSilent PowerFactory is only capable of doing this at only one point per simulation. This would not lead to meaningful results for GIC-Analysis, as the additional reactive power would occur on several transformers at once. Although reactive power needs to be provided locally, close transformers can interact here and this analysis could provide misleading results.

To analyze the impact of additional reactive power of transformers without further transformer modelling and with reasonable effort, reactive power loads were added at busbars with transformers. During load flow analysis, the reactive power loads were increased according to the GIC-simulation results until voltage levels were violated or the load flow calculation did not converge.

#### 6.2.2.1 Scenarios in the Austrian Transmission Grid

Due to the increase in volatile production caused by solar and wind power plants, power transit from Germany to southern European countries leads to high load flows in the Austrian power grid. Especially the 380 kV gap in the Alps is a bottleneck and leads to high stress on the 220 kV lines and limits the trading capacities on the energy market (see market limitations at [170]). As this area is usually under high load, a typical west-east load flow scenario was selected to calculate the influence of additional reactive power demand on voltage and system stability. The electric field in east-northeast direction was increased and the resulting reactive power demand in the load flow analysis was included. It should be stated, that the sum of the reactive power also includes transformers outside of Austria. This is because of the above-mentioned reduction of corner effects, meaning that also transformers, lines and substations outside of Austria are included.

**Scenario 1, medium load flow in normal operation**

In this scenario, a medium load flow from north to south (on the lines in Tyrol from west to east), which leads to no

critical situations or (n-1) violations, is assumed. No lines are under critical load, the voltage is inside the voltage limits. Generators in this area are operated in voltage control mode with 1 % Q-static or with constant reactive power infeed.

Adding a major solar storm with amplitudes of 5 V/km in the before calculated direction of 60° to this scenario, additional reactive power demands rise to 100 Mvar at one transformer. Compared to the rated power of this transformer, this means a higher reactive power demand of 16 %. At the transformers in this selected area, additional reactive power demands of 42 and 47 Mvar respectively, occur. However, as the grid is not heavily loaded, the generators in operation are capable of providing this reactive power and no voltage limits are harmed. Even the voltage at the transformer with the additional 100 Mvar only drops by 5 % and remains within the voltage limits. This means, that for this analyzed scenario, even major solar storms lead to no problems in terms of voltage and reactive power.

**Scenario 2, high load flow with line outage**

The second scenario assumes a high load flow with a critical line outage. Therefore, the remaining lines are under higher loads and are operated above their surge impedance load. This means higher reactive power losses of lines which need to be compensated to stabilize the voltage. Additionally, because of the line outage, this system would not be (n-1) secure.

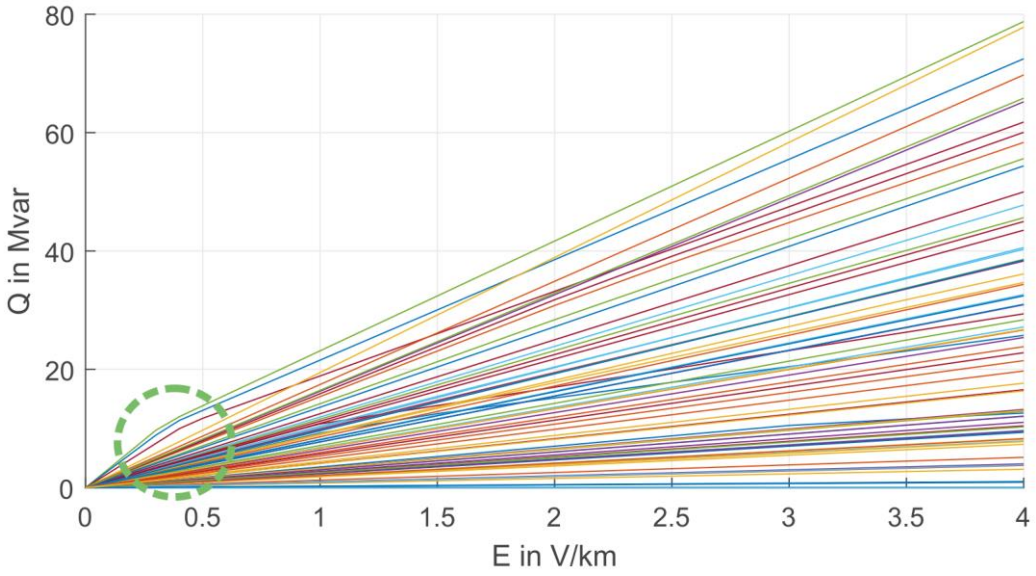


*Figure 64: Reactive power demand of transformers in the investigated grid in dependency on the electric field*

As mentioned above, transformers have different sensitivities to electric field directions, which is caused by the grid topology. This sensitivity can now be seen in Figure 64, as the additional reactive power demand of some transformers rises up to 80 Mvar at the maximum electric field amplitude and some others nearly don't change, as the selected electric field direction does not lead to neutral point currents in these transformers. Additionally, the different slopes and slope changes can be seen, especially at electric field values of 400 mV/km. The voltage in Figure 65 changes accordingly to the reactive power demand, but is damped by the generator control scheme in most cases.

At electric field strengths higher than 4 V/km, the load flow calculation did not converge as some voltages would be too low and harm the voltage band. With only the generators in operation, this would mean voltage problems and severe risks for grid operation.

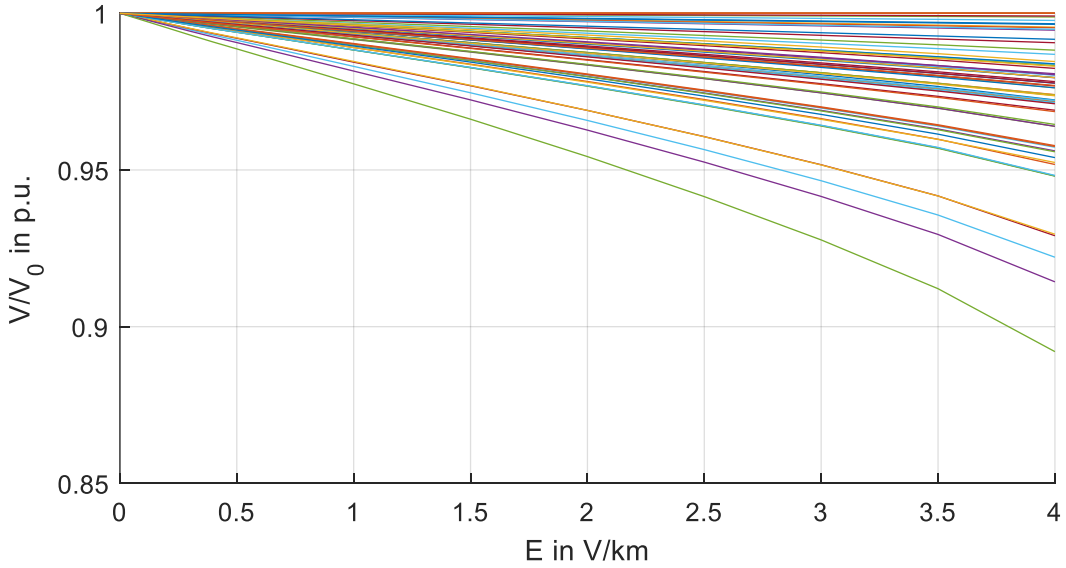


*Figure 65: Voltage drop at bus bars in relation to electric field strengths*

At some of the busbars, however, the voltage does not drop, although the reactive power of connected transformers rises (top lines in Figure 65). This is simply because of simulation preferences: close slack-node or generators in voltage-control mode (inside their operating limits) prevent the voltage from changing.

This scenario shows, that solar storms with induced electric fields of up to 4 V/km lead to no major disturbances in the Austrian grid, but is very close to a major incident. However, this only considers the situation in Austria, meaning the reactive power situation in neighboring countries further than a few nodes is not analyzed. This could only be done with detailed grid data of the whole synchronized zone of the ENTSO-E grid.

There are of course other interesting scenarios: For example, could this grid be tested with another E-field direction, in which the transformers in Austria have the highest additional reactive power demand, and not as shown above, the whole system has the highest demand?

## 6.3 Summary of Grid Impacts

The principal behavior of the magnetizing current of saturated transformers was investigated. For this purpose, an analytical calculation of the distorted magnetizing current was performed and the influence of direct flux and voltage harmonics was analyzed. It is shown, that voltage harmonics influence the magnetizing current, however, as long as the voltage harmonics are within reasonable boundaries, the effect can be neglected. Therefore it is suitable to add a harmonic current source, which describes the transformer saturation behavior, for harmonic load flow analysis. At the end, a procedure for grid analysis is proposed. However, as there are no harmonic measurements of transformers with DC bias in the grid available yet, the analysis is postponed until data is available.

This chapter also presents a reactive power calculation method added to the LFC-simulator program. The additional reactive power demand of transformers is piecewise linearized. The slopes of these linear relations can be obtained from simulations provided by the transformer manufacturer or from literature if no data is available.

A rotating electric field was used to identify the overall worst-case field direction for the investigated grid in terms of additional reactive power. The additional reactive power demand of the transformers was added via loads at the busbars, reducing the effort of detailed transformer modelling and enabling an easy combination of different calculation software.

Two scenarios in different grid situations were analyzed. At medium grid load, even high solar storms do not lead to voltage or reactive power problems hence generators are capable of providing the additional reactive power. In the second scenario, a major solar storm can lead to voltage problems, however, in the analyzed grid are generators in idle mode, which could be activated in a short time and provide additional reactive power. It is important to mention, that the induced electric fields may not lead to problems within this grid, however, geomagnetic disturbances are never only a national issue. Especially in the interconnected European grid, national voltage problems or outages always influence other grids as well. This means, that e.g. a GIC-related transformer outage in a neighboring country will influence the system security in Austria as well.

The analyzed scenarios are special cases, where the additional reactive power does not lead to voltage problems. However, depending on the electric field direction, grid situation or load scenario, reactive power demand needs to be analyzed specially for each situation.

Some transformers in the Austrian power grid are equipped with a direct current compensation system, which reduces the influence of neutral point currents. This compensation may have a positive influence on the reactive power demand, however, this reduction method was not considered in these scenarios.

# 7 Method for Minimizing the Impact of GICs

This chapter is based on the author's work in [171].

## 7.1 Description of the Proposed Method

The AC transmission grid in Europe with 220 kV and 380 kV voltage levels is solidly grounded. The reasons are e.g. fast detection of phase-to-ground faults, fast fault clearing times and preventing overvoltage during faults. However, not every transformer neutral point is connected. The number of connected transformer neutral points is determined by the minimum and maximum single phase-to-ground fault currents. The minimal current is needed for a safe and reliable fault detection and fault clearance. The maximum fault currents must stay within limits of the short circuit current ratings of all assets in the grid and prevent damage to assets and extreme touch-voltages. This leads in the Austrian transmission system to the commonly applied rule that only one neutral point per voltage level is grounded in a substation. If there are two 380/220 kV transformers operating in parallel in one substation, the 380 kV neutral point of one transformer and the 220 kV neutral point of the other transformer are solidly grounded. This also prevents the transfer of a zero sequence system through the transformer from one voltage level to another. This leaves a certain degree of freedom for changing the earthing configuration during a solar storm temporarily to minimize the impact on the grid. The proposed GIC mitigation method uses these available neutral points to distribute the currents on more transformers, thereby reducing the GIC load on single transformers. To find the best neutral point configuration, an optimization problem is formulated and solved.

Before an objective function can be formulated, a goal of the mitigation approach must be defined. A possible mitigation approach would be to reduce the maximum transformer current in the grid or to reduce GICs at transformers that are more vulnerable to DC neutral currents.

In the proposed method, the goal is to minimize the overall GIC impact on the grid.

$$minimize \sum_{n=1}^{N_T} \mathbf{I}_{Tn}^2(\mathbf{np}) \tag{89}$$

The objective function in (89) minimizes the sum of all squared transformer currents $I_{Tn}$. The currents are expressed in p.u. of the nominal phase current, thus considering the rating of the transformer. In (89), *n* is the transformer index and *np* describes the actual neutral point status (open or closed). The actual transformer currents depend on both the electric field (magnitude and orientation) and the grid topology. As the electric field is held constant during the optimization and only the neutral point connections in the grid are changed, the transformer currents are only dependent on the optimization variable *np.* If the electric field changes, the optimization must be done again. The relation between transformer currents and neutral point connections is complex: An additional parallel transformer means a split of the transformer currents on the one hand; on the other hand, the parallel resistance reduces the overall resistance of the grid, and resistance ratios, meaning that one parallel path does not lead to an exact 50% reduction.

According to Kirchhoff's law, the total sum of all transformer currents in the simulated grid is zero. Therefore, only the sum of absolute currents or the squared currents can be minimized. Because of the squaring in the objective function, higher currents are more penalized than lower currents. Therefore, a maximum current reduction is indirectly included.

The optimization variable and constraints that need to be taken into account are the following:

As described in (90), the optimization variable *np* is a binary vector with the size $N_N \times 1$, where $N_N$ is the number of disposable neutral points in the grid, and defines whether a neutral point *i* is connected ($np_i = 1$) to the ground or if it is open($np_i = 0$).

$$np_i \in \{0,1\}, i = 1, \dots, N_N \tag{90}$$

The neutral point connection vector *np* is added to the GIC calculation described in 2.4.3.2 by multiplication with the winding conductance of the related transformer in the branch-node matrix.

From a grid operator's point of view, only a limited number of changes in the grid topology are applicable in practice. To limit the number of allowed changes, this constraint is mathematically introduced with (91). This constraint compares the original neutral point connection vector $np_0$ with the optimization variable $np$ through an exclusive 'or' ($\oplus$) and calculates the sum. The sum must be lower or equal to an arbitrarily defined number of allowed switching actions $npc_{max}$.

$$\sum_{n=1}^{N_N} (np_{0i} \oplus np_i) \leq npc_{max} \tag{91}$$

The objective function minimizes the overall impact on the grid. To limit the maximum current of individual transformers, constraint (92) is introduced. The maximum current $I_{T,max}$ can be either set as a global maximum for all transformers or as an individual maximum of each transformer. With individual limits, different transformer core types can be taken into account and particular attention to vulnerable types can be paid. More details on transformer current limits to prevent hot spots, harmonic emissions or reactive power demand can be found in the literature, e.g., [50, 168].

$$|I_{Tn}| \leq I_{T,max}, \qquad n = 1, \dots, N_T \tag{92}$$

As mentioned above, it is mandatory to have at least one neutral point per substation and voltage level connected to the ground. This can be accomplished in several ways, such as implementing a constraint for each substation that examines each neutral connection or various summation techniques. In this work, constraint (93) is introduced, which compares the sum and the RMS sum of the difference between the substation connection matrix $SC_{xV}$ (which is calculated with (94)) and the minimum connection matrix $MC_{xV}$.

$$\sum (\mathbf{SC}_{xV} - \mathbf{MC}_{xV}) \geq \sum \sqrt{(\mathbf{SC}_{xV} - \mathbf{MC}_{xV})^2}$$
$$xV \in \{HV, LV\} \tag{93}$$

The minimum connection matrices $MC_{xV}$ with the size $N_S \times 1$, where $N_S$ is the number of substations, contain the minimum neutral point connections per substation and voltage level. The items are zero or positive integers. These matrices indirectly include the constraint, that due to their design and way of operation, neutral points of autotransformers have to be connected to ground. Therefore, if there are two parallel autotransformers in a substation, the corresponding value in the $MC_{xV}$ matrix would be 2.

By subtracting the minimum connection matrix $MC_{xV}$ from $SC_{xV}$, the elements of the resulting vector depict if there are enough neutral points in a substation connected. As the sums of $SC_{xV}$ and $MC_{xV}$ can be equal, although not all necessary neutral points are connected, the comparison with the RMS value in (93) is needed. If there are fewer than required neutral points connected in a substation, a negative value occurs in the resulting vector of $\mathbf{SC}_{xV} - \mathbf{MC}_{xV}$, meaning that the right side of the equation is higher and the constraint is not fulfilled.

For a simple example, assume a grid with two substations A and B. The minimum connection matrix is $MC_{HV} = (2\ 1)^T$ with 2 required neutral points in substation A and 1 in substation B. Assume further, that the optimization would lead to the optimum substation connection matrix $SC_{HV} = (1\ 2)^T$. There are fewer neutral points connected in substation A than required. This can be prevented during the optimization with constraint (93), as the left side of the equation is smaller than the right side and therefore not feasible.

For this approach, two further equations (94) and (95) are needed: The items in the substation connection matrix $SC_{xV}$, calculated with (94) show how many neutral points are connected in every substation. The allocation matrix $A_{xV}$ links the neutral points with substations and voltage levels. The index HV or LV depicts the corresponding voltage level. The element of $A_{HV}(i,j)$ is 1 if the neutral point i is situated in substation j. The size of $A_{xV}$ is $N_N \times N_S$, where $N_N$ is the overall number of available neutral points and $N_S$ is the number of substations.

$$\mathbf{SC}_{xV} = (\mathbf{np}^T \cdot \mathbf{A}_{xV})^T \circ \mathbf{BMC}_{xV}, \qquad xV \in \{HV, LV\} \tag{94}$$

The matrix $BMC_{xV}$ is the Boolean minimum connection matrix with the size $N_s \times 1$, which depicts if there needs to be a neutral connection in a substation and is calculated with (95).

$$BMC_{xV,j} = \begin{cases} 1, & MC_{xV,j} > 0 \\ 0, & MC_{xV,j} = 0 \end{cases}, \qquad xV \in \{HV, LV\}, j = 1, \dots, N_s \tag{95}$$

The multiplication of $np^T$ with $A_{xV}$ creates a vector of the size $1 \times N_S$, which contains the connected neutral points per substation. The element-wise product of the transposed vector with the $BMC_{xV}$ matrix neglects all non-mandatory neutral connections.

The result of this optimization problem is an optimum neutral point connection set for the grid under investigation. As the neutral point configuration has a direct influence on the magnitude of line-to-ground fault currents, short circuit calculations are needed to check for minimum and maximum fault currents. As the mitigation approach follows a modular approach, this is done outside the LFC-simulator in other power calculation software used by the grid operator. Some of the proposed changes in the grid topology may not be feasible due to the aforementioned restrictions Therefore the optimization also generates alternative solutions close to the optimum.

The formulation of this problem shows that, due to the inverse admittance matrix used by the GIC calculation (see chapter 2.4.3), it is a mixed integer, nonlinear problem. To solve this optimization problem, a genetic algorithm is used. Genetic algorithms, developed by [172], are based on the mechanics of natural selection, starting with an initial population and changing it through crossover and mutation into a new generation [173]. Especially in complex problems or problems with several local optima, these stochastic search algorithms provide good results [174]. In the described problem, the initial population is the original neutral point connection vector $np_0$. The used genetic algorithm solves this problem with an Augmented Lagrangian Algorithm. The usage of other solvers is, of course, possible, however, as this work describes the principal idea of a neutral point optimization, the focus is not on different solvers or runtimes, but on the possibility of solving this with a genetic algorithm. Further research may point out the benefits of different solvers or algorithms. The used parameters for the prototype genetic algorithm are: population size = 500, crossover fraction = 0.5 and elite count = 0.05 times population size. As mentioned for the solver, again, these parameters were chosen to work fine for the test grid. A general formulation of the parameter settings is under investigation and further research may lead to better suiting preferences.

### 7.1.1 Description of the Test Grid

The proposed mitigation algorithm has been tested on the GIC-test grid from [89]. It consists of 8 substations, connected with 500 kV and 345 kV lines, 15 transformers and 19 transformer neutral points. Originally, all neutral points are connected to the ground. As described in Section 7.1, usually only one neutral point per voltage level

and substation is grounded. Additionally, the neutral points of auto-transformers are always connected. Applied to the benchmark grid in Figure 66, this leads to the ground-connected neutral points marked in blue.

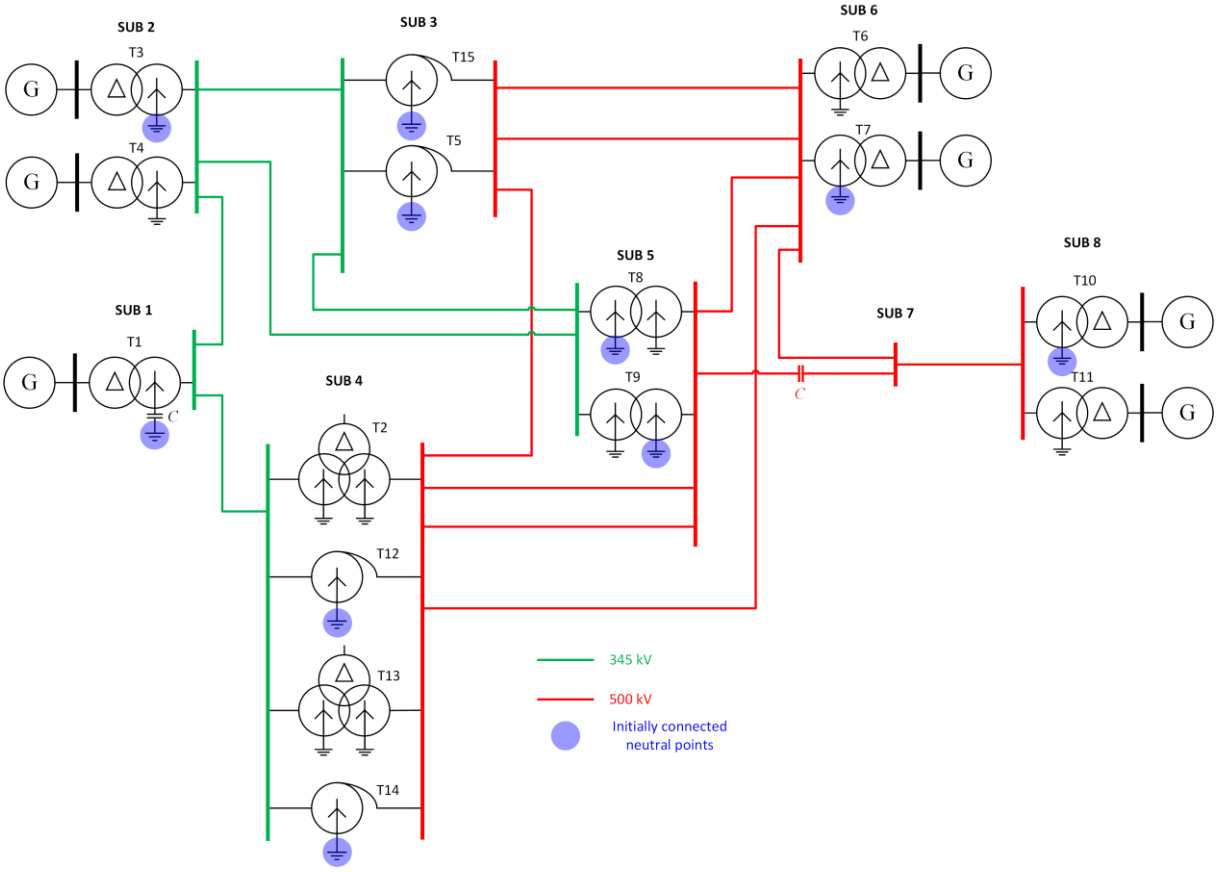


*Figure 66: Benchmark grid adapted from [89]. Connected neutral points are marked blue; all other neutral points are available for the mitigation algorithm*

As there is no detailed data about the rated power, nor the number of limbs of the transformers in the grid given, all generator step-up transformers are assumed to be the same type with a rated power of 600 MVA and all other transformers have the same rated power of 1000 MVA.

Upon first consideration, a constant electric field with $E_x = 1\,\frac{V}{km}$ and $E_y = 1\,\frac{V}{km}$ is applied to the grid. Transformed into a polar coordinate system in Figure 44, this refers to an angle of $\vartheta = 45°$.

### 7.1.2 Influence of Neutral Point Changes

The result of the objective function highly depends on the number of allowed neutral point changes $npc_{max}$ in the optimization variable $np$. The optimum result of one neutral point change ($npc_{max} = 1$) is shown in orange and two neutral point changes ($npc_{max} = 2$) in yellow in Figure 67. The shown transformer currents are calculated in p.u. of the rated current. The newly connected neutral point is $T6_{HV}$ in substation 6, which operates in parallel to transformer T7.

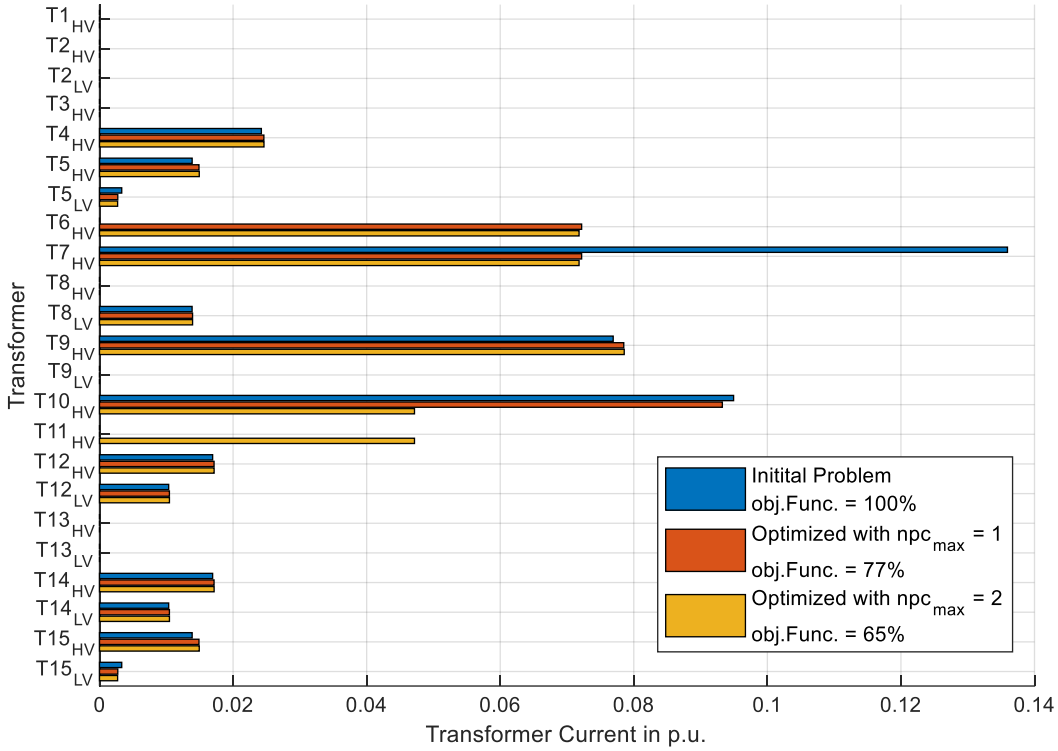


*Figure 67: Transformer currents of original and optimized neutral point configuration.*

As several transformer neutral points are not connected, currents in the respective transformer's windings are zero, e.g., $T2_{HV}$. Although the neutral point of T1 in substation 1 is connected, there is no current flowing through this transformer, as a GIC blocking device is installed there.

As mentioned beforehand, splitting the neutral current of one transformer onto two parallel transformers does not reduce the load by half on a single transformer, as the overall resistance ratios between parallel paths in the grid are changed. Therefore, also the current in T10 is slightly reduced. The reduction of the overall resistance in the grid and the different distribution of currents lead to a slightly higher current in transformer $T9_{HV}$. However, with the objective function chosen in equation (89), a clear reduction of the GIC load on the grid is possible. Additionally, the high current of transformer T7 is effectively reduced with simply one additional neutral point connection.

The additional connection of neutral points reduces the transformer zero-sequence for phase-to-ground faults and the short-circuit currents increase. Therefore, short-circuit calculations need to be performed and short-circuit current ratings must be checked. A possible result of this short-circuit calculation may be, that the optimum neutral point change is not applicable. To overcome this problem, the optimization algorithm is performed several times and the resulting optimal neutral point change is forbidden in the next iteration. The results of the optimization cycle are depicted in Figure 68. The optimal solution would be the connection of $T6_{HV}$, where the objective function is reduced to a value lower than 80 % of the initial problem. However, if this led to inadmissible short circuit currents, another, less effective solution would be the connection of $T11_{HV}$. The five alternative solutions in Figure 68 with the related objective function results show that at a certain point, alternative solutions lead to no improvement. In this case, this starts with alternative three, the connection of $T3_{HV}$. The reason is that the highest currents of $T7_{HV}$, $T9_{HV}$ and $T10_{HV}$ can only be reduced effectively with a parallel connected neutral point and transformer.

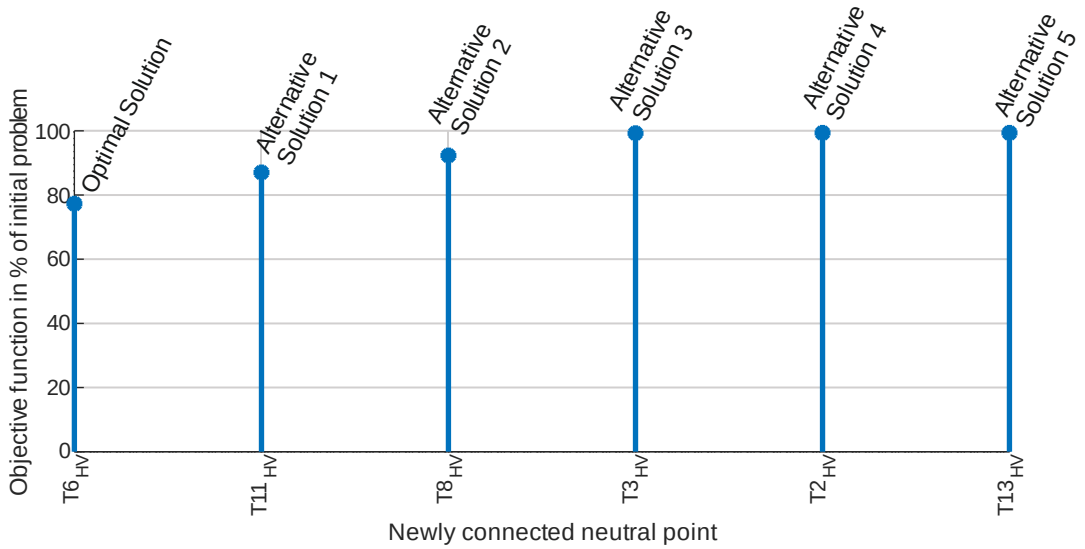


*Figure 68: Ranking of different optimization results.*

In theory, it can be expected that the connection of all available neutral points may lead to the overall lowest objective function value, however, this would violate the given constraints, e.g. maximum short-circuit faults. A similar satisfying result may also be possible with fewer neutral point changes. This would also mean less effort for grid operators while making the mitigation approach more applicable.

This is proven by the results in Figure 69. The increase of constraint (91) up to three allowed neutral point changes leads to a result close to the overall optimal solution and the highest currents in the grid are effectively reduced. Additional connections only lead to minor improvements but increase grid operators' operational expenses.

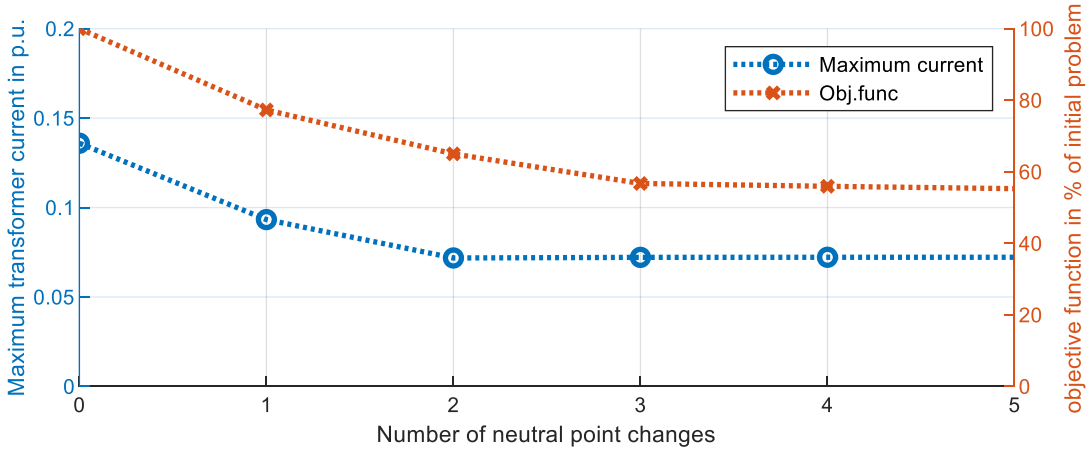


*Figure 69: Ranking of multiple neutral point changes*

It bears mentioning that the maximum transformer current as shown in Figure 69 occurs on different transformers for different numbers of neutral point changes: In the initial problem, it is at $T7_{HV}$, with one additional connection it is at $T10_{HV}$ and with two additional neutral points it is at $T9_{HV}$. This is also depicted in Figure 67.

### 7.1.3 Influence of E-field Direction

The direction of the induced electric field has a major influence on the neutral point changes. Solar storm forecasts

predict the impact time, angle and magnitudes of the magnetic field changes, which lead to the induced electric field. With an electric field of $E_x = 1\,\frac{V}{km}$ and $E_y = 1\,\frac{V}{km}$, the initial current in transformer $T7_{HV}$ is the highest. For this case, the optimum for the objective function is the connection of $T6_{HV}$ and the reduction of current $T7_{HV}$, as shown in Figure 67 and Figure 68. A slight uncertainty in the space weather predictions immediately changes this result.

To further investigate the influence of the electric field direction on the optimal neutral connections, the angle $\vartheta$ of the electric field with a magnitude of 1 V/km is changed. As shown in Figure 44, the angle is varied clockwise from 0° to 180° in increments of 1°. For each angle change, the optimization algorithm calculates the optimal neutral point change. With only one neutral point change, this leads to the reductions of the objective function as shown in Figure 70. Depending on the E-field direction, either the connection of $T8_{HV}$, $T11_{HV}$ or $T6_{HV}$ leads to the highest reduction of the objective function. In the case of a uniform electric field, as it is used in this study, the currents and effects repeat after 180° as the transformer core would saturate in the other half-cycle. Therefore, the applied rotation from 0° to 180° covers all cases.

Figure 70 shows that the mitigation effect is limited and very dependent on the electric field direction $\vartheta$. The highest reduction with only one additional connected neutral point of 30% is possible, if the E-field has a direction of 100°, which corresponds to a south-east and north-west direction. The maximum current in this case occurs in transformer $T7_{HV}$ and can be effectively reduced by connecting the parallel transformer neutral point of $T6_{HV}$.

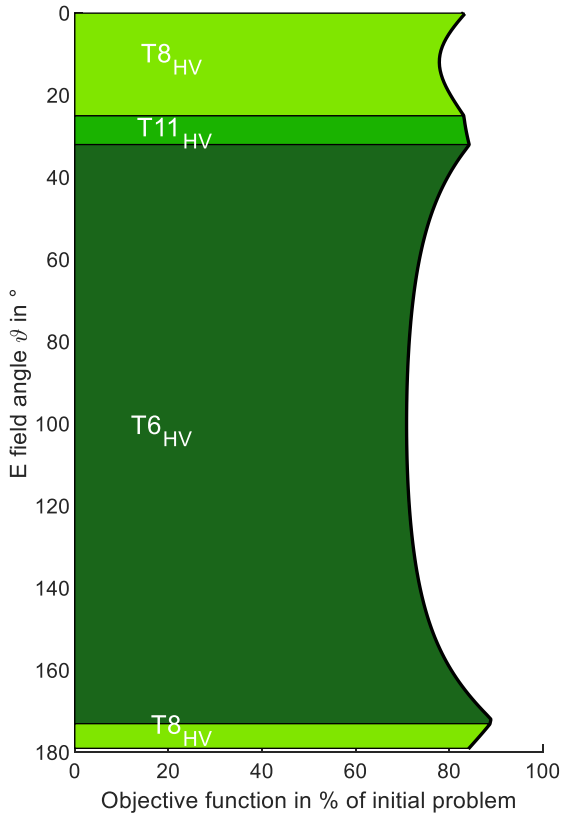


*Figure 70: Objective function depending on E-field direction and additional connected neutral points*

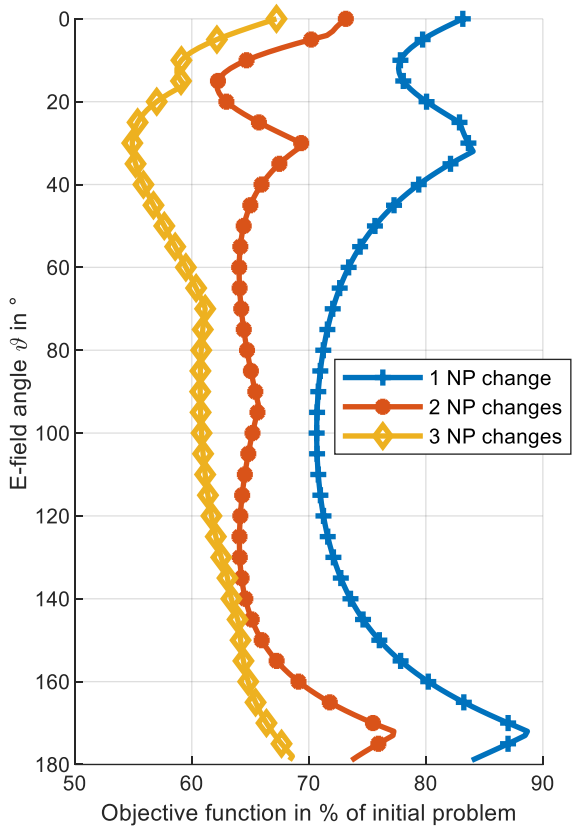


*Figure 71: Objective function depending on E-field direction for three different allowed neutral point changes.*

The minimum reduction of 12% occurs in the range of 170°. In this field direction, the currents of several transformers are high but none has an extreme value. This means that even though the highest current is reduced to an applicable value, the currents of other transformers are still large and lead to high values in the objective function. To overcome this problem, more neutral point connections are needed.

Similar to what Section 7.1.2 conveys, more neutral point changes are allowed and the effect is analyzed in Figure 71. The three lines show the objective function in the percentage of the initial problem for one, two or three neutral point changes and the dependency on the E-field direction. As expected, and already presented in Figure 69, more neutral point changes lead to higher reductions of the objective function. The minimum, mean and maximum objective function in the percentage of the initial problem, as well as the maximum occurring current in p.u. for each of the three scenarios, are shown in Table 10. The improvement rate is the highest between one and two additional neutral point connections, but of course, three additional neutral points lead to the best results. A mean reduction of 39% is a remarkable result achieved without any additional assets.

*Table 10: Results depending on allowed neutral point changes*

| NP CHANGES | MAX I | MIN OBJ. FUNCTION | MEAN OBJ. FUNCTION | MAX OBJ. FUNCTION |
|---|---|---|---|---|
| | in p.u. | in % | in % | in % |
| **1** | 0,08 | 70 | 76 | 88 |
| **2** | 0,08 | 60 | 66 | 77 |
| **3** | 0,08 | 54 | 61 | 68 |

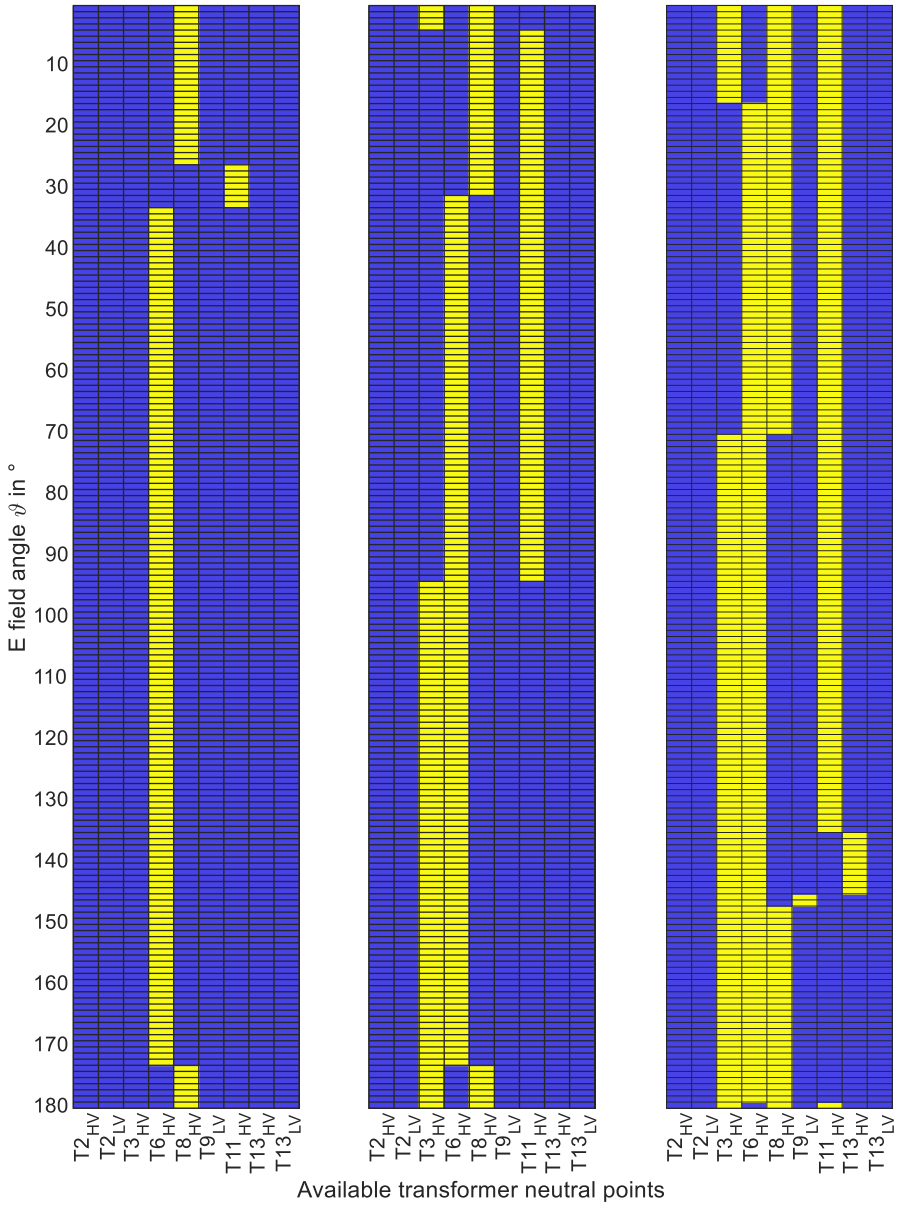


*Figure 72: Optimal additional neutral point connections for 1, 2 or 3 additional connections, depending on the electric field direction. Newly connected transformers are marked in yellow.*

The additional connected neutral points, depending on the E-field direction, are provided in Figure 72, which only includes the available neutral points. Depending on the allowed neutral point changes, either one, two or three, the additional connected transformers are marked in yellow. This can be used as pre-calculated switching states for different electric field directions.

Not every available transformer neutral point is utilized in the same way. Figure 73 shows the number of additional connections of the available transformer neutral points. This shows that some transformers are of higher importance for mitigation actions than others. Transformer neutral $T6_{HV}$ is the one most used by this mitigation algorithm. This leads to the highest reductions during the E-field variations. On the contrary, transformers T9 and T13 are only used in a minor way, as the reduction achieved with them is small.

The high utilization rates of, e.g., $T6_{HV}$ for this mitigation approach means that these transformers are of significant importance. A restriction of these transformers, as shown in Section 7.1.2 and Figure 68 for only one E-field

direction, leads to a significant drop in mitigation effectiveness. A possible restriction reason in grid calculation software should be analyzed in detail, especially for transformers with high utilization rates.

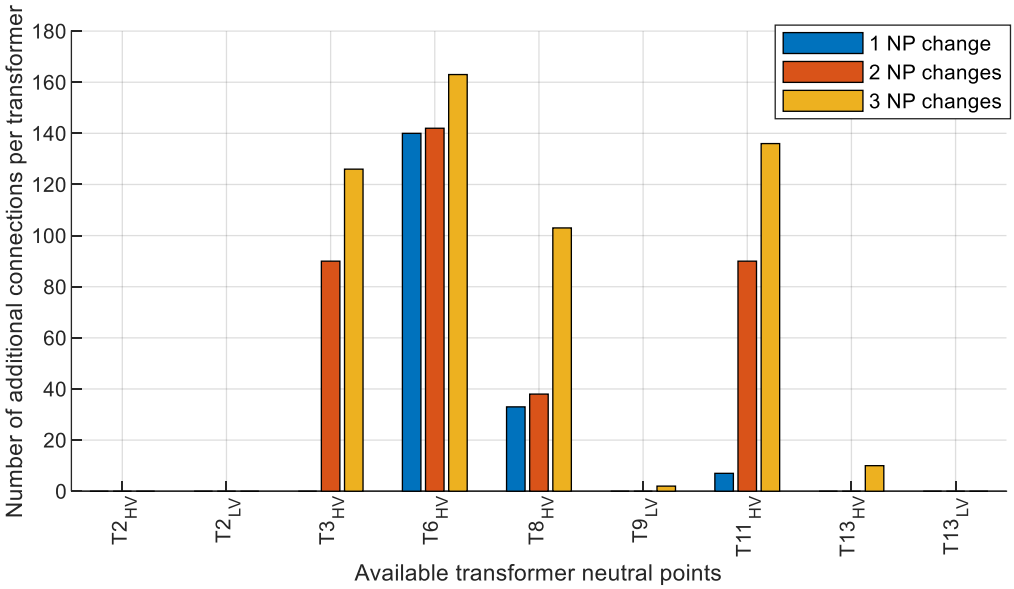


*Figure 73: Number of additional connections per transformer and scenario.*

## 7.2 Mitigation Conclusion

The new GIC mitigation method presented shows effectiveness in a test grid. It is based on the fact that not all transformer neutral points in a grid are connected to ground. An optimization problem is formulated that reduces the GIC impact on a system-wide view and is implemented in the LFC simulator. The optimization variable represents all neutral points in the grid and new connections are added to reduce the transformer currents by distributing it to other transformers. It is demonstrated that the algorithm can effectively reduce transformer currents. The effectiveness of this mitigation approach also depends on the direction of the electric field and the sensitivity of transformers in the respective direction. A a test grid shows that the formulated objective function can be reduced by up to 46% by connecting three additional transformer neutral points to the ground.

Due to restrictions from the grid operation, the optimal connections may not be possible. Therefore, alternative solutions are also calculated and compared. The changes in grid topology can be easily tested for feasibility in other grid calculation software, e.g., to calculate the impact on fault currents. This modular approach has the advantage that information about the power plant operations of the whole grid is not needed in the LFC simulator.

Other grid mitigation measures might still be required if the reduction of transformer currents through neutral point changes is insufficient or essential connections cannot be changed. However, the number of such measures can probably be decreased by using the suggested approach.

The objective function used herein aims for a distribution of high currents onto several transformers and therefore a reduction of the GIC load and possible damage to one transformer. The mitigation of additional reactive power demand of transformers or harmonic emissions due to saturation is dependent on the transformer type and therefore may result in different optimal neutral connections. Additionally, the constraints could be adapted to include more transformer details and limits. However, independent of the selected objective function, this mitigation approach reduces the GIC impact on the grid without any additional investments in new assets or mitigation devices and can be quickly applied to power grids.

# 8 Conclusion

## 8.1 Low frequency current measurement system

The neutral point measurement system in operation in Austria is unique in Europe. The two different system types either bypass the transformer neutral point or are mounted on the earthing switch. With the increasing number of measurement systems, all different transformer types (transformer bank, three-phase, autotransformer) in the Austrian Power grid are equipped and provide data for analysis. The measurement system is active since 2017 and the data from nine sites is transferred to a central server. Since 2017, several geomagnetic storms have been measured and analyzed. The largest ever recorded GIC in the Austrian power grid was recognized in April 2023 and had a magnitude of 20.9 A.

The positions for new measurement systems were selected according to several criteria. The first criteria were GIC calculations, which gave an estimation of interesting measurement sites. This goes hand in hand with the geographical distribution of the Austrian power grid and the different geological areas in Austria. Another criterion was the strategic position in substations to track the change in neutral point currents before and after large changes in grid topology were made. And finally, the installation near possible LFC sources was also in focus.

The measurement range of ± 25 A is suitable for Austria and the sampling interval of 1s is also high enough for long-term analysis. Nevertheless, for the identification of LFC sources, a higher sampling rate is in some cases needed.

Additionally to the expansion of the neutral point measurement system, a new method to measure LFCs on high voltage potential is under development. This system uses the influence of magnetic fields on the polarization angle of linear polarized light. With this system, several assumptions, e.g., the distribution of LFCs in the three-phase system, can be checked.

## 8.2 Sources of LFC

The sources of LFCs were further investigated: The source with the highest impact on grids is of course the sun and the geomagnetically induced currents during solar storms. The most recent storm in April 2023 led to the highest ever recorded currents in Austria of up to 20.9 A.

The effect of public transportation systems using DC supply on transformers was further analyzed. Because of the special operating hours of the Vienna subway system during the COVID-19 pandemic, the correlation between neutral point currents and subway systems was confirmed. Additional measurements at connection points of the subway and public earthing systems delivered further proof of this correlation. In conclusion, DC-supply of transportation systems in metropolitan areas can cause DC currents in transformers, which can be clearly distinguished from GIC by their frequency range and time of appearance.

The combination of neutral point measurements, phasor measurements and switching protocols led to the conclusion, that switching in power systems also leads to neutral point currents. The connection of shunt reactors in transformer tertiary windings to compensate reactive power and to regulate line voltage leads to inrush currents on the transformer's primary side. If the power system is not completely symmetric in terms of impedance, which is usually the case, the inrush currents will also lead to a zero-sequence current and hence to DC neutral point currents during the energization of the reactor. This effect can be seen over long distances. Also, the tap-changing process of transformers can be seen in neutral point currents. As these DC transients only last a few seconds to minutes,

they are not considered as a risk for half-cycle saturation.

## 8.3 Calculation of GIC

To improve the usability of the GIC calculation code, a graphical user interface was created and the LFC simulator was programmed. With this software, GICs and the related impact can be easily calculated without the need to understand the mathematics behind them.

The plane wave method with the nodal admittance calculation and a DC source between the substation grounding and a reference substation is suitable for grids, where the electric field can be assumed as uniform.

The analysis and comparison between neutral point measurements and simulations show, that unknown grid parameters, e.g. number of grounded neutral points or changes in the grid topology, have the highest impact on the simulation accuracy.

## 8.4 Impact of LFC on the Grid

The additional reactive power demand calculation of transformers caused by half-cycle saturation was implemented in the LFC simulator. With datasets about transformers in the Austrian power grid, the reactive power calculation was adapted to include the non-linear behavior of transformer saturation. The additional reactive power demand is added as reactive power loads in load flow simulations, which are performed outside the LFC simulator. The modular approach enables the usage of LFC data in other grid calculation software. The effect of severe geomagnetic disturbances was simulated in two grid scenarios. In the scenario with a critical line outage, the increased reactive power demand leads to undervoltage in the system and critical situations can occur. The usage of voltage-supporting measures (e.g. generators in idle mode, reactive power compensation units, synchronous condensers,…) can counteract these problems. However, because of the available datasets, the impact was only analyzed on the Austrian power grid. Voltage problems in neighboring countries could again lead to disturbances also in Austria.

The behavior of the transformer's magnetizing currents under DC bias and voltage distortion is discussed. As long as the resulting voltage harmonics stay within reasonable boundaries of up to 10% (depending on the harmonic order), an implementation of the transformer as a harmonic current source for harmonic analysis is possible. This enables the analysis of the influence of the DC bias on voltage distortion in a simplified way using classical harmonic load flow studies. Although the method has limited accuracy, it is sufficient to estimate a possible threat to the system.

## 8.5 Reduction of LFC impact

The saturation of transformers, caused by LFC in transformer neutrals, poses a threat to the grid. However, since there are not all transformer neutral points in the power grid connected to ground, there is a potential to minimize the effect of LFC by selective connection or disconnection of neutrals. Constraints in the selection of grounding points are given the strategies to limit fault currents, management of overvoltages in unbalanced faults and other safety issues. In case of a solar storm, specific configurations of grounded transformer neutral points can be utilized to distribute the GICs, and hence to stress, of one transformer onto several transformers. To find the best topology to reduce the GIC load on the grid, an optimization algorithm was developed. The optimization variable contains all available neutral points in a grid, which can be utilized for switching. The objective function minimizes the squared

transformer neutral currents, which penalizes high currents and shows good results in a test grid. The algorithm includes several constraints, e.g., a maximum number of neutral point changes or the maximum currents through a transformer. In each iteration of the optimization algorithm, a full GIC calculation is performed, as the change of neutral point connections directly influences the current distributions. This process is non-linear, therefore, the optimization is done with a genetic algorithm.

The number and location of connected neutral points also directly influence fault currents and grid operation. Each proposed new neutral point connection must therefore be checked for applicability, which is done in grid calculation software outside the LFC simulator. As some of the proposed connections may not be possible, the algorithm produces several connection schemes with decreasing impact. This new approach to GIC mitigation was tested on a small grid, showing possible reductions in the objective function of up to 46%. This is especially remarkable, as no additional assets need to be installed in the grid. However, the reduction impact must be analyzed for every grid in detail.

## 8.6 Future work

**Measuring LFCs**

The LFC measurement system is on a good level, however, more measurement systems would be preferable, e.g., one in the most western part of Austria, as there are no systems yet. Bypass systems should be replaced by mounted system, as this would improve the acceptance of the grid operator. As the solar storm in April led to magnitudes close to the measurement range, the measurement range should be adapted.

As soon as the prototype of the optical current measurement is ready for field applications, measurements may show new insights into the distribution of LFCs in the three-phase power system.

**LFC Simulator**

The LFC simulation tool has several features in the current version, which are not completely open for public use. The implementation of all parameters, simulation options, mitigation algorithms etc. into the graphical user interface should be the next step.

A more complex, and therefore time-consuming, task would be the development of APIs to other grid calculation software. With these interfaces, the analysis of grid impact could be done even faster and the integration into grid planning and operation would be possible in an easy-to-use way. The interface would also enable the fault current check to be inside the mitigation algorithm.

**Grid Impacts**

The impact of half-cycle saturation and hence on harmonics was done in a more or less rudimentary way. To gain knowledge about the relation between LFCs and harmonics, data loggers are installed in the power grid to measure harmonics on the transformer terminals. However, at the time of writing, too little data is available. With the harmonic and neutral point measurements, the calculations in section 6 can be assessed and further improved. With this data, also harmonic load flow analysis can be performed and cross-checked with measurements.

**GIC Mitigation**

The concept of GIC mitigation by optimizing neutral point connections was shown in this thesis. There is room for

improvements e.g., a detailed analysis of the genetic algorithm preferences. Additionally, the performance in a real grid with real storm data would be of interest.

# 9 References


[1] T. Halbedl, H. Renner, M. Sakulin, and G. Achleitner, “Measurement and analysis of neutral point currents in a 400-kV-network,” in *2014 Electric Power Quality and Supply Reliability Conference (PQ)*, Rakvere, Estonia, 2014, pp. 65–68.

[2] R. L. Bailey, T. Halbedl, I. Schattauer, A. Römer, G. Achleitner, C. D. Beggan, V. Wesztergom, R. Egli, and R. Leonhardt, “Modelling geomagnetically induced currents in midlatitude Central Europe using a thin-sheet approach,” *Ann. Geophys.*, vol. 35, no. 3, pp. 751–761, 2017, doi: 10.5194/angeo-35-751-2017.

[3] T. Halbedl, H. Renner, R. L. Bailey, R. Leonhardt, and G. Achleitner, “Analysis of the impact of geomagnetic disturbances on the Austrian transmission grid,” in *19th Power Systems Computation Conference*, Genoa, Italy, 2016, pp. 1–5.

[4] R. L. Bailey, T. Halbedl, I. Schattauer, G. Achleitner, and R. Leonhardt, “Validating GIC Models With Measurements in Austria: Evaluation of Accuracy and Sensitivity to Input Parameters,” *Space Weather*, vol. 16, no. 7, pp. 887–902, 2018, doi: 10.1029/2018SW001842.

[5] T. Halbedl, “Low Frequency Neutral Point Currents on Transformer in the Austrian power Transmission Network,” PhD Thesis, Institute of Electrical Power Systems, Graz University of Technology, Graz, 2019. [Online]. Available: https://diglib.tugraz.at/download.php?id=5cc8220f5d096&location=browse

[6] M. Wik, “The Sun, Space Weather and Effects,” Swedish Institute of Space Physics, Lund University, Lund, 2008. [Online]. Available: https://lup.lub.lu.se/search/ws/files/5593404/1259715.pdf

[7] R. L. Bailey, “Space weather and geomagnetically induced currents in Austria,” PhD Thesis, Geophysik, Universität Wien, Vienna, 2018.

[8] L. Rosenqvist, T. Fristedt, A. P. Dimmock, P. Davidsson, R. Fridström, J. O. Hall, L. Hesslow, J. Kjäll, M. Y. Smirnov, d. Welling, and P. Wintoft, “3D Modeling of Geomagnetically Induced Currents in Sweden—Validation and Extreme Event Analysis,” *Space Weather*, vol. 20, no. 3, 2022, doi: 10.1029/2021SW002988.

[9] B. T. Tsurutani and W. D. Gonzalez, “The Interplanetary causes of magnetic storms: A review,” *Washington DC American Geophysical Union Geophysical Monograph Series*, vol. 98, pp. 77–89, 1997, doi: 10.1029/GM098p0077.

[10] M. Wik, R. Pirjola, H. Lundstedt, A. Viljanen, P. Wintoft, and A. Pulkkinen, “Space weather events in July 1982 and October 2003 and the effects of geomagnetically induced currents on Swedish technical systems,” *Ann. Geophys.*, vol. 27, no. 4, pp. 1775–1787, 2009, doi: 10.5194/angeo-27-1775-2009.

[11] R. A. D. Fiori, D. H. Boteler, and D. M. Gillies, “Assessment of GIC risk due to geomagnetic sudden commencements and identification of the current systems responsible,” *Space Weather*, vol. 12, no. 1, pp. 76–91, 2014, doi: 10.1002/2013SW000967.

[12] J. W. Dungey, “Interplanetary Magnetic Field and the Auroral Zones,” *Phys. Rev. Lett.*, vol. 6, no. 2, pp. 47–48, 1961, doi: 10.1103/PhysRevLett.6.47.

[13] J. BARTELS, “II - The Technique of Scaling Indices K and Q of Geomagnetic Activity,” in *Annals of The International Geophysical Year, Geomagnetism*, International Council of Scientific Unions Comité Spécial de l’Année Géophysique Internationale (CSAGI), Ed.: Pergamon, 1957, pp. 215–226. [Online]. Available: http://www.sciencedirect.com/science/article/pii/B9781483213040500063

[14] GFZ Potsdam, *Geomagnetischer Kp-Index.* [Online]. Available: https://kp.gfz-potsdam.de/ (accessed: May 9 2023).

[15] J. Matzka, C. Stolle, Y. Yamazaki, O. Bronkalla, and A. Morschhauser, “The Geomagnetic Kp Index and Derived Indices of Geomagnetic Activity,” *Space Weather*, vol. 19, no. 5, 2021, doi: 10.1029/2020SW002641.

[16] J. Matzka, O. Bronkalla, K. Tornow, K. Elger, and C. Stolle, “Geomagnetic Kp index,” 2021.

[17] A. Chlaki and M. Kuznetsova, *CME Scoreboard.* [Online]. Available: https://kauai.ccmc.gsfc.nasa.gov/CMEscoreboard/ (accessed: May 9 2023).

[18] NOAA's National Weather Service, *SPACE WEATHER PREDICTION CENTER.* [Online]. Available: https://www.swpc.noaa.gov/noaa-scales-explanation# (accessed: May 12 2023).

[19] P. Riley, M. L. Mays, J. Andries, T. Amerstorfer, D. Biesecker, V. Delouille, M. Dumbović, X. Feng, E. Henley, J. A. Linker, C. Möstl, M. Nuñez, V. Pizzo, M. Temmer, W. K. Tobiska, C. Verbeke, M. J. West, and X. Zhao, “Forecasting the Arrival Time of Coronal Mass Ejections: Analysis of the CCMC CME Scoreboard,” *Space Weather*, vol. 16, no. 9, pp. 1245–1260, 2018, doi: 10.1029/2018SW001962.

[20] P. Riley, M. Ben-Nun, J. A. Linker, M. J. Owens, and T. S. Horbury, “Forecasting the properties of the solar wind using simple pattern recognition,” *Space Weather*, vol. 15, no. 3, pp. 526–540, 2017, doi: 10.1002/2016SW001589.

[21] P. Riley, M. A. Reiss, and C. Möstl, “Which Upstream Solar Wind Conditions Matter Most in Predicting Bz Within Coronal Mass Ejections,” *Space Weather*, vol. 21, no. 4, 2023, doi: 10.1029/2022SW003327.

[22] R. L. Bailey, R. Leonhardt, C. Möstl, C. Beggan, M. A. Reiss, A. Bhaskar, and A. J. Weiss, “Forecasting GICs and Geoelectric Fields From Solar Wind Data Using LSTMs: Application in Austria,” *Space Weather*, vol. 20, no. 3, 2022, doi: 10.1029/2021SW002907.

[23] W. H. Barlow, “On the spontaneous electrical currents observed in the wires of the electric telegraph,” *Phil. Trans. R. Soc.*, vol. 139, pp. 61–72, 1849, doi: 10.1098/rstl.1849.0006.

[24] R. C. Carrington, “Description of a Singular Appearance seen in the Sun on September 1, 1859,” *Monthly Notices of the Royal Astronomical Society*, vol. 20, no. 1, pp. 13–15, 1859, doi: 10.1093/mnras/20.1.13.

[25] Daily Chronicle & Sentinel., *The Auroa Borealis and the Telegraph.* [Online]. Available: https://gahistoricnewspapers.galileo.usg.edu/lccn/sn82015215/1859-09-08/ed-1/seq-1/ (accessed: Mar. 4 2022).

[26] J. L. Green, S. Boardsen, S. Odenwald, J. Humble, and K. A. Pazamickas, “Eyewitness reports of the great auroral storm of 1859,” *Advances in Space Research*, vol. 38, no. 2, pp. 145–154, 2006, doi: 10.1016/j.asr.2005.12.021.

[27] D. H. Boteler, “The super storms of August/September 1859 and their effects on the telegraph system,” *Advances in Space Research*, vol. 38, no. 2, pp. 159–172, 2006, doi: 10.1016/j.asr.2006.01.013.

[28] L. J. Lanzerotti, “Space Weather: Historical and Contemporary Perspectives,” *Space Science Reviews*, vol. 212, no. 3, pp. 1253–1270, 2017, doi: 10.1007/s11214-017-0408-y.

[29] L. J. Lanzerotti, “Space Weather Effects on Technologies,” *Space Weather*, pp. 11–22, 2001, doi: 10.1029/GM125p0011.

[30] D. H. Boteler, “A 21st Century View of the March 1989 Magnetic Storm,” *Space Weather*, vol. 17, no. 10, pp. 1427–1441, 2019, doi: 10.1029/2019SW002278.

[31] J. Allen, H. Sauer, L. Frank, and P. Reiff, “Effects of the March 1989 solar activity,” *Eos Trans. AGU*, vol. 70, no. 46, p. 1479, 1989, doi: 10.1029/89EO00409.

[32] L. Bolduc, “GIC observations and studies in the Hydro-Québec power system,” *Journal of Atmospheric and Solar-Terrestrial Physics*, vol. 64, no. 16, pp. 1793–1802, 2002, doi: 10.1016/S1364-6826(02)00128-1.

[33] J. G. Kappenman and V. Albertson, “Bracing for the geomagnetic storms,” *IEEE Spectr.*, vol. 27, no. 3, pp. 27–33, 1990, doi: 10.1109/6.48847.

[34] R. A. Marshall, M. Dalzell, C. L. Waters, P. Goldthorpe, and E. A. Smith, “Geomagnetically induced currents in the New Zealand power network,” *Space Weather*, vol. 10, no. 8, 1-13, 2012, doi: 10.1029/2012SW000806.

[35] J. P. Eastwood, M. A. Hapgood, E. Biffis, D. Benedetti, M. M. Bisi, L. Green, R. D. Bentley, and C. Burnett, “Quantifying the Economic Value of Space Weather Forecasting for Power Grids: An Exploratory Study,” *Space Weather*, vol. 16, no. 12, pp. 2052–2067, 2018, doi: 10.1029/2018SW002003.

[36] A. Pulkkinen, S. Lindahl, A. Viljanen, and R. Pirjola, “Geomagnetic storm of 29-31 October 2003: Geomagnetically induced currents and their relation to problems in the Swedish high-voltage power transmission system,” *Space Weather*, vol. 3, no. 8, 2005, doi: 10.1029/2004SW000123.

[37] C. Balch, B. Murtagh, D. Zezula, L. Combs, N. Gayle, K. Tegnell, M. Crown, and B. McGehan, “Intense space weather storms October 19-November 07, 2003,” National Oceanic and Atmospheric Administration. [Online]. Available: https://repository.library.noaa.gov/view/noaa/6995/noaa_6995_DS1.pdf

[38] C. T. Gaunt and G. Coetzee, “Transformer failures in regions incorrectly considered to have low GIC-risk,” in *IEEE Lausanne Power Tech, 2007: Lausanne, Switzerland, 1-5 July 2007*, Lausanne, Switzerland, 2007, pp. 807–812.

[39] D. H. Hathaway, “The Solar Cycle,” *Living reviews in solar physics*, vol. 12, p. 4, 2015, doi: 10.1007/lrsp-2015-4.

[40] K. Petrovay, “Solar cycle prediction,” *Living Rev Sol Phys*, vol. 17, no. 1, 2020, doi: 10.1007/s41116-020-0022-z.

[41] NOAA, *Solar Cycle Progression.* [Online]. Available: https://www.swpc.noaa.gov/products/solar-cycle-progression (accessed: Jun. 4 2020).

[42] C. Möstl, A. J. Weiss, R. L. Bailey, M. A. Reiss, T. Amerstorfer, J. Hinterreiter, M. Bauer, S. W. McIntosh, N. Lugaz, and D. Stansby, “Prediction of the In Situ Coronal Mass Ejection Rate for Solar Cycle 25: Implications for Parker Solar Probe In Situ Observations,” *ApJ*, vol. 903, no. 2, p. 92, 2020, doi: 10.3847/1538-4357/abb9a1.

[43] D. Albert, P. Schachinger, H. Renner, P. Hamberger, F. Klammler, and G. Achleitner, “Field experience of small quasi DC bias on power transformers A first classification of low-frequency current pattern and identification of sources,” in *Cigre Session 48*, Cigre, Ed., Paris, 2020.

[44] X. Dong, Y. Liu, and J. G. Kappenman, “Comparative analysis of exciting current harmonics and reactive power consumption from GIC saturated transformers,” in *2001 IEEE Power Engineering Society winter meeting conference proceedings: 28 January-1 February 2001, Columbus, Ohio USA*, Columbus, OH, USA, 2001, pp. 318–322.

[45] R. A. Walling and A. N. Khan, “Characteristics of transformer exciting-current during geomagnetic disturbances,” *IEEE Trans. Power Delivery*, vol. 6, no. 4, pp. 1707–1714, 1991, doi: 10.1109/61.97710.

[46] J. Raith, “Risk Assessment of Power Transformers under the Influence of Geomagnetically Induced Currents (GIC),” PhD Thesis, Hochspannungstechnik und Systemmanagement, TU Graz, Graz, 2019. [Online]. Available: https://diglib.tugraz.at/risk-assessment-of-power-transformers-under-the-influence-of-geomagnetically-induced-currents-gic-2019

[47] Cigre, “Load sound power levels for specification purposes of three-phase 50 Hz and 60 Hz liquid-filled power transformers,” Cigre WGR_310_1, 2020. Accessed: Feb. 27 2020. [Online]. Available: https://e-cigre.org/publication/WGR_310_1-load-sound-power-levels-for-specification-purposes-of-three-phase-50-hz-and-60-hz-liquid-filled-power-transformers

[48] M. Beltle and S. Tenbohlen, “Power transformer diagnosis based on mechanical oscillations due to AC and DC currents,” *IEEE Trans. Dielect. Electr. Insul.*, vol. 23, no. 3, pp. 1515–1522, 2016, doi: 10.1109/TDEI.2016.005537.

[49] G. Shilyashki, H. Pfützner, P. Hamberger, M. Aigner, A. Kenov, and I. Matkovic, “Spatial distributions of magnetostriction, displacements and noise generation of model transformer cores,” *International Journal of Mechanical Sciences*, vol. 118, pp. 188–194, 2016, doi: 10.1016/j.ijmecsci.2016.09.022.

[50] J. Raith and U. Schichler, “Risk assessment of electrical equipment under the influence of GIC,” in *2016 International Conference on Condition Monitoring and Diagnosis*, pp. 341–344.

[51] H. K. Chisepo, “Measurements and finite element modelling of transformer flux with dc and power frequency current,” Ph Thesis, Department of Electrical Engineering, University of Cape Town, Cape Town, South Africa, 2019. Accessed: Sep. 14 2020. [Online]. Available: https://open.uct.ac.za/bitstream/handle/11427/31218/thesis_ebe_2019_chisepo_hilary_kudzai.pdf?sequence=1&isAllowed=y

[52] R. Pirjola, “Electromagnetic induction in the earth by a plane wave or by fields of line currents harmonic in time and space,” Phd Thesis, Finnish Meteorological Institute, Helsinki, 1982.

[53] A. Thomson and S. Flower, “Modernizing a Global Magnetic Partnership,” *Eos*, vol. 102, 2021, doi: 10.1029/2021EO156569.

[54] Intermagnet, *Intermagnet.* [Online]. Available: https://intermagnet.github.io/ (accessed: Oct. 31 2022).

[55] R. Leonhardt, R. Egli, B. Leichter, I. Herzog, R. Kornfeld, R. L. Bailey, N. Kompein, P. Arneitz, R. Mandl, and R. Steiner, “Conrad Observatory, GMO Bulletin 6,” 2020.

[56] D. H. Boteler, “Calculating the voltages induced in technological systems during a geomagnetic disturbance,” *IEEE Trans. Electromagn. Compat.*, vol. 41, no. 4, pp. 398–402, 1999, doi: 10.1109/15.809834.

[57] L. Cagniard, “Basic theory of the magneto-telluric method of geophysical prospecting,” *GEOPHYSICS*, vol. 18, no. 3, pp. 605–635, 1953, doi: 10.1190/1.1437915.

[58] P. Weidelt and A. D. Chave, “The magnetotelluric response function,” in *The magnetotelluric method: Theory and practice*, A. D. Chave and A. G. Jones, Eds., Cambridge: Cambridge University Press, 2012, pp. 122–164.

[59] B. Dong, Z. Wang, D. Boteler, and R. Pirjola, “Review of earth conductivity structure modelling for calculating geo-electric fields,” in *IEEE Power and Energy Society general meeting (PES), 2013*, Vancouver, BC, 2013, pp. 1–5.

[60] A. Kelbert, “The Role of Global/Regional Earth Conductivity Models in Natural Geomagnetic Hazard Mitigation,” *Surveys in Geophysics*, vol. 41, no. 1, pp. 115–166, 2020, doi: 10.1007/s10712-019-09579-z.

[61] A. Ádám, E. Prácser, and V. Wesztergom, “Estimation of the electric resistivity distribution (EURHOM) in the european lithosphere in the frame of the eurisgic WP2 project,” *Acta Geodaetica et Geophysica Hungarica*, vol. 47, no. 4, pp. 377–387, 2012, doi: 10.1556/AGeod.47.2012.4.1.

[62] P. Fernberg, “One-Dimensional Earth Resistivity Models for Selected Areas of Continental United States and Alaska: EPRI Technical Update 1026430,” 2012. Accessed: Apr. 8 2019. [Online]. Available: http://jupiter.ethz.ch/~kuvshinov/For_Dima_Alexeev/150116_Relevant_Papers_for_Revision/1D_profiles_for_North_America.pdf

[63] L. Marti, A. Rezaei-Zare, and D. H. Boteler, “Calculation of Induced Electric Field During a Geomagnetic Storm Using Recursive Convolution,” *IEEE Trans. Power Delivery*, vol. 29, no. 2, pp. 802–807, 2014, doi: 10.1109/TPWRD.2013.2273833.

[64] A. T. PRICE, “The induction of electric currents in non-uniform thin sheets and shells,” *Q J Mechanics Appl Math*, vol. 2, no. 3, pp. 283–310, 1949, doi: 10.1093/qjmam/2.3.283.

[65] G. Vasseur and P. Weidelt, “Bimodal electromagnetic induction in non-uniform thin sheets with an application to the northern Pyrenean induction anomaly,” *Geophys. J. Int.*, vol. 51, no. 3, pp. 669–690, 1977, doi: 10.1111/j.1365-246X.1977.tb04213.x.

[66] Weaver and J. T., “Regional induction in Scotland: an example of three-dimensional numerical modelling using the thin sheet approximation,” 1982. [Online]. Available: https://www.semanticscholar.org/paper/Regional-induction-in-Scotland%3A-an-example-of-using-Weaver/9ab38e8d1d217d71ba0fd7991e74a06d9b0b6929

[67] C. D. Beggan, D. Beamish, A. Richards, G. S. Kelly, and A. Thomson, “Prediction of extreme geomagnetically induced currents in the UK high-voltage network,” *Space Weather*, vol. 11, no. 7, pp. 407–419, 2013, doi: 10.1002/swe.20065.

[68] A. J. McKay, “Geoelectric Fields and Geomagnetically Induced Currents in the United Kingdom,” University of Edingburgh. Accessed: Jun. 1 2019. [Online]. Available: https://www.era.lib.ed.ac.uk/bitstream/id/1414/allanmckthesis.pdf/

[69] T. Divett, M. Ingham, C. D. Beggan, G. S. Richardson, C. J. Rodger, A. W. P. Thomson, and M. Dalzell, “Modeling Geoelectric Fields and Geomagnetically Induced Currents Around New Zealand to Explore GIC in the South Island's Electrical Transmission Network,” *Space Weather*, vol. 15, no. 10, pp. 1396–1412, 2017, doi: 10.1002/2017SW001697.

[70] T. Divett, D. H. Mac Manus, G. S. Richardson, C. D. Beggan, C. J. Rodger, M. Ingham, E. Clarke, A. W. P. Thomson, M. Dalzell, and Y. Obana, “Geomagnetically Induced Current Model Validation From New Zealand's South Island,” *Space Weather*, vol. 18, no. 8, 2020, doi: 10.1029/2020SW002494.

[71] E. Ivannikova, M. Kruglyakov, A. Kuvshinov, L. Rastätter, and A. Pulkkinen, “Regional 3-D Modeling of Ground Electromagnetic Field Due To Realistic Geomagnetic Disturbances,” *Space Weather*, vol. 16, no. 5, pp. 476–500, 2018, doi: 10.1002/2017SW001793.

[72] A. Kelbert and G. M. Lucas, “Modified GIC Estimation Using 3-D Earth Conductivity,” *Space Weather*, vol. 18, no. 8, 2020, doi: 10.1029/2020SW002467.

[73] L. Rosenqvist and J. O. Hall, “Regional 3-D Modeling and Verification ofGeomagnetically Induced Currents in Sweden,” *Space Weather*, vol. 17, no. 1, pp. 27–36, 2019, doi: 10.1029/2018SW002084.

[74] S. Nakamura, Y. Ebihara, S. Fujita, T. Goto, N. Yamada, S. Watari, and Y. Omura, “Time Domain Simulation of Geomagnetically Induced Current (GIC) Flowing in 500-kV Power Grid in Japan Including a Three-Dimensional Ground Inhomogeneity,” *Space Weather*, vol. 66, no. 1, p. 164, 2018, doi: 10.1029/2018SW002004.

[75] L. Wang, J. Duan, A. P. Hitchman, A. M. Lewis, and W. V. Jones, “Modeling Geoelectric Fields Induced by Geomagnetic Disturbances in 3D Subsurface Geology, an Example From Southeastern Australia,” *JGR Solid Earth*, vol. 125, no. 9, 2020, doi: 10.1029/2020JB019843.

[76] C. Püthe and A. Kuvshinov, “Towards quantitative assessment of the hazard from space weather. Global 3-D modellings of the electric field induced by a realistic geomagnetic storm,” *Earth Planet Sp*, vol. 65, no. 9, pp. 1017–1025, 2013, doi: 10.5047/eps.2013.03.003.

[77] D. H. Boteler and R. J. Pirjola, “Modeling geomagnetically induced currents,” *Space Weather*, vol. 15, no. 1, pp. 258–276, 2017, doi: 10.1002/2016SW001499.

[78] S. Marsal, J. M. Torta, V. Canillas-Pérez, and J. J. Curto, “A New Standalone Tool for DC-Equivalent Network Generation and GIC Calculation in Power Grids with Multiple Voltage Levels,” *Space Weather*, e2021SW002984, 2022, doi: 10.1029/2021SW002984.

[79] M. Lehtinen and R. J. Pirjola, “Currents produced in earthed conductor networks by geomagnetically-induced electric fields,” *Ann. Geophysicae*, vol. 3, pp. 479–484, 1985.

[80] R. L. Bailey, *Modelling geomagnetically induced currents in Austria.* [Online]. Available: https://github.com/geomagpy/GEOMAGICA (accessed: Apr. 10 2019).

[81] J. Alves Ribeiro, F. J. G. Pinheiro, and M. A. Pais, “First Estimations of Geomagnetically Induced Currents in the South of Portugal,” *Space Weather*, vol. 19, no. 1, 2021, doi: 10.1029/2020SW002546.

[82] S. P. Blake, P. T. Gallagher, J. Campanyà, C. Hogg, C. D. Beggan, A. W. P. Thomson, G. S. Richardson, and D. Bell, “A Detailed Model of the Irish High Voltage Power Network for Simulating GICs,” *Space Weather*, vol. 16, no. 11, pp. 1770–1783, 2018, doi: 10.1029/2018SW001926.

[83] R. A. Marshall, A. Kelly, T. van der Walt, A. Honecker, C. Ong, D. Mikkelsen, A. Spierings, G. Ivanovich, and A. Yoshikawa, “Modeling geomagnetic induced currents in Australian power networks,” *Space Weather*, vol. 15, no. 7, pp. 895–916, 2017, doi: 10.1002/2017SW001613.

[84] K. E. J. Huttunen, S. P. Kilpua, A. Pulkkinen, A. Viljanen, and E. Tanskanen, “Solar wind drivers of large geomagnetically induced currents during the solar cycle 23,” *Space Weather*, vol. 6, no. 10, 2008, doi: 10.1029/2007SW000374.

[85] J. M. Torta, L. Serrano, J. R. Regué, A. M. Sánchez, and E. Roldán, “Geomagnetically induced currents in a power grid of northeastern Spain,” *Space Weather*, vol. 10, no. 6, 2012, doi: 10.1029/2012SW000793.

[86] D. Albert, P. Schachinger, R. L. Bailey, H. Renner, and G. Achleitner, “Analysis of long-term GIC measurements in transformers in Austria,” *Space Weather*, 2021, doi: 10.1029/2021SW002912.

[87] D. H. Boteler, R. Pirjola, C. Blais, and A. Foss, “Development of a GIC simulator,” in *2014 IEEE PES general meeting: Conference & exposition ; 27-31 July 2014, National Harbor, MD*, National Harbor, MD, USA, 2014, pp. 1–5.

[88] NERC, “Application Guide: Computing Geomagnetically-Induced Current in the Bulk-Power Systems,” 2013. [Online]. Available: https://www.nerc.com/comm/PC/Geomagnetic%20Disturbance%20Task%20Force%20GMDTF%202013/GIC%20Application%20Guide%202013_approved.pdf

[89] R. Horton, D. H. Boteler, T. J. Overbye, R. J. Pirjola, and R. C. Dugan, “A Test Case for the Calculation of Geomagnetically Induced Currents,” *IEEE Trans. Power Delivery*, vol. 27, no. 4, pp. 2368–2373, 2012, doi: 10.1109/TPWRD.2012.2206407.

[90] D. H. Boteler and R. J. Pirjola, “Modelling geomagnetically induced currents produced by realistic and uniform electric fields,” *IEEE Trans. Power Delivery*, vol. 13, no. 4, pp. 1303–1308, 1998, doi: 10.1109/61.714500.

[91] K. Patil, “Modeling and Evaluation of Geomagnetic Storms in the Electric Power System,” 2014. [Online]. Available: https://e-cigre.org/publication/C4-306_2014-modeling-and-evaluation-of-geomagnetic-storms-in-the-electric-power-system

[92] T. J. Overbye, T. R. Hutchins, K. Shetye, J. Weber, and S. Dahman, “Integration of geomagnetic disturbance modeling into the power flow: A methodology for large-scale system studies,” in *2012 North American Power Symposium (NAPS)*, 2012, pp. 1–7.

[93] Electric Power Research Institute (EPRI), “Monitoring and Mitigation of Geomagnetically Induced Currents,” 1015938, 2008.

[94] L. Marti, “Effects of Series Compensation Capacitors on Geomagnetically Induced Currents,” *IEEE Transactions on Power Delivery*, vol. 29, no. 4, pp. 2032–2033, 2014, doi: 10.1109/TPWRD.2014.2326984.

[95] A. A. Hussein, “Mitigation of geomagnetically induced currents by variable series reactor,” in *2017 North American Power Symposium (NAPS): 17-19 Sept. 2017*, Morgantown, WV, 2017, pp. 1–6.

[96] P. Hamberger, “SCHUTZEINRICHTUNG FÜR EINEN TRANSFORMATOR VOR GEOMAGNETICALLY INDUCED CURRENTS,” EP3179492B1 15198574.4.

[97] Alakula, M. A. F. K. and S. Lindahl, “Method and equipment for the protection of power systems against geomagnetically induced currents,” EP1766746 (A1), EP EP20050736455 20050504, Mar 28, 2007.

[98] H. Herterich, F. Klammler, P. Hamberger, and G. Leber, “Restoring efficiency, removing sound: Ready for DC in the grid with DC compensation and DC-ready transformers,” *Transformers Magazine*, no. 4, pp. 92–99, 2018.

[99] J. G. Kappenman, S. R. Norr, G. A. Sweezy, D. L. Carlson, v.d. Albertson, J. E. Harder, and B. L. Damsky, “GIC mitigation: a neutral blocking/bypass device to prevent the flow of GIC in power systems,” *IEEE Trans. Power Delivery*, vol. 6, no. 3, pp. 1271–1281, 1991, doi: 10.1109/61.85876.

[100] L. Bolduc, M. Granger, G. Pare, J. Saintonge, and L. Brophy, “Development of a DC Current-Blocking Device for Transformer Neutrals,” *IEEE Trans. Power Delivery*, vol. 20, no. 1, pp. 163–168, 2005, doi: 10.1109/TPWRD.2004.835437.

[101] A. D. Rajapakse, N. Perera, F. R. Faxvog, W. Jensen, G. Nordling, G. Fuchs, D. B. Jackson, T. L. Volkmann, N. Ruehl, and B. Groh, “Power grid stability protection against GIC using a capacitive grounding circuit,” in *2012 IEEE Power & Energy Society Transmission and Distribution Conference and Exposition: Making innovation work for tomorrow, experience it! : Orlando, Florida, May 7-10, 2012*, Orlando, FL, USA, 2012, pp. 1–6.

[102] *Power Transformers - Part 23: DC magnetic bia ssuppression devices*, 60076-23, IEC, Jan. 2018.

[103] A. Abu Hussein and M. H. Ali, “Suppression of geomagnetic induced current using controlled ground resistance of transformer,” *Electric Power Systems Research*, vol. 140, pp. 9–19, 2016, doi: 10.1016/j.epsr.2016.07.005.

[104] Z. Wang, Z. Xie, C. Liu, X. Lin, H. Qian, Y. He, Z. Zhang, Z. Li, and Z. Chen, “Novel DC Bias Suppression Device Based on Adjustable Parallel Resistances,” *IEEE Transactions on Power Delivery*, vol. 33, no. 4, pp. 1787–1797, 2018, doi: 10.1109/TPWRD.2017.2775679.

[105] A. Hesami Naghshbandy, A. Ghaderi Baayeh, and A. Faraji, “Mitigating the effects of geomagnetically induced currents in the power network,” *IET Generation, Transmission & Distribution*, vol. 14, no. 23, pp. 5514–5525, 2020, doi: 10.1049/iet-gtd.2020.0055.

[106] M. Nazir, K. Burkes, and J. H. Enslin, “Converter-Based Solutions: Opening New Avenues of Power System Protection Against Solar and HEMP MHD-E3 GIC,” *IEEE Transactions on Power Delivery*, vol. 36, no. 4, pp. 2542–2549, 2021, doi: 10.1109/TPWRD.2020.3016207.

[107] J. Zhu, C. Mao, B. Liu, Z. Wang, D. Wang, and H. Wang, “Design and Field Application of DC and Harmonic Suppression System for Neutral Current in 220 kV Substation,” *IEEE Trans. Ind. Electron.*, vol. 69, no. 8, pp. 7560–7570, 2022, doi: 10.1109/TIE.2021.3104582.

[108] B. Kovan and F. de Leon, “Mitigation of Geomagnetically Induced Currents by Neutral Switching,” *IEEE Transactions on Power Delivery*, vol. 30, no. 4, pp. 1999–2006, 2015, doi: 10.1109/TPWRD.2015.2434411.

[109] H. Zhu and T. J. Overbye, “Blocking Device Placement for Mitigating the Effects of Geomagnetically Induced Currents,” *IEEE Trans. Power Syst.*, vol. 30, no. 4, pp. 2081–2089, 2015, doi: 10.1109/TPWRS.2014.2357213.

[110] P.-H. Yang, Y. Li, L.-G. Liu, X.-L. Dong, and J.-J. Zhang, “Optimal placement of grounding small resistance in neutral point for restraining voltage fluctuation in power grid caused by geomagnetic storm,” *IET Generation, Transmission & Distribution*, vol. 13, no. 8, pp. 1456–1465, 2019, doi: 10.1049/iet-gtd.2018.6310.

[111] A. Lamichhane, A. Rezaei-Zare, and A. Asgary, “Optimal Placement of GIC Blocking Devices Considering Transformer Thermal Limit Using Surrogate Optimization,” in *2022 IEEE International Conference on Environment and Electrical Engineering and 2022 IEEE Industrial and Commercial Power Systems Europe (EEEIC / I&CPS Europe)*, Prague, Czech Republic, Jun. 2022 - Jul. 2022, pp. 1–6.

[112] A. H. Etemadi and A. Rezaei-Zare, “Optimal Placement of GIC Blocking Devices for Geomagnetic Disturbance Mitigation,” *IEEE Trans. Power Syst.*, vol. 29, no. 6, pp. 2753–2762, 2014, doi: 10.1109/TPWRS.2014.2309004.

[113] E. Arajärvi, R. J. Pirjola, and A. Viljanen, “Effects of neutral point reactors and series capacitors on geomagnetically induced currents in a high-voltage electric power transmission system,” *Space Weather*, vol. 9, no. 11, 2011, doi: 10.1029/2011SW000715.

[114] M. Kazerooni, H. Zhu, and T. J. Overbye, “Mitigation of Geomagnetically Induced Currents Using Corrective Line Switching,” *IEEE Trans. Power Syst.*, vol. 33, no. 3, pp. 2563–2571, 2018, doi: 10.1109/TPWRS.2017.2753840.

[115] M. Lu, H. Nagarajan, E. Yamangil, R. Bent, S. Backhaus, and A. Barnes, “Optimal Transmission Line Switching Under Geomagnetic Disturbances,” in *IEEE Transactions on Power Systems*, pp. 2539–2550. [Online]. Available: https://ieeexplore.ieee.org/document/8064715

[116] M. Ryu, H. Nagarajan, and R. Bent, “Mitigating the Impacts of Uncertain Geomagnetic Disturbances on Electric Grids: A Distributionally Robust Optimization Approach,” *IEEE Trans. Power Syst.*, p. 1, 2022, doi: 10.1109/TPWRS.2022.3147104.

[117] M. Beltle, M. Schühle, S. Tenbohlen, and U. Sundermann, “Das Verhalten von Leistungstransformatoren bei Beanspruchung mit Gleichströmen,” in *Stuttgarter Hochspannungssymposium 2016*, 2016. Accessed: Nov. 15 2018. [Online]. Available: https://www.researchgate.net/publication/296958913_Das_Verhalten_von_Leistungstransformatoren_bei_Beanspruchung_mit_Gleichstromen

[118] R. A. Marshall, H. Gorniak, T. van der Walt, C. L. Waters, M. d. Sciffer, M. Miller, M. Dalzell, T. Daly, G. Pouferis, G. Hesse, and P. Wilkinson, “Observations of geomagnetically induced currents in the Australian power network,” *Space Weather*, vol. 11, no. 1, pp. 6–16, 2013, doi: 10.1029/2012SW000849.

[119] A. C. Kellerman, R. Mcgranaghan, J. Bortnik, B. A. Carter, J. Hughes, R. F. Arritt, K. Venkataramani, C. H. Perry, J. McCormick, C. M. Ngwira, M. Cohen, and J. Yue, “Geomagnetically Induced Currents at Middle Latitudes: 1. Quiet-time Variability,” *Space Weather*, 2021, doi: 10.1029/2021SW002729.

[120] S. Watari, S. Nakamura, and Y. Ebihara, “Measurement of geomagnetically induced current (GIC) around Tokyo, Japan,” (in En;en), *Earth Planets Space*, vol. 73, no. 1, pp. 1–19, 2021, doi: 10.1186/s40623-021-01422-3.

[121] E. Matandirotya, P. J. Cilliers, R. R. van Zyl, D. T. Oyedokun, and J. de Villiers, “Differential magnetometer method applied to measurement of geomagnetically induced currents in Southern African power networks,” *Space Weather*, vol. 14, no. 3, pp. 221–232, 2016, doi: 10.1002/2015SW001289.

[122] J. Hübert, C. D. Beggan, G. S. Richardson, T. Martyn, and A. W. P. Thomson, “Differential Magnetometer Measurements of Geomagnetically Induced Currents in a Complex High Voltage Network,” *Space Weather*, vol. 18, no. 4, 2020, doi: 10.1029/2019SW002421.

[123] S. Marsal, J. M. Torta, J. J. Curto, V. Canillas-Pérez, O. Cid, M. Ibañez, and A. Marcuello, “Validating GIC modeling in the Spanish power grid by differential magnetometry,” *Space Weather*, 2021, doi: 10.1029/2021SW002905.

[124] J. Chen, C. Liu, M. Wang, and T. Wang, “Power system responses to geomagnetic disturbances recognized using phasor measurement recordings,” *International Journal of Electrical Power & Energy Systems*, vol. 113, pp. 932–940, 2019, doi: 10.1016/j.ijepes.2019.06.027.

[125] H. Parry, “Monitoring and Assessment of Geomagnetically Induced Currents in Alberta’s High Voltage Network,” Master Thesis, Department of Physics, University of Alberta, Alberta, Canada, 2022.

[126] U.S. Department of Energy, “Geomagnetic Disturbance Monitoring Approach and Implementation Strategies,” Washington, D.C., 2019.

[127] A. W. P. Thomson, A. J. McKay, E. Clarke, and S. J. Reay, “Surface electric fields and geomagnetically induced currents in the Scottish Power grid during the 30 October 2003 geomagnetic storm,” *Space Weather*, vol. 3, no. 11, n/a-n/a, 2005, doi: 10.1029/2005SW000156.

[128] S. P. Blake, “Modelling and Monitoring Geomagnetically InducedCurrents in Ireland,” Dissertation, School of Physics, University of Dublin, Dublin, Ireland.

[129] B. Efimov, V. Selivanov, and Y. Sakharov, “Impact of Geomagnetically Induced Currents on Transformers in the Kola Power Grid,” in *2019 International Multi-Conference on Industrial Engineering and Modern Technologies (FarEastCon)*, Vladivostok, Russia, Oct. 2019, pp. 1–4.

[130] K.-C. Choi, M.-Y. Park, Y. Ryu, Y. Hong, J.-H. Yi, S.-W. Park, and J.-H. Kim, “Installation of Induced Current Measurement Systems in Substations and Analysis of GIC Data during Geomagnetic Storms,” *Journal of Astronomy and Space Sciences*, vol. 32, no. 4, pp. 427–434, 2015, doi: 10.5140/JASS.2015.32.4.427.

[131] C. J. Rodger, M. A. Clilverd, D. H. Mac Manus, I. Martin, M. Dalzell, J. B. Brundell, T. Divett, N. R. Thomson, T. Petersen, Y. Obana, and N. R. Watson, “Geomagnetically Induced Currents and Harmonic Distortion: Storm-Time Observations From New Zealand,” *Space Weather*, vol. 18, no. 3, 2020, doi: 10.1029/2019SW002387.

[132] D. H. Mac Manus, C. J. Rodger, M. Dalzell, A. W. P. Thomson, M. A. Clilverd, T. Petersen, M. M. Wolf, N. R. Thomson, and T. Divett, “Long-term geomagnetically induced current observations in New Zealand: Earth return corrections and geomagnetic field driver,” *Space Weather*, vol. 15, no. 8, pp. 1020–1038, 2017, doi: 10.1002/2017SW001635.

[133] N. M. Simon, “Esitmation of Geomagnetically Induced Currents (GICs) in the Namibian Transmission network,” University of Cape Town. Accessed: Dec. 7 2018. [Online]. Available: https://open.uct.ac.za/bitstream/handle/11427/8688/thesis_ebe_2013_simon_mn.pdf?sequence=1

[134] R. M. Silva, H. Martins, I. Nascimento, J. M. Baptista, A. L. Ribeiro, J. L. Santos, P. Jorge, and O. Frazão, “Optical Current Sensors for High Power Systems: A Review,” *Applied Sciences*, vol. 2, no. 3, pp. 602–628, 2012, doi: 10.3390/app2030602.

[135] P. Schachinger, D. Albert, A. Fröhlich, H. Renner, J. Mandl, P. Trampitsch, R. Klambauer, A. Bergmann, and W. Schöffer, “DC Measurement in HVAC-Systems: Status Quo and Recent Developments,” in *58th International Universities Power Engineering Conference, UPEC 2023*, Dublin, Ireland, 2023.

[136] J. Mandl, P. Trampitsch, P. Schachinger, D. Albert, R. Klambauer, and A. Bergmann, “Fiber optic current sensor prototype for low DC measurements in the power grid,” in *2023 IEEE 13th International Workshop on Applied Measurements for Power Systems (AMPS)*.

[137] *EN 50522:2011 Earthing of power installations exceeding 1 kV a.c.*, 50522, OVE, 2011.

[138] D. Albert, “Power Transformer under DC/GIC bias - Modelling and Measurement,” PhD Thesis, Institute of Electrical Power Systems, Graz University of Technology, Graz, 2022.

[139] P. Schachinger, D. Albert, and H. Renner, “Low Frequency Currents Source Identification,” in *2022 20th International Conference on Harmonics & Quality of Power (ICHQP)*, Naples, Italy, 2022, pp. 1–6.

[140] B. Schäfer, M. Timme, and D. Witthaut, “Isolating the Impact of Trading on Grid Frequency Fluctuations,” in *2018 IEEE PES Innovative Smart Grid Technologies Conference Europe (ISGT-Europe)*, 2018, pp. 1–5.

[141] B. Schäfer, C. Beck, K. Aihara, D. Witthaut, and M. Timme, “Non-Gaussian power grid frequency fluctuations characterized by Lévy-stable laws and superstatistics,” *Nat Energy*, no. 3, pp. 119–126, 2018, doi: 10.1038/s41560-017-0058-z.

[142] M. Anvari, L. R. Gorjão, M. Timme, D. Witthaut, B. Schäfer, and H. Kantz, “Stochastic properties of the frequency dynamics in real and synthetic power grids,” *Phys. Rev. Research*, vol. 2, no. 1, 2020, doi: 10.1103/PhysRevResearch.2.013339.

[143] CIGRE WG B5.57, *Protection, Monitoring and Control of Shunt Reactors*.
[144] Z. Gajic, B. Hillström, and F. Mekic, “HV Shunt Reactor Secrets for Protection Engineers,” in *30th Western Protective Relaying Conference,Spokane, Washington*.
[145] F. K. Basha and M. Thompson, “Practical EHV reactor protection,” in *66th Annual Conference for Protective Relay Engineers, 2013: ProRelay 2013 ; 8 - 11 April 2013, College Station, TX, USA*, College Station, TX, USA, 2013, pp. 408–419.
[146] L. Ghatpande, N. Ganta, J. Perez, and J. Burton, “Analyzing the Impact of Shunt Reactor Switching Operations Based on DFR Monitoring System,” in *72nd Annual Conference for Protective Relay Engineers: March 25-March 28, 2019*, College Station, TX, USA, 2019, pp. 1–8.
[147] L. Gertmar, P. Karlsson, and O. Samuelsson, “On DC injection to AC grids from distributed generation,” in *European Conference on Power Electronics and Applications, 2005: 11 - 14 Sept. 2005, [Dresden, Germany*, Dresden, Germany, 2005, 1-10.
[148] M. Pfeiffer, C. M. Franck, and J. Schmutz, “DC ion-currents in AC conductors in hybrid AC/DC transmission systems,” in *AC and DC Power Transmission 2015*, 2015.
[149] M. Pfeiffer, S. Hedtke, and C. M. Franck, “Corona Current Coupling in Bipolar HVDC and Hybrid HVAC/HVDC Overhead Lines,” *IEEE Trans. Power Delivery*, vol. 33, no. 1, pp. 393–402, 2018, doi: 10.1109/TPWRD.2017.2713603.
[150] J. M. Torta, A. Marcuello, J. Campanyà, S. Marsal, P. Queralt, and J. Ledo, “Improving the modeling of geomagnetically induced currents in Spain,” *Space Weather*, vol. 15, no. 5, pp. 691–703, 2017, doi: 10.1002/2017SW001628.
[151] M. Schühle and S. Tenbohlen, “Berechnung Und Messung Von Geomagnetisch Induzierten Strömen Im Deutschen Übertragungsnetz: Calculation And Measurement Of Geomagnetic Induced Currents In The German Transmission Grid,” in *VDE-Hochspannungstechnik*, Online, 2020, pp. 447–452.
[152] M. Schühle and S. Tenbohlen, “Berechnung von geomagnetisch induzierten Strömen auf Basis eines dreidimensionalen Leitfähigkeitsmodells,” (in De;de), *Elektrotech. Inftech.*, pp. 1–6, 2020, doi: 10.1007/s00502-020-00828-3.
[153] P. Bloomfield, *Fourier analysis of time series: An introduction,* 2nd ed. New York: Wiley, 2010. [Online]. Available: http://onlinelibrary.wiley.com/book/10.1002/0471722235
[154] D. H. Boteler and R. J. Pirjola, “Numerical Calculation of Geoelectric Fields That Affect Critical Infrastructure,” *IJG*, vol. 10, no. 10, pp. 930–949, 2019, doi: 10.4236/ijg.2019.1010053.
[155] *IEEE Guide for Safety in AC Substation Grounding: IEEE Power and Energy Society*, IEEE Std 80, IEEE Standard Association, Piscataway, NJ, USA, 2015.
[156] *IEEE Guide for Measuring Earth Resistivity, Ground lmpedance, and Earth Surface Potentials of a Grounding System*, 81, IEEE Standard Association, 2012.
[157] H. Schmolke, *Potentialausgleich, Fundamenterder, Korrosionsgefährdung: DIN VDE 0100, DIN 18014 und viele mehr,* 8th ed. Berlin, Offenbach: VDE Verlag GmbH, 2013.
[158] I. Schattauer, A. Römer, R. L. Bailey, R. Leonhardt, G. Bieber, K. Motschka, R. Supper, and A. Schiller, “Laterale Verteilung des elektrischen Widerstandes in Österreich,” in *Arbeitstagung der Geologischen Bundesanstalt 2017*, Bad Ischl, Hallstatt, Gmunden, 2017.
[159] *International Standard 60909-0:2016 Short-circuit currents in three-phase a.c. systems - Part 0 - Calculation of Currents*, 60909-0, IEC, 2016.
[160] P. Schachinger, D. Albert, and H. Renner, “Geomagnetically induced currents: A measurement based inverse determination of earth impedances,” in *2021 56th International Universities Power Engineering Conference (UPEC)*, Middlesbrough, United Kingdom, Aug. 2021, pp. 1–5.
[161] R. Pirjola, “Calculation of geomagnetically induced currents (GIC) in a high-voltage electric power transmission system and estimation of effects of overhead shield wires on GIC modelling,” *Journal of Atmospheric and Solar-Terrestrial Physics*, vol. 69, no. 12, pp. 1305–1311, 2007, doi: 10.1016/j.jastp.2007.04.001.
[162] C. Liu, D. H. Boteler, and R. J. Pirjola, “Influence of shield wires on geomagnetically induced currents in power systems,” *International Journal of Electrical Power and Energy Systems*, vol. 117, p. 105653, 2020, doi: 10.1016/j.ijepes.2019.105653.
[163] R. Santos, M. A. Pais, J. Alves Ribeiro, J. Cardoso, L. Perro, and A. Santos, “Effect of shield wires on GICs: Equivalent resistance and induced voltage sources,” *International Journal of Electrical Power and Energy Systems*, vol. 143, p. 108487, 2022, doi: 10.1016/j.ijepes.2022.108487.
[164] L. Gérin-Lajoie, A. Haddadi, A. Rezaei-Zare, and J. Mahseredjian, “Simultaneous DC and AC Simulation of GMD Impacts in a Power System,” in *Proceedings of the International Conference on Power Systems Transients 2019 (IPST 2019)*.

[165] A. Ovalle, R. Dugan, and R. Arritt, “A Test Case for GIC Harmonics Analysis,” in *CIGRE US National Committee 2019 Grid of the Future*.

[166] A. Ovalle, R. Dugan, and R. Arritt, “GICharm: A System level Analysis tool for Geomagnetic Disturbance related harmonics,” in *2021 IEEE Industry Applications Society Annual Meeting (IAS)*, Vancouver, BC, Canada, 2021, pp. 1–7.

[167] A. Ovalle, R. Dugan, and R. Arritt, “GICharm: A System Level Analysis Tool for Geomagnetic Disturbance Related Harmonics,” *IEEE Transactions on Industry Applications*, vol. 58, no. 2, pp. 1406–1415, 2022, doi: 10.1109/TIA.2022.3145770.

[168] EPRI, “Analysis of Geomagnetic Disturbance (GMD) Related Harmonics: 3002002985,” Electric Power Research Institute (EPRI), Palo Alto, CA, 2014.

[169] P. Schachinger, P. Wohlfart, D. Albert, Herwig Renner, and G. Achleitner, “Influence of GIC related Reactive Power Demand on the Austrian Transmission Grid,” in *Power and Energy Student Summit and Power Electronics Student Summit (PESS & PELS 2022)*, Universität Kassel, Ed., 2022, pp. 1–5.

[170] Joint Allocation Office, *Core publication tool.* [Online]. Available: https://publicationtool.jao.eu/core/ (accessed: Aug. 5 2022).

[171] P. Schachinger, D. Albert, and H. Renner, “Reduction of geomagnetically induced current impacts by optimized neutral point connections,” *IET Generation, Transmission & Distribution*, 2023, doi: 10.1049/gtd2.12957.

[172] J. Holland, *Adaptation in natural and artificial systems*: University of Michigan Press, 1975.

[173] D. E. Goldberg, *Genetic algorithms in search, optimization, and machine learning*: Addison-Wesley, 1989.

[174] S.-K. S. Fan, Y.-C. Liang, and E. Zahara, “A genetic algorithm and a particle swarm optimizer hybridized with Nelder–Mead simplex search,” *Computers & Industrial Engineering*, vol. 50, no. 4, pp. 401–425, 2006, doi: 10.1016/j.cie.2005.01.022.

# Appendix

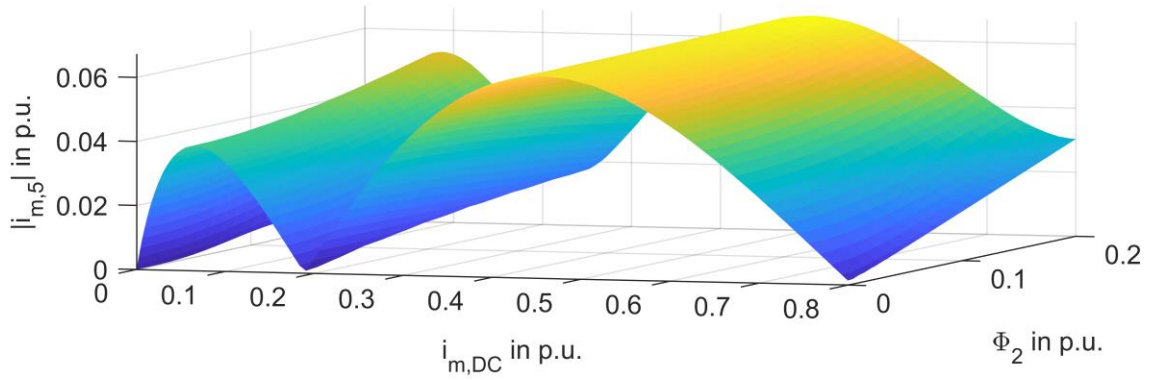
|i_m,5| in p.u.
0.06
0.04
0.02
0
0
0.1
0.2
0.3
0.4
0.5
0.6
0.7
0.8
i_m,DC in p.u.
0
0.1
0.2
Φ_2 in p.u.

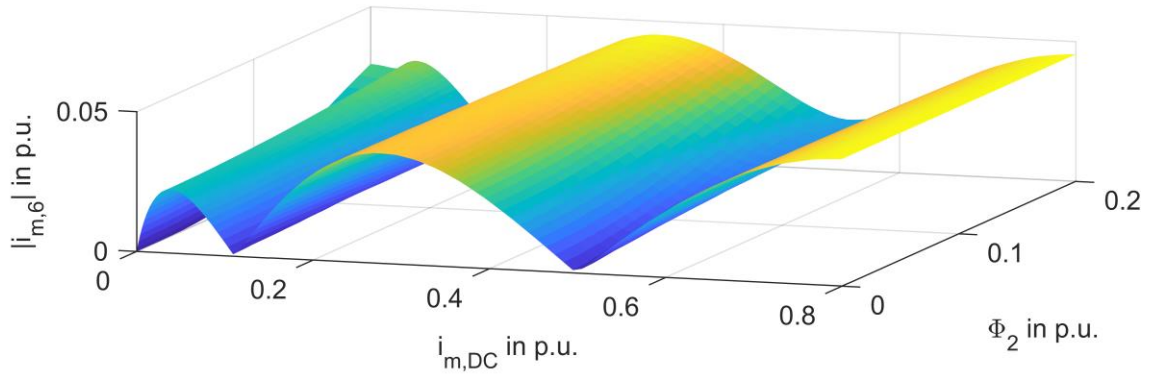
|i_m,6| in p.u.
0.05
0
0
0.2
0.4
0.6
0.8
i_m,DC in p.u.
0
0.1
0.2
Φ_2 in p.u.

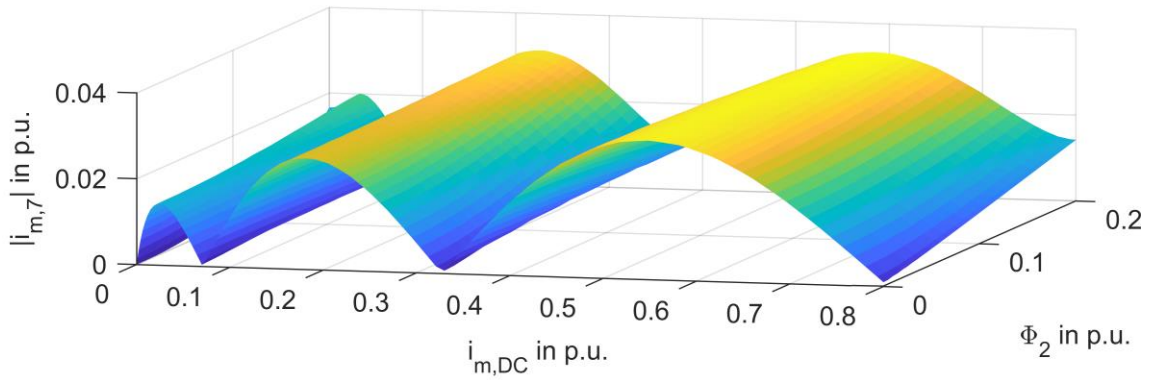
|i_m,7| in p.u.
0.04
0.02
0
0
0.1
0.2
0.3
0.4
0.5
0.6
0.7
0.8
i_m,DC in p.u.
0
0.1
0.2
Φ_2 in p.u.

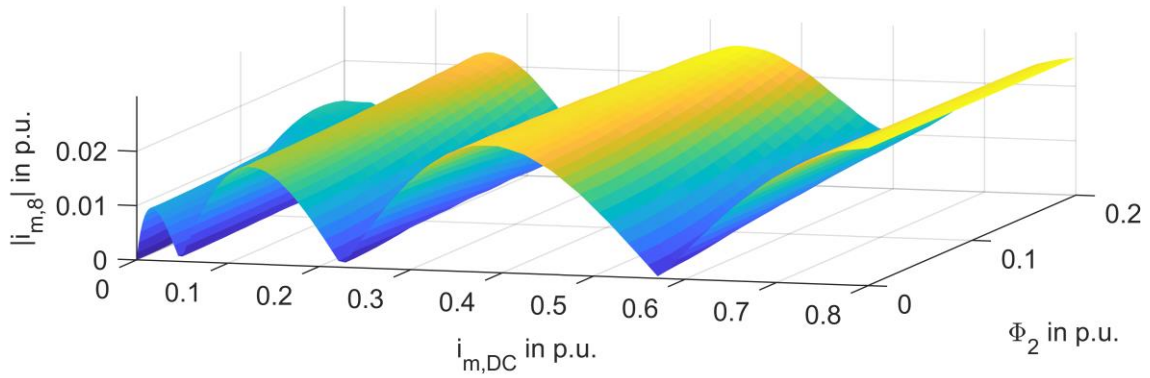
|i_m,8| in p.u.
0.02
0.01
0
0
0.1
0.2
0.3
0.4
0.5
0.6
0.7
0.8
i_m,DC in p.u.
0
0.1
0.2
Φ_2 in p.u.

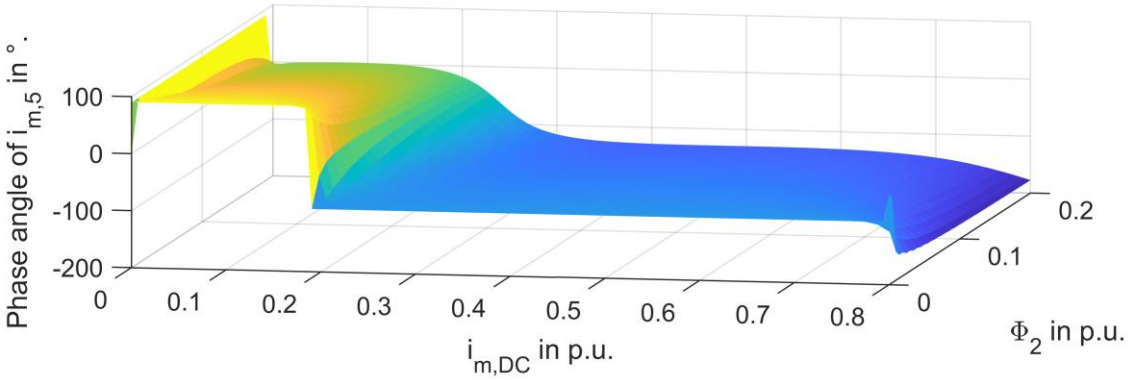
Phase angle of $i_{m,5}$ in °
100
0
-100
-200
0
0.1
0.2
0.3
0.4
0.5
0.6
0.7
0.8
$i_{m,DC}$ in p.u.
0
0.1
0.2
$\Phi_2$ in p.u.

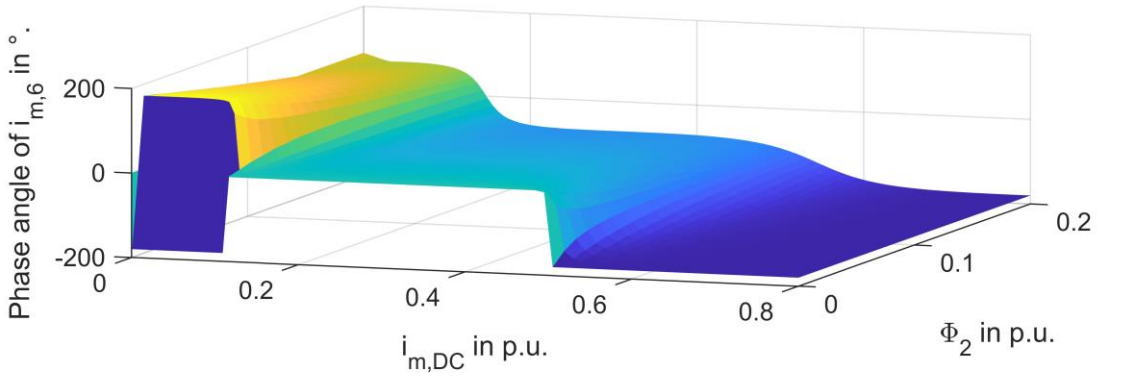
Phase angle of $i_{m,6}$ in °
200
0
-200
0
0.2
0.4
0.6
0.8
$i_{m,DC}$ in p.u.
0
0.1
0.2
$\Phi_2$ in p.u.

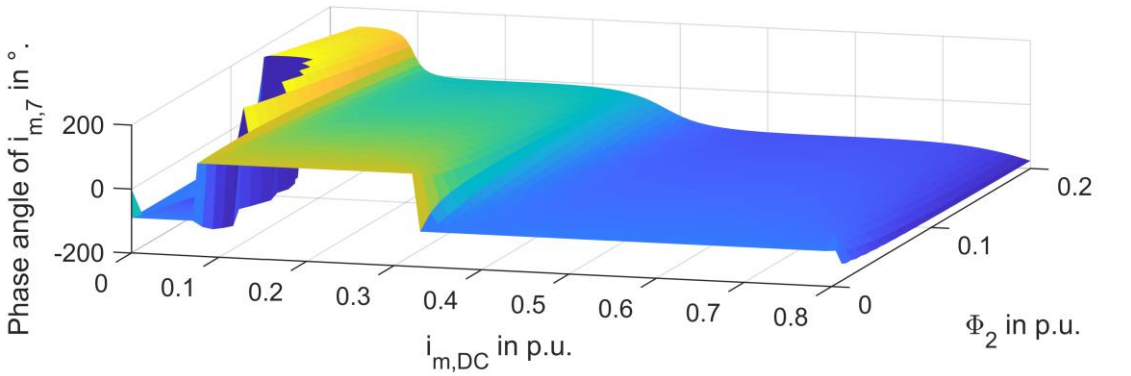
Phase angle of $i_{m,7}$ in °
200
0
-200
0
0.1
0.2
0.3
0.4
0.5
0.6
0.7
0.8
$i_{m,DC}$ in p.u.
0
0.1
0.2
$\Phi_2$ in p.u.

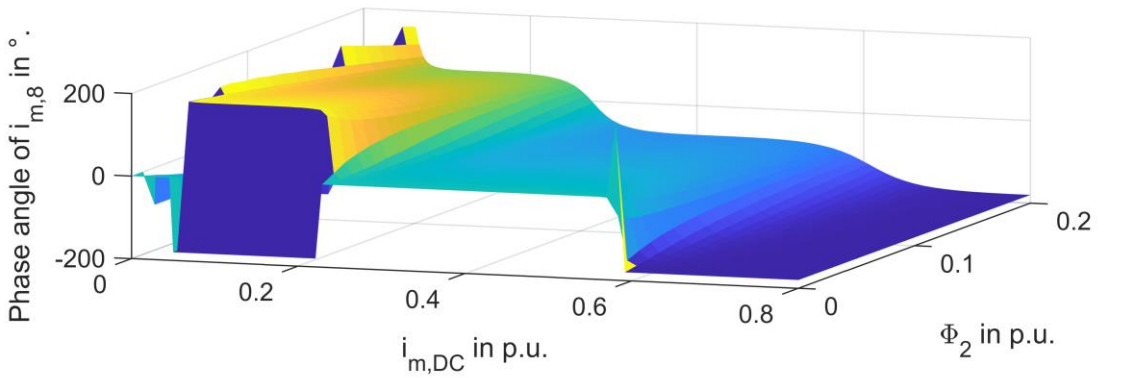
Phase angle of $i_{m,8}$ in °
200
0
-200
0
0.2
0.4
0.6
0.8
$i_{m,DC}$ in p.u.
0
0.1
0.2
$\Phi_2$ in p.u.